Modeling Radiation Belts and Ionospheric Outflows With the Space Weather Modeling Framework

by

Alex Glocer

A dissertation submitted in partial fulfillment
of the requirements for the degree of
Doctor of Philosophy
(Space and Planetary Physics)
in The University of Michigan
2008

Doctoral Committee:

Professor Tamas I. Gombosi, co-Chair
Research Scientist Gabor Toth, co-Chair
Professor Andrew F. Nagy
Professor Fred C. Adams
Professor Gregory Tarle

"Don't Panic" - The Hitchhiker's Guide to the Galaxy

-

To Jessica, my wonderful wife, without whose support and patience I could never have made it.

ACKNOWLEDGEMENTS

Graduate school is a long trying experience that requires dedication, hard work, and self motivation. To survive the experience, however, requires the help and support of family, friends, co-workers and others. It is those wonderful people, whom I have depended upon, that I would like acknowledge and thank.

First and foremost, I want to thank my family. Especially my wife Jessica who has been patient all these years, and always kept me happy and motivated. I love her with all my heart. I also want to thank my parents, Helene and Jorge Glocer, for always encouraging me and pushing me to excel. Also my sister Karen, to whom I always enjoyed talking with about science and math, and my brother Eric, serving bravely in Iraq, he inspires me everyday.

I also want to thank my committee members, Tamas Gombosi, Gabor Toth, Andrew Nagy, Fred Adams, and Greg Tarle for taking the time to read my thesis, attend my defense, and provide their insight. My advisors Tamas Gombosi and Gabor Toth, in particular, always gave me good advice and kept me on track through graduate school. Working with them has been a real pleasure.

I am also grateful to the faculty and students of the department of Atmospheric Oceanic and Space Science at the University of Michigan. K. C. Hansen, Aaron Ridley, and Mike Leimohn have also helped me tremendously with useful conversations. With my fellow students Ofer Cohen, Dan Welling, Jared Bell, Noe Lugaz, and others, there was a true sense of comradery that really made this a great place

to study.

There are certainly other people, not named, to whom I owe a debt of gratitude for their assistance and support in writing his thesis. To them I can only say thank you, and please forgive me for neglecting to mention your name.

TABLE OF CONTENTS

LIST OF FIGURES

Figure

LIST OF TABLES

Table

CHAPTER I

Introduction

The space environment is a vastly complicated system that is immensely difficult to study. Any model needs to have the ability to transcend different temporal and spatial scales, and must incorporate a wide array of techniques. An additional complicating factor is the sparsity of available data which makes purely data based studies challenging. By using carefully constructed numerical models, and utilizing data where appropriate, we study two aspects of the space environment in this thesis: Ionospheric outflow, and radiation belts. Specifically, in this study we:

- Incorporate the Radiation Belt Environment (RBE) model into the Space Weather Modeling Framework (SWMF) and examine how interactions between the magnetosphere, ionosphere, and radiation belts can affect the rapid capture of relativistic particles.
- Develop a new model of ionospheric outflow, called the Polar Wind Outflow Model (PWOM), add it to the SWMF, and then use the coupled codes to explore the impact of ionospheric plasma on the magnetosphere.
- Expand the PWOM to work at Saturn and estimate the rate at which Saturn's ionosphere supplies plasma to the magnetosphere.

This introductory chapter is devoted to providing the scientific and practical motivation behind this study, while the following chapters will delve into each topic in more detail providing specific study descriptions and results.

1.1 Motivation

Solar-terrestrial physics has captivated the imagination of humankind throughout history. Indeed, references to the aurora appear in ancient Chinese and Greek literature and has made their way into several ancient mythologies. Other impacts became evident as the compasses in sailing ships, used for navigation, saw deflections due to changes in the magnetic field of the Earth. However, it was really the dawn of the space age with the launch of Sputnik 1 in 1957, that humankind began to actively explore and understand space. Through exploration and discovery, a coherent picture of the space environment comprised of different regions began to emerge. This thesis deals primarily with the magnetosphere, radiation belts, ionosphere and polar wind. It is therefore appropriate to give a brief description of each region. For more historical perspective refer to Kivelson and Russell (1995).

The magnetosphere refers to the region of space in which the plasma population is controlled by the intrinsic magnetic field of the Earth. It is interaction of the supersonic solar wind with the Earth's magnetic field that forms and shapes the magnetosphere. The Explorer 10 satellite provided some of the earliest measurements of the boundary between the magnetosphere and the solar wind (see for instance Heppner et al. (1962)). However more detailed observations had to wait for Explorer 12 (see Mead and Cahill (1967)).

The radiation belts were first discovered by the Explorer 1 satellite (van Allen, 1959). Radiation belts specifically refer to the relativistic electrons and energetic

ions in the inner magnetosphere. There remains a great deal of interest in this region because of the ability of the energetic population to cause radiation damage to electronics and humans.

The ionosphere refers to the electrically conducting region in the upper atmosphere. Unlike the magnetosphere and the radiation belts, study of the ionosphere began before the dawn of the space age. In fact remote measurements utilizing spectroscopy and radio measurements allowed for study before direct observations from rockets and satellites were possible.

The polar wind refers to the supersonic outflow of particles along open magnetic field lines at high latitude. First suggested by Axford (1968) and Banks and Holzer (1968), and demonstrated experimentally by Hoffman (1970), the polar wind is caused by an ambipolar electric field resulting from the separation between the electrons and the major ion species. More recently there have been new observations of the polar wind by the Akebono satellite Abe et al. (2004) as well as a plethora of new models to describe it (Schunk and Sojka, 1997; Gombosi et al., 1985; Pierrard and Lemaire, 1998).

There is a rich history of space exploration extending for more than 60 years. The discoveries during that time have helped us to classify and understand the various pieces of the space environment system. It is how these regions behave, both independently and as a system, as well as their impact on human activity that drives interest in this field.

1.1.1 The Space Environment as a Coupled System

There is a natural inclination to regard each physical regime in the space environment system independently because such an approach allows for simple modeling technique and basic understanding. That inclination, however, leaves out the very

important interaction between different regimes. Neglecting these interactions yields an incomplete physical picture.

Magnetosphere Ionosphere Coupling (MIC) is an intricate process involving electrical connectivity and mass flow. Energetic electrons and protons precipitate into the ionosphere from the magnetosphere creating local ionization, heating, aurora and airglow. Mass can also flow from the ionosphere to the magnetosphere. Indeed, ionospheric plasma is found in the magnetosphere during both quiet and active times. A review paper by Daglis et al. (1999) compiles relative magnetosphere ring current composition (see table 1.1) based on the Active Magnetospheric Particle Tracer Explorer (AMPTE) mission of the 1980s and the Combined Release and Radiation Effects Satellite (CRRES) observations. Another study by Sharp et al. (1985) examines International Sun-Earth Explorer (ISEE) 1 satellite and Spacecraft Charging AT High Altitude (SCATHA) satellite mass spectrometer data and found the ionosphere to be an important or dominant source of plasma for the inner magnetosphere. Additionally, Huddleston et al. (2005) examine data from Dynamics Explorer and Polar satellites, and also find the ionosphere to be a sufficient source for magnetospheric plasma.

The ionospheric plasma found in the magnetosphere can have a tremendous impact on the solution in the magnetosphere. The increased density can modify wave speeds, and provide a source of particles to be locally accelerated to higher energies. Moreover, the presence of heavy ions can modify the ring current in the inner magnetosphere, impacting the Dst index and the local plasma beta.

With such a preponderance of data supporting the importance of MIC, it is imperative to look at how these processes are currently included in large scale models. The electrical connectivity between the ionosphere and magnetosphere is usually treated

Ion Source and Species	Quiet Time	Small-Medium Storms	Intense Storms
Total energy density, keV cm^{-}3	∼10	≥50	≥100
Solar Wind H^+,%	≥60	∼50	≤20
Ionospheric H^+,%	≥30	∼20	≤10
Ionospheric O^+,%	≤ 5	∼30	≥60
Solar wind He^{++},%	∼2	≤5	≥10
Solar wind He^+,%	>1	>1	>1
Ionospheric He^+,%	>1	>1	>1
Solar wind, total, %	∼65	∼50	∼30
Ionosphere, total, %	∼35	∼50	∼70

Table 1.1: Sources of Ring Current Ions at L ≈ 5 Based on AMPTE and CRRES Missions (taken from Daglis et al. (1999))

in a similar manner in different models. Typically, a height integrated conductivity is calculated by the ionosphere model which is combined with the Field Aligned Current (FAC) information from the magnetosphere model. The resulting calculation gives the polar cap potential. Most global magnetosphere models use this approach (e.g. Wang et al. (2008),Wiltberger et al. (2004), Ridley et al. (2004)).

Unlike the electrical connectivity in MIC, mass coupling is handled very differently in different models. Zhang et al. (2007) change the inner boundary density of the BATS-R-US (Block-Adaptive-Tree Solar-wind Roe-type Upwind Scheme (Powell et al., 1999; De Zeeuw et al., 2000; Gombosi et al., 2001)) magnetosphere model to represent changing amounts of mass flowing from the ionosphere to the magnetosphere. In this case the plasma is drawn off the inner boundary by pressure gradients. They found that the calculated Dst index is sensitive the value chosen. Another approach is taken by Gagne (2005) who use an empirical relationship relating oxygen outflow developed by Strangeway et al. (2000) to set the inner boundary density of the Lyon-Fedder-Mobarry (LFM) (Lyon et al., 2004) magnetosphere model in the following manner: The study by Strangeway et al. (2000) relates the Poynting flux

with cusp related oxygen ion outflow. Gagne (2005) calculates the Poynting flux in the LFM code, maps the results to Fast Auroral SnapshoT explorer (FAST) satellite altitudes, assume the cusp relationship holds over the entire polar cap, and then set the boundary accordingly. Winglee (2000) uses yet another approach. He uses centrifugal acceleration of ions to throw plasma off the inner boundary. Then their multi-fluid MHD model tracks the out-flowing ionospheric plasma in order to define a geopause where the magnetosphere is dominated by ionospheric plasma instead of solar wind plasma. In chapter III we will outline a new approach to dealing with the problem of mass coupling between the ionosphere and magnetosphere.

Of course the ionosphere is also affected by external sources. A paper by Abe et al. (2004) examines the Akebono supra-thermal ion mass spectrometer observations to quantify the impact of varying solar input on polar wind type ionospheric outflow. They indeed found that there was significant dependence on solar input (characterized by the 10.7 cm solar radio flux known as the F10.7 index). This result compares well with earlier numerical studies (Cannata and Gombosi, 1989; Gombosi et al., 1991). The topside electron heat flux, which represents direct magnetosphere energy input, also affects the outflow solution. Bekerat et al. (2007) carry out a study to find the range of values that allow their model to best match data taken by the Defense Meteorological Satellites Program (DMSP) satellite. Those values for topside heat flux fall into the range of $0.5 - 1.5 \times 10^{10}$ eV cm^{-2} s^{-1}.

The radiation belts are also a highly integrated part of the space environment system. Earth's radiation belts consist of energetic plasma with temperatures between tens of keV to several MeV, located in the inner magnetosphere (1.2-12 R_e). One of the earliest discoveries of space era (van Allen, 1959), the radiation belts continue to be of interest due to their dramatic and often hazardous effects on space-borne as-

sets. Despite many years of study, there remain several unanswered questions about this important region.

Two major questions are the response of the radiation belts to geomagnetic storms and the source of the observed populations. Reeves et al. (2003) notes the intriguing response of the radiation belts to geomagnetic activity, with populations either dropping or rising compared to prestorm values for reasons that are not fully understood. Furthermore, Chen et al. (2006) find some events where radial diffusion provides the main source of particles, and other events that are due to internal, locally accelerated, sources. These studies bring forth interesting questions. However, the reasons for radiation belt enhancement for specific events remains unknown, as does the specific mechanism for acceleration.

The radiation belts interact strongly with other parts of the space environment. For instance, the charged particle population is affected by changes in the geomagnetic field of the magnetosphere. Therefore, changes in the solar wind pressure, solar wind magnetic field orientation, ionospheric conductance, or any other change that impacts the geomagnetic field in the magnetosphere, by extension, impacts the radiation belts. Similarly changes in the plasmasphere or the ionospheric conduction can also affect the solution. Because of the highly interconnected nature of the radiation belts, a systems approach is needed. These issues will be dealt with in great detail in chapter II.

1.1.2 Practical Consequences: Space Weather

Several times a year, the sun releases a tremendous amount of energy in the form of solar flares and Coronal Mass Ejections (CMEs). The resulting interaction with the Earth can be stunningly beautiful, such as the aurora. On the other hand, the interactions can have a devastating impact on human technology and health. The

effects, both beautiful and otherwise, of the space environment on human activities are collectively referred to as space weather. Improving our ability to model the space environment can potentially lead to the mitigation of space weather damage through forecasting. The particular aspects of space weather that the work described in this thesis can improve are satellite drag and charging.

Increased X-ray and EUV flux in the ionosphere/thermosphere can cause the atmosphere to heat up and expand. The expanded atmosphere can lead to an increase in satellite drag, causing the orbit to degrade and potentially falling out of orbit earlier than anticipated. A June 12, 1979 article in the New York Times titled *Skylab Nears Its Dangerous Plunge; Skylab Nears Plunge to Earth* describes how satellite drag terminated the Skylab mission ahead of schedule. Satellite drag is still a very real concern; For example, the iridium satellite constellation of low earth orbiting satellites, which carry communications to remote areas, is susceptible to drag.

Satellite charging occurs in two forms: Surface charging and deep dielectric charging. Both types of charging have been exhaustedly studied and discussed in numerous papers (see for instance Garrett and Whittlesey (2000); Baker (2000); Wrenn et al. (2002); National Research Council (2003)). Surface charging refers to the accumulation or charge on the surface of the spacecraft, whereas deep dielectric charging is the charge accumulated on the interior. While the discharges from surface charging are only loosely coupled to the spacecraft electronics, deep dielectric charging can cause significant damage to a satellites circuits. Electron energies that can lead to this internal charging range from 100 keV to a few MeV (Garrett and Whittlesey, 2000). It is precisely this energies range that we are modeling in chapter II.

As human reliance on space-based assets continues to grow, it becomes increasingly important to mitigate the costly effects of space weather. We rely on satellites

for direct to consumer products (television and radio), gps navigation, and military operations. Therefore the cost of space weather can not just be measured in terms of lost revenue, but in the loss of services upon which we have come to depend on. Having a good radiation belt model can help understand and potentially mitigate radiation hazards, and a good model for ion outflow can improve our magnetosphere solution, improving space weather prediction.

1.2 Techniques

1.2.1 Fluid vs Kinetic

We utilize a variety of techniques to model the space environment. This thesis uses two main methods to study space plasma: Kinetic and Fluid. Both approaches involve obtaining a solution to the Boltzmann equation, either without making assumptions about the distribution function, in the case of kinetic solutions, or by taking velocity moments and assuming a closure relation, in the case of fluid solutions.

The Boltzmann equation describes the time evolution of the distribution function. It is given by (Boltzmann, 1872):

$$\frac{\partial f}{\partial t} + v_i \frac{\partial f}{\partial x_i} + a_i \frac{\partial f}{\partial v_i} = \frac{\delta f}{\delta t} \tag{1.1}$$

f is the distribution function, the subscript i refers to the dimension index, v_i is velocity, a_i is the acceleration, and x_i is the position. The right hand side,$\frac{\delta f}{\delta t}$, is the collision term.

Models that obtain a solution to the Boltzmann equation without assuming a form of the distribution function are known as kinetic models. This approach is extremely useful when dealing with problems that can not be treated using a fluid approach. Of particular interest to this work, is how the Boltzmann equation can be

used to study the radiation belts.

When modeling the radiation belts we solve the Boltzmann equation to obtain the densities of electrons in different energy bins. This approach is taken in chapter II. However, rather than use the version of the equation given above, the RBE model solves the bounce-averaged Boltzmann equation given by (Fok et al., 2008):

$$\begin{aligned} &\tfrac{\partial f_s}{\partial t} + \langle\dot{\lambda_i}\rangle\tfrac{\partial f_s}{\partial \lambda_i} + \langle\dot{\phi_i}\rangle\tfrac{\partial f_s}{\partial \phi_i} = \\ &\left((E+E_0)\sqrt{E(E-2E_0)}\right)^{-1}\tfrac{\partial}{\partial E}\left((E+E_0)\sqrt{E(E-2E_0)}D_{EE}\tfrac{\partial f_s}{\partial E}\right) \\ &+\left(T(\alpha_0)\sin 2\alpha_0\right)^{-1}\tfrac{\partial}{\partial \alpha_0}\left(T(\alpha_0)\sin 2\alpha_0 D_{\alpha_0\alpha_0}\tfrac{\partial f_s}{\partial \alpha_0}\right) - \left(\tfrac{f_s}{0.5\tau_b}\right)_{Loss\ Cone} \end{aligned} \tag{1.2}$$

on an ionosphere based grid. The equation is said to be "bounce averaged" because the distribution function, f_s, is the average distribution function on the field-line between the magnetic mirror points, and λ_i and ϕ_i are magnetic latitude and longitude at the ionospheric foot point. E is the energy, and α_0 is the pitch angle. The collision terms on the right hand side represent the diffusion in energy and pitch angle with diffusion coefficients D_{EE} and $D_{\alpha_0\alpha_0}$. respectively. Additionally, the loss of particles by scattering into the loss cone is included in the final term of the equation, with τ_b being the bounce period.

It is often the case that solving the kinetic equations is not practical. In these situations it is preferable to solve for macroscopic quantities such as density, bulk flow velocity, or pressure. By taking velocity moments of the Boltzmann equation we can derive transport equations, such as the Euler or Navier-Stokes equations. In chapter III we utilize this 'fluid' approach, applying the gyrotropic transport equations (3.1 - 3.4) to model the polar wind.

The magnetosphere is another regime where we utilize a fluid like approach. In addition to the fluid equations, we also have to incorporate Maxwell's equations and

Ohm's law. The resulting equations are known as the Magnetohydrodynamic (MHD) equations. Derivations of the MHD equations can be found in any elementary plasma physics textbook and the process will not be reiterated here, but briefly stated the MHD equations in conservative form are (Gombosi, 1998):

$$
\begin{aligned}
\frac{\partial \rho}{\partial t} + \nabla \cdot (\rho \mathbf{u}) &= 0 \\
\frac{\partial \rho \mathbf{u}}{\partial t} + \nabla \cdot \left(\rho \mathbf{u}\mathbf{u} + p\mathbf{I} + \frac{B^2}{2\mu_0}\mathbf{I} - \frac{\mathbf{B}\mathbf{B}}{\mu_0} \right) &= 0 \\
\frac{\partial \mathbf{B}}{\partial t} + \nabla \cdot (\mathbf{u}\mathbf{B} - \mathbf{B}\mathbf{u}) &= 0 \\
\frac{\partial \epsilon}{\partial t} + \nabla \cdot \left[\left(\epsilon + p + \frac{\mathbf{B}\cdot\mathbf{B}}{2\mu_0} \right) \mathbf{u} - \frac{1}{\mu_0}(\mathbf{B}\cdot\mathbf{u})\mathbf{B} \right] &= 0 \quad ,
\end{aligned}
\tag{1.3}
$$

where

$$\epsilon = \frac{p}{\gamma - 1} + \rho \frac{\mathbf{u}\cdot\mathbf{u}}{2} + \frac{\mathbf{B}\cdot\mathbf{B}}{2\mu_0}$$

. The variables in 1.3 are defined as follows: ρ is the mass density, t is time, $\mathbf{u}$ is the velocity, p is the pressure, $\mathbf{B}$ is is the magnetic field, and $\mathbf{I}$ is the identity matrix.

A wide array of techniques, including different types of kinetic and fluid approaches are needed to accurately model the space environment. Taken together with the differing temporal and spatial scales between regimes, the problem of finding a single model to study the entire system appears intractable. We therefore do not rely on a single model, but rather a framework of models as outlined in the next section.

1.2.2 A Framework Approach to the Space Environment

Individual pieces of the space environment are often simulated through the use of independent models. The interactions between these regions can have a significant impact on the solution, but are at best parameterized and just as often ignored. Including all of these models into a single monolithic code, however, is impractical

and lacks flexibility. We therefore turn to a framework approach to studying the space environment.

A *framework* is a reusable design that couples multiple independent models via a standardized interface (Tóth et al., 2005). Frameworks have been used to study various complex systems including geoscience applications. Hill et al. (2004) describe one such framework known as the Earth System Modeling Framework (ESMF). The ESMF joins numerous oceanic and atmospheric models to allow for the investigation of hurricanes, seasonal forecasts, and other weather and climate studies. In the realm of space science, Luhmann et al. (2004) describes a framework that allows for the study of space weather.

In this thesis we rely on the Space Weather Modeling Framework presented by Tóth et al. (2005). The SWMF allows coupling and executing multiple space physics models in parallel, and provides models to the various physics domains. It also provides a uniform, user-friendly interface to the models. The SWMF is a flexible tool which allows for the examination of space physics and space weather problems. The physical models making up the SWMF represent various regions and are compiled into a single parallel and efficient executable (see Tóth et al. (2005) for details). The current version has ten components including: Solar Corona (SC), Eruptive Event Generator (EE), Inner Heliosphere (IH), Solar Energetic Particles (SP), Global Magnetosphere (GM), Inner Magnetosphere (IM), Radiation Belt (RB), Ionosphere Electrodynamics (IE), Upper Atmosphere (UA), and Polar Wind (PW). Figure 1.1 illustrates the component layout and couplings.

The SWMF utilizes a layered architecture. On the highest level is a user interface layer which allows for configuration, setup, and execution. The next level is the superstructure layer which contains the framework services and component in-

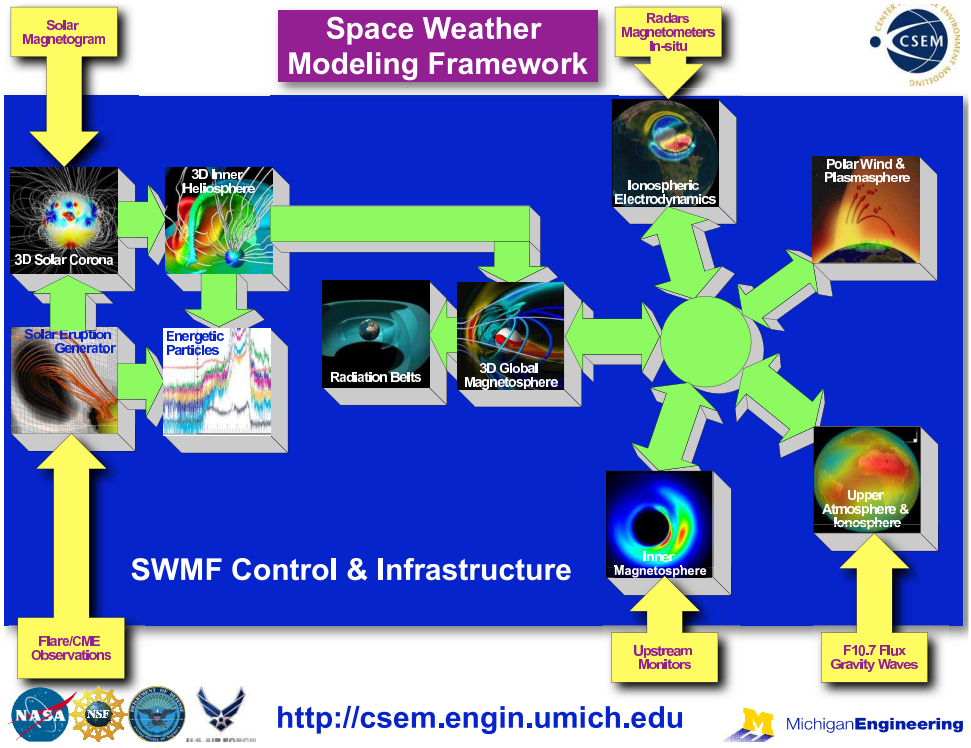

Figure 1.1: A schematic of the SWMF showing components and model couplings (courtesy of Tamas Gombosi)

terfaces. Underneath that lays individual physics models which sit on top of a final infrastructure layer containing shared utilities. The full details of this architecture is beyond the scope of the work presented here, but since the incorporation of new physics components is an essential part of the studies presented in this thesis, it is appropriate to give additional detail on the integration of components.

The physics models interact with the larger framework though a component interface known as a wrapper. The wrapper provides the methods which allows the physics model to be controlled by the control module and exchange information with other components through a coupler. It must provide the methods that set the parameters, initialize the component, advance the solution, save restart files, receive/get information from/for other components, and finalize the simulation at the end. Figure 1.2 illustrates the structure of a physics component.

In order to study the role of ionospheric outflows and radiation belts in the space environment system, new physics components had to be added to the SWMF. In particular, we add the Radiation Belt (RB) component in chapter II and the Polar Wind (PW) component detailed in chapter III. The models representing these components could not be more different, one uses a kinetic approach and the other a fluid approach, but the framework has no problem with using different approaches in different domains; as long as each component has the appropriate interface, the SWMF can be used to simulate the space environment with each region represented with the best available model.

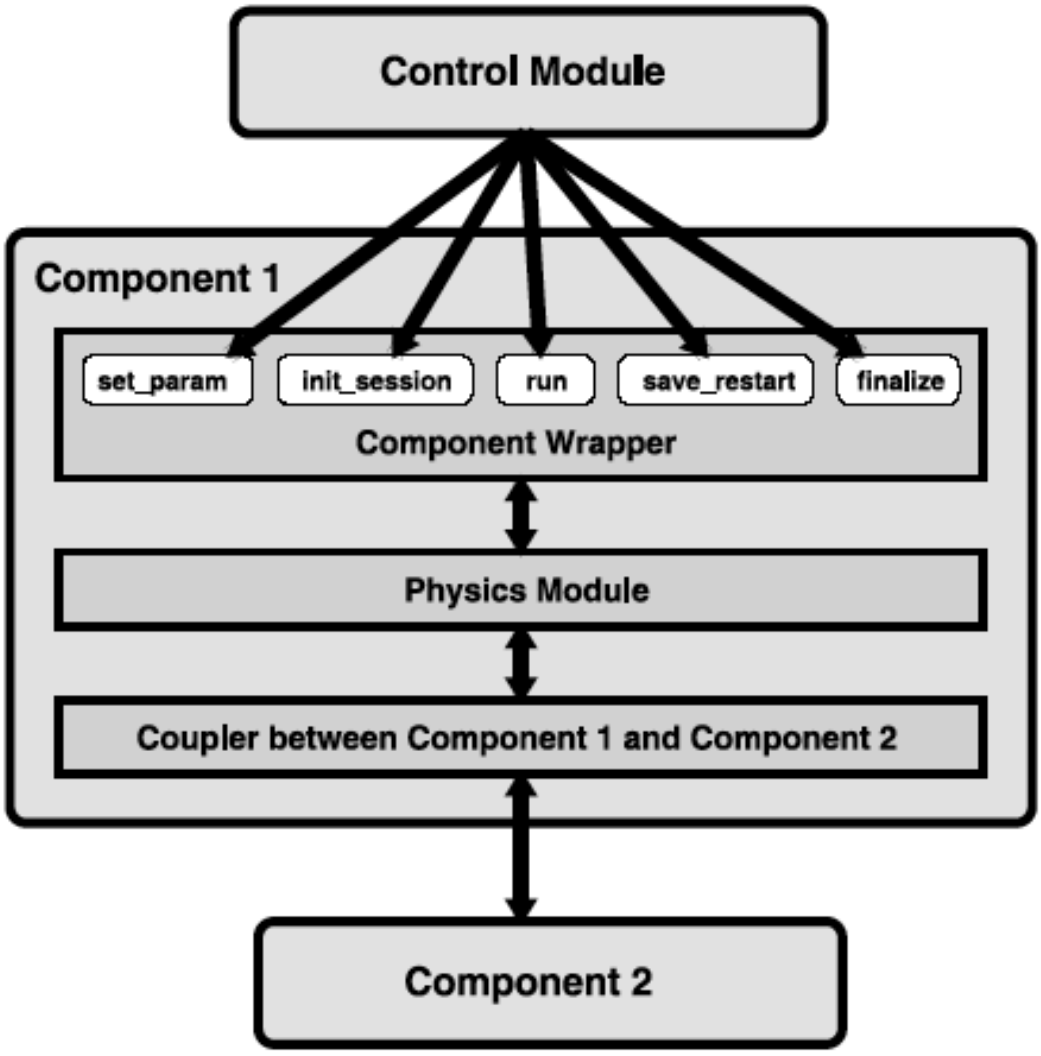

Figure 1.2: The structure of a component of the SWMF (Tóth et al., 2005)

CHAPTER II

Modeling Radiation Belts

2.1 Chapter Abstract

We have integrated the Fok Radiation Belt Environment model (RBE) into the Space Weather Modeling Framework (SWMF). RBE is coupled to the global magnetohydrodynamics component (represented by the BATS-R-US code) and the Ionosphere Electrodynamics component of the SWMF. The radiation belt model solves the convection-diffusion equation of the plasma in the energy range of 10keV to a few MeV. In stand-alone mode RBE uses Tsyganenko's empirical models for the magnetic field, and Weimer's empirical model for the ionospheric potential. In the SWMF the BATS-R-US model provides the time dependent magnetic field by efficiently tracing the closed magnetic field-lines and passing the geometrical and field strength information to RBE at a regular cadence. The Ionosphere Electrodynamics component uses a 2D vertical potential solver to provide new potential maps to the RBE model at regular intervals. We discuss the coupling algorithm and show some preliminary results with the coupled code. We run our newly coupled model for periods of steady solar wind conditions and compare our results to the radiation belt model using an empirical magnetic field and potential model. We also simulate the radiation belts for an active time period.

2.2 Introduction

Earth's radiation belts consist of energetic plasma with temperatures between tens of keV to several MeV, located in the inner magnetosphere (1.2-12 R_e). One of the earliest discoveries of space era (van Allen, 1959), the radiation belts continue to be of interest due to their dramatic and often hazardous effects on space-borne assets. It is therefore important to construct accurate models to study and better understand this region.

To date, several physics based and empirical radiation belt models have been developed, and all have their advantages and weaknesses. For instance a model developed by Li et al. (2001) solves the radial diffusion equation, and exhibits excellent agreement with data; the model is limited, however, to one dimension and requires tweaking the diffusion coefficients. Other codes such as Salammbo (Beutier and Boscher, 1995; Beutier et al., 1995; Bourdarie et al., 1997), and the model of Jordanova and Miyoshi (2005) are three dimensional, but rely on a dipole to represent the magnetic field of the magnetosphere.Fok et al. (2001) is also global in extent, but uses an empirical magnetic field model. Elkington et al. (2004) read in MHD calculated magnetic fields from a file, but lack the realistic ring current needed for storm time evolution of the geomagnetic field in the inner magnetosphere.

A realistic time-varying geomagnetic field is crucial for understanding radiation belt dynamics, particularly during storm time. Some models have included just such a field; Zheng et al. (2003) for instance, use the T96 and T01 (Tsyganenko, 2002a,b) models that take IMF and Dst as inputs. Zheng et al. (2003) solve the convection-diffusion equation in the context of this realistic magnetic field to create a radiation belt forecasting model. A similar approach is taken by Ukhorskiy et al. (2006) who

take the magnetic field from the TS05 model (Tsyganenko and Sitnov, 2005). They then use a test particle method to study storm time transport and loss.

Sources, losses and transport of energetic plasma during during a storm are not fully understood. Flux intensities at the main phase of a storm are significantly depleted (Reeves et al., 2003). The relative importance of adiabatic expansion due to ring current intensification, and other sources and losses needs to be quantified. From observations, Chen et al. (2006) find some events where radial diffusion provides the main source of particles, and other events that are due to internal, locally accelerated, sources. Reeves et al. (2003) notes the intriguing response of the radiation belts to geomagnetic activity, with populations either dropping or rising compared to prestorm values for reasons that are not fully understood.

In this chapter, we present a new approach to modeling the radiation belts during active times. We include the Radiation Belt Environment model into the Space Weather Modeling Framework (SWMF), thereby giving us the ability to couple the radiation belt model with a magnetosphere model and ionosphere model, which are further coupled with other components of the SWMF. The global MHD model obtains a realistic time-varying geomagnetic field (Ridley et al., 2002; Gombosi et al., 2004; Zhang et al., 2007). This magnetic field is used as input to the radiation belt code. We describe the radiation belt model in section 2.3, and the coupled model in section 2.4. Finally, we present some of our results modeling the 23-26 October 2002 storm in section 2.5.

2.3 The Radiation Belt Environment Model

The Radiation Belt Environment (RBE) model (Zheng et al., 2003; Fok et al., 2008) is a convection-diffusion model created to understand the radiation belts during

active periods. Fok et al. (2008) provide a complete description of the current status of the RBE model. Here we will only highlight the main points.

This kinetic model solves the bounce-averaged Boltzmann equation given in Fok et al. (2001) and Zheng et al. (2003) for electrons with energies ranging from 10 keV to 6MeV. The physical domain of the model is defined by the ionospheric foot-points of the closed field-line region. The innermost field-line is considered to have its foot-point at 11.8 degrees latitude while the outermost foot-point is at 70.2 degrees with a non-uniform resolution. In the azimuthal direction the grid consisting of 48 points is set to be equally spaced.

The effects of time-varying magnetic field, and the associated induced electric field, are included in the RBE model. Zheng et al. (2003) used an empirical magnetic field model to study the effect of time-varying magnetic field during active time periods. Additionally, they utilize an empirical model (Weimer, 1996) for the ionospheric potential. Zheng et al. (2003) demonstrate reasonable agreement with data, and illustrate the efficacy of this approach. In section 2.4 we discuss improvements to this technique by replacing the empirical magnetic field and potential models with physics based approaches.

2.4 The Coupled Model

The major scientific aims of coupling the RBE model with a global model are to self-consistently include the effect of time-varying magnetic field in the radiation belt, to add a physics based ionospheric potential, and to gain the ability to study the radiation belt solution as part of a larger system. These advantages bring with them some formidable challenges. The models interact in a three dimensional, overlapping domain, they use vastly different grids, and the magnetosphere's solution is

potentially distributed across many processors at any given time during the simulation. In this section we discuss the coupling and challenges of including the RBE into the Space Weather Modeling Framework.

The Space Weather Modeling Framework (SWMF) incorporates physical models of various regions into a single parallel and efficient executable (see Tóth et al. (2005) for details). Each physical region is treated as a component of the SWMF and is assigned a two letter abbreviation. The current version of the SWMF has ten components including: Solar Corona (SC), Eruptive Event Generator (EE), Inner Heliosphere (IH), Solar Energetic Particles (SP), Global Magnetosphere (GM), Inner Magnetosphere (GM), Radiation Belt (RB), Ionosphere Electrodynamics (IE), Upper Atmosphere (UA), and Polar Wind (PW). Each component can be represented by one or more model. The RBE model is included as the RB component. Moreover, the SWMF can be configured to run with any subset of components, and can be coupled both sequentially or concurrently.

The principal interaction of the RB component is with GM component. A brief description of the GM component is therefore warranted. In our coupled model, the global magnetosphere is represented by the Block-Adaptive-Tree Solar-wind Roe-type Upwind Scheme or BATS-R-US (Powell et al., 1999; De Zeeuw et al., 2000; Gombosi et al., 2001).

The governing equations solved by BATS-R-US are the magnetohydrodynamic (MHD) equations. Various implementations of the MHD equations are considered including semi-relativistic, Hall, and multi-species MHD. Explicit, implicit and semi-implicit time-stepping is included, as well non-Cartesian grids. The conservative or nonconservative equations can be used. Typically, the conservative version of the equations is used near the shock, while away from the shock we utilize the non-

conservative version. A finite volume discretization is implemented along with block based Adaptive Mesh Refinement (AMR) (Stout et al., 1997; Gombosi et al., 2001).

The GM component's physical domain typically extends from 32 R_e upstream to 224 R_e downstream of the planet, and 64 R_e to the sides. Upstream boundary conditions are taken from either the IH component or satellite measurements. The magnetosphere interacts at it's inner boundary with the IE component represented by a 2D height integrated potential solver given by Ridley et al. (2004). The GM component can also interact with the IM component represented by the Rice Convection Model (RCM) to realistically capture the ring current pressure (De Zeeuw et al., 2004). This last point is essential to modeling storm time conditions.

The magnetosphere solution has been verified and validated in several different studies. Initial verification was carried out by Powell et al. (1999) demonstrating grid convergence and correct numerics. Ridley et al. (2001), verified the ability of the model to reproduce region 1 currents. Ridley et al. (2002) applied to model to the Geospace Circulation Model metrics challenge and found good matches with DMSP satellite data as well as with features of the polar cap potential. More importantly to the work we present in this chapter, Zhang et al. (2007) demonstrated an excellent ability to reproduce the magnetic field data at specific satellites distributed throughout the magnetosphere. Magnetic field is the essential parameter in our coupled radiation belt model.

To couple the three dimensional magnetosphere grid with the ionosphere based RBE grid, we have to deal with the problem of efficient field-line tracing. In principal, we could collect the magnetic field information distributed across the GM processors and send them to the RB processor to be traced in the same manner as is done when RBE uses the T01 or T96 empirical model. While straightforward, this method is

both slow and inefficient, especially if new magnetic field information is being provided every few seconds. We therefore use a new parallel field-line tracing algorithm described in the appendix of Glocer et al. (2008).

The second coupling of the RBE model with a component of the SWMF is with the Ionosphere Electrodynamics (IE) model. The 2D height integrated potential solver representing the IE component, given by Ridley et al. (2004), interacts with the RBE model via a simple one way coupling. New potential patterns are passed at a regular cadence, usually about 10 seconds, and interpolated onto the ionosphere based RBE model grid.

Validation of the IE component was carried out by Wang et al. (2008) using measurements from the CHAMP and DMSP satellites. They found that the model better reproduced the potential along the dawn-dusk line than along the noon-midnight line. Moreover, the model performs better during quiet times than during active times. This last point will arise again in section 2.5.1.

As an initial test that the coupled model is working correctly, we compare the coupled (RB-GM-IE) and stand-alone (using the T96 magnetic field) simulations for steady solar wind conditions. The solar wind density is 5 cm^{-3}, the velocity is 400 km/s, the temperature is 100,000 Kelvin and the magnetic field is -5 nT south. Figure 2.1 demonstrates that during steady solar wind conditions the coupled model and the stand-alone version give very similar results. However, some effects due the coarse resolution are visible, as is the appearance of the short MHD tail.

As mentioned above, the SWMF can be configured using any subset of components. Although the the RB component is only directly interacting with the GM and IE components, including other components can improve the solution of the GM and IE components; the RB solution can thereby be improved as well. The initial results

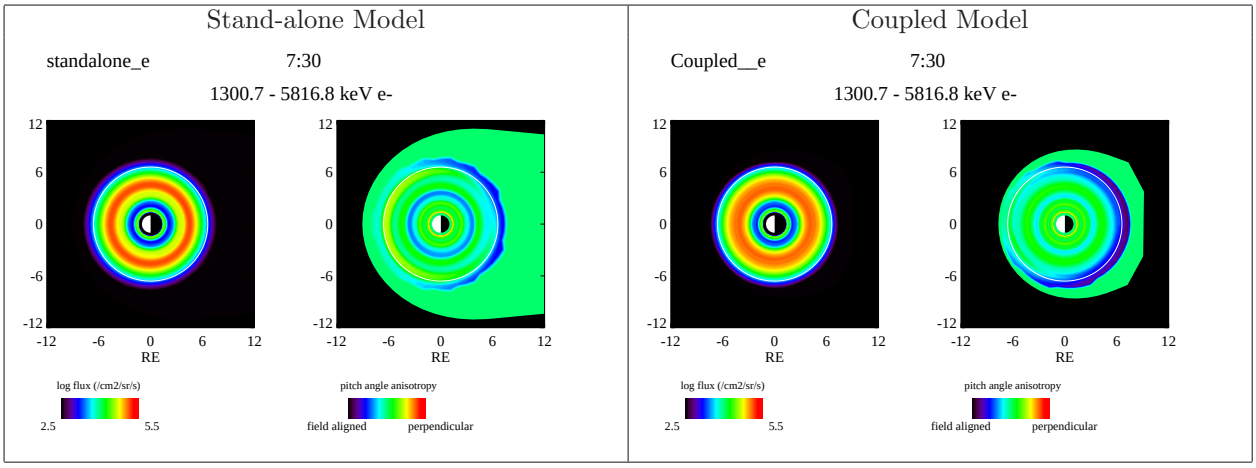

Figure 2.1: The plots above show a comparison of the stand-alone RBE model with the coupled model.

of the coupled model, presented in section 2.5, are run using the SWMF configured with the GM,IE,IM, and RB components.

2.5 Results: The 23-26 October 2002 Storm

We apply our newly coupled model to the geomagnetic storm that occurred on 23-26 October 2002. A moderate storm with Dst reaching as low as -98 nT, our simulation begins at noon on the 23rd, coinciding with the first pressure pulse. The upstream boundaries are set with the solar wind and IMF conditions measured by the ACE satellite (see figure 2.2). We simulate two and a half days of the storm, finishing our simulation at the end of October 26th. Results from the GM and RB components are presented and discussed here.

As mentioned in section 2.4 we are using the SWMF configured with the GM, IE, IM and RB components. In this case, we focus on the GM-RB coupling; the IE component is used, but it is not coupled with the RB component. Instead, the empirical model is used for the potential, and the results that utilize the IE potential are given in section 2.5.1. The components couple every 10s which, in the case of the RBE model, means that new magnetic field traces are provided every 10s. The

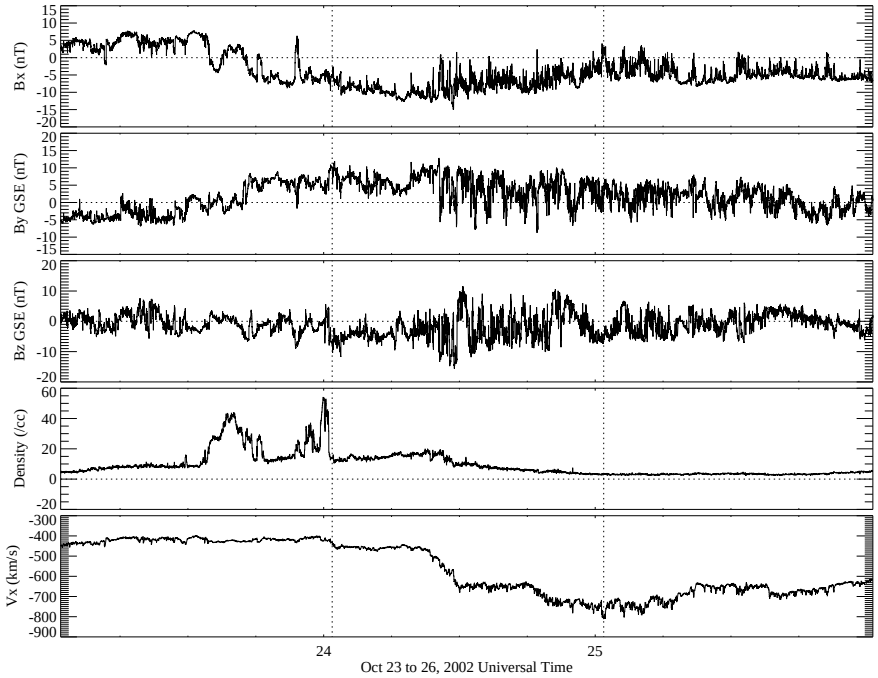

Figure 2.2: The solar wind conditions during the 23-26 October 2002 storm. These conditions are used to drive the coupled model.

grid in the magnetosphere is shown in figure 2.3, and the initial state of the RBE model is shown in figure 2.4. The left hand panel in figure 2.4 shows the equatorial pitch-angle averaged flux while the right panel displays the pitch angle anisotropy. The two and a half day simulation runs slightly faster than real-time on 64 processors on the Columbia Altix machine.

The first result of the coupled model is shown in figure 2.5. The figure shows the 1.3 to 5.8 MeV electron flux as a function of both time from the start of the simulation and L shell. The outer belt, slot region, and inner radiation belt are clearly separated throughout the entirety of the simulation. Moreover, we see a decrease in the flux starting around 32 hours into the simulation, about 20 UT on the 24th, near the minimum Dst. Following the decrease, there is a rapid capture of particles from high L-shell that quickly leads to a flux enhancement in the range $3.5 < L < 5$.

We examine the rapid capture in detail in figure 2.6. Each frame of the figure is labeled by its simulation time. Frame A shows the conditions immediately prior

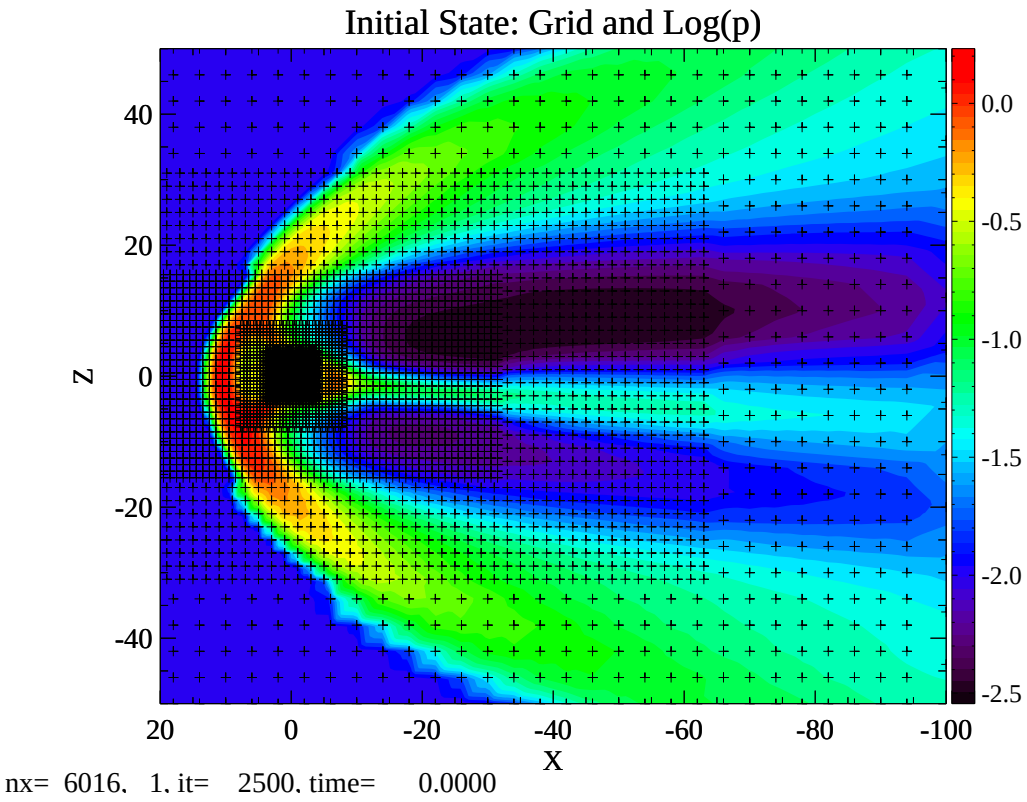

Figure 2.3: The initial condition and grid in the magnetosphere

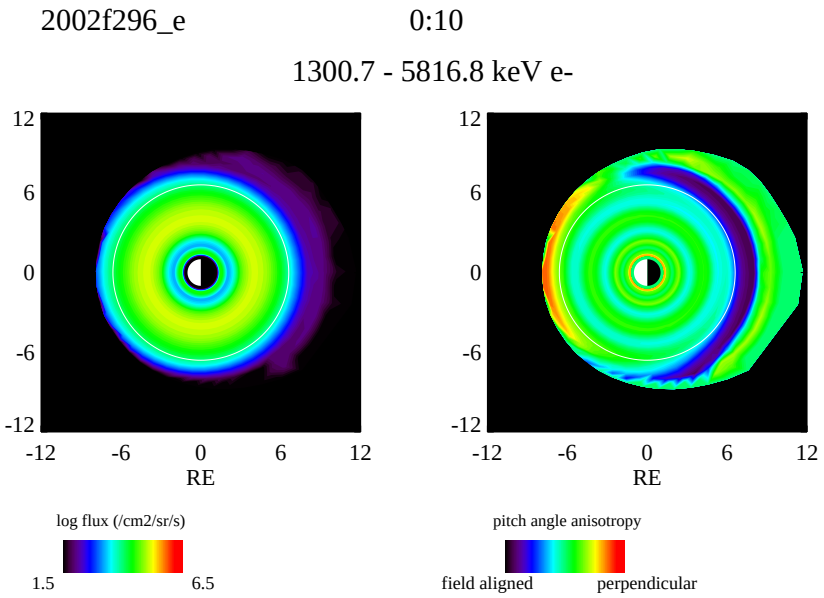

Figure 2.4: The initial condition in the radiation belts

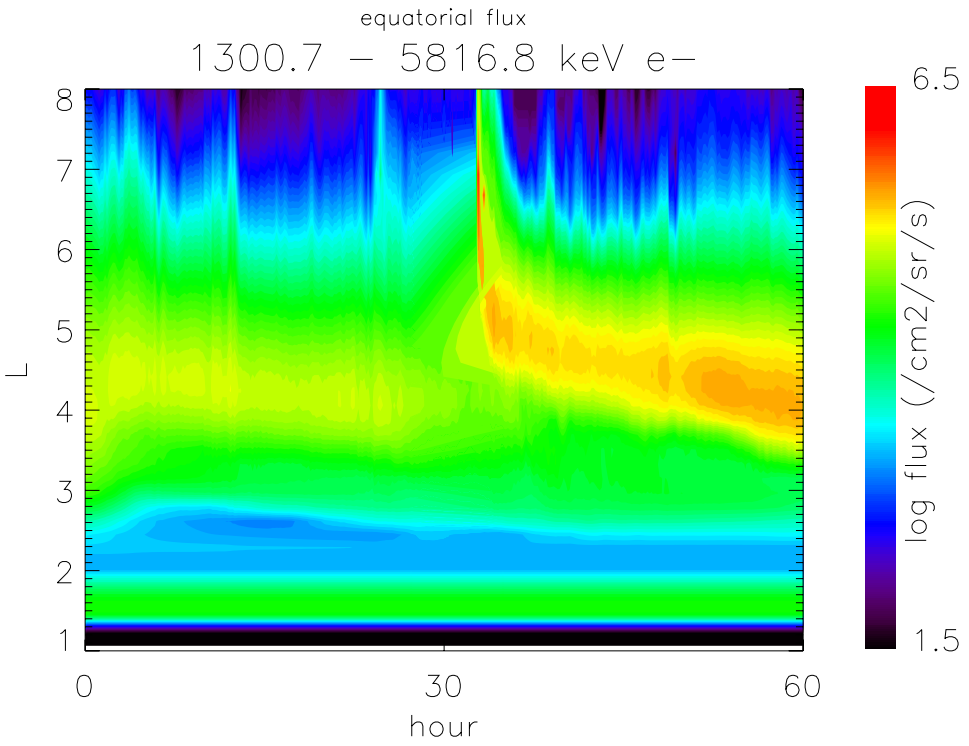

Figure 2.5: A L-shell v. Simulation Time plot of the upper two energy bins of the RBE model during the 23-26 October 2002 Storm. The zero time corresponds to noon on the 23rd

to the injection; frames B through F demonstrate the capture and inward diffusion and convection of the energetic electron flux. The inward motion of the flux appears to occur on an accelerated time-scale, with the captured flux crossing the white line that denotes geosynchronous orbit within about an hour.

Interestingly, the distribution seems to be primarily field-aligned. Drift shell splitting, the process by which perpendicular particles drift further away from the Earth on the dayside, is a likely explanation. The electron flux enters the simulated domain on the night-side, which as a consequence of drift shell splitting, has a field-aligned distribution. As the injection makes it's way inward, the field-aligned pitch angle anisotropy is carried to a large part of the inner magnetosphere. Additionally, slight magnetopause compression resulting from the increased solar wind ram pressure can make the effect more pronounced.

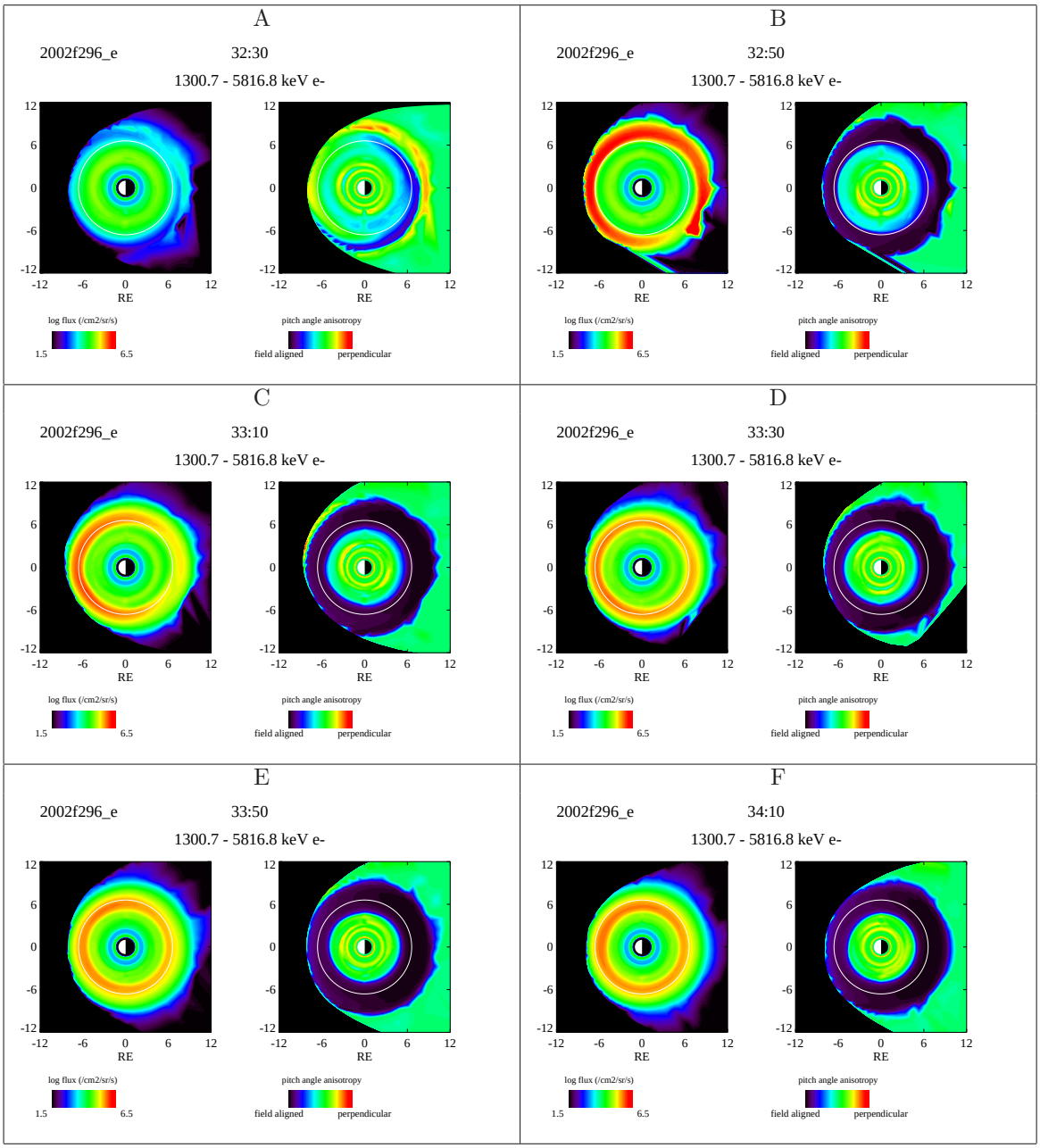

Figure 2.6: Plots A to F show a sequence of equatorial slices of flux and pitch angle anisotropy during the particle injection.

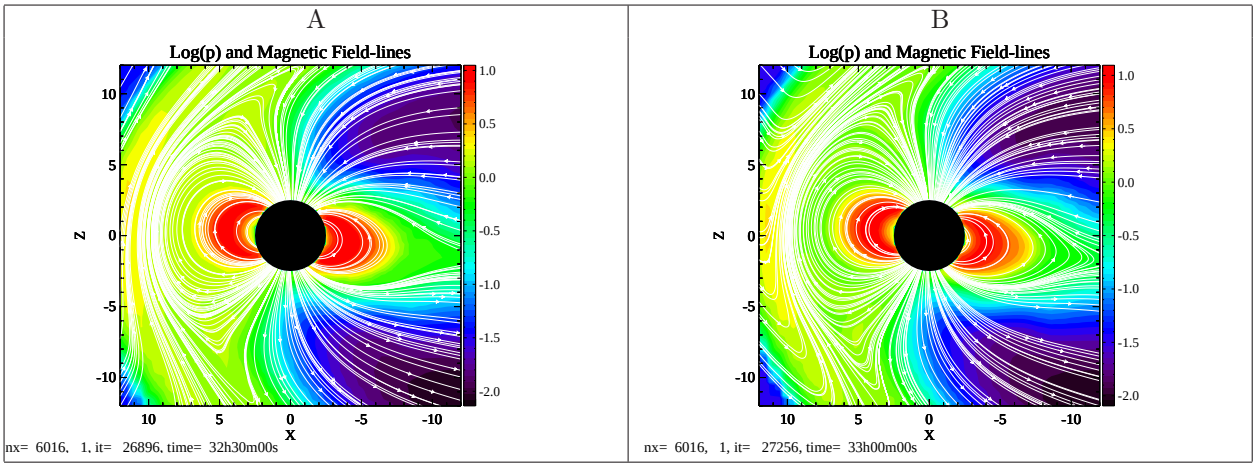

Figure 2.7: Plot A shows the solution immediately before the injection of flux into the magnetosphere, while plot B shows the solution immediately after.

Figure 2.7 shows the configuration of the magnetosphere immediately before and after the flux injection displayed in figure 2.6. Each frame contains a slice along the noon-midnight meridian; the white lines are magnetic field traces, and the color contours indicate the logarithm of pressure. The magnetic field varies significantly during this time period, and certainly affects the radial transport due to the resulting strongly inductive electric field. However, it is not clear that this plays a large role in the capture.

The influx of energetic particles at this time is coincident with the increase in solar wind speed to around 800 km/s. This is to be expected as the night-side outer boundary in the RBE model is assumed to be a kappa function with a characteristic energy given by (Zheng et al., 2003):

$$E_{ps}(t) = 0.016 \times V_{SW}(t - 2hr) - 2.4 \tag{2.1}$$

The result is an increase in energetic electrons at the boundary that are then available to move inward.

The Solar Anomalous and Magnetospheric Particle Explorer (SAMPEX) satellite was taking measurements during this time. SAMPEX is a low earth orbiting satellite

with an 82 degree inclination (Baker et al., 1993). It probes the radiation belts by making observations at the foot-points of field-lines threading the region. The Proton/Electron Telescope (PET) on SAMPEX can measure the 2-30 MeV electron population. Although we are looking at equatorial fluxes instead of fluxes at the ionosphere, Kanekal et al. (2005) has demonstrated that the temporal variation is identical. A comparison of our model with SAMPEX data is therefore reasonable.

The top panel in figure 2.8 shows the SAMPEX fluxes smoothed over 15 orbits. The 2-6 MeV fluxes are shown, which is close to the modeled energy range. Just as with the model a significant dropout is seen late on the 24th, followed by a significant increase in flux between L of 3 and 5. The first part of the data differs significantly from the model, but this is merely due to the RBE model being initialized with the NASA trapped radiation model (AE8MAX) (Vette, 1991; Fung, 1996) rather than the actual data. The rapid capture is also not seen in the data but this may be a results of time scale; the SAMPEX orbit period is about 90 minutes, but the influx of energetic particles happens much faster than that. The overall agreement between the data and model is satisfactory, but there exists significant room for improvement.

We additionally can compare our model to LANL SOPA fluxes. Figure 2.9 shows a scatter plot the electron flux in the .75 to 1.5 MeV energy range of five LANL satellites for 24 October 2002. The average flux at geosynchronous orbit is calculated and over-plotted, as is the averaged simulated flux at approximately 7 R_e. The energy range shown from the model is from 0.6 - 1.3 MeV which is close, but not identical, to the energy range of the data plotted. Because lower energy electrons are included in the model output, we expect to see larger fluxes in the model than in the data. Using a qualitative analysis, we see that there are three significant spikes in the data, including one at around 20 UT near the rapid capture in the

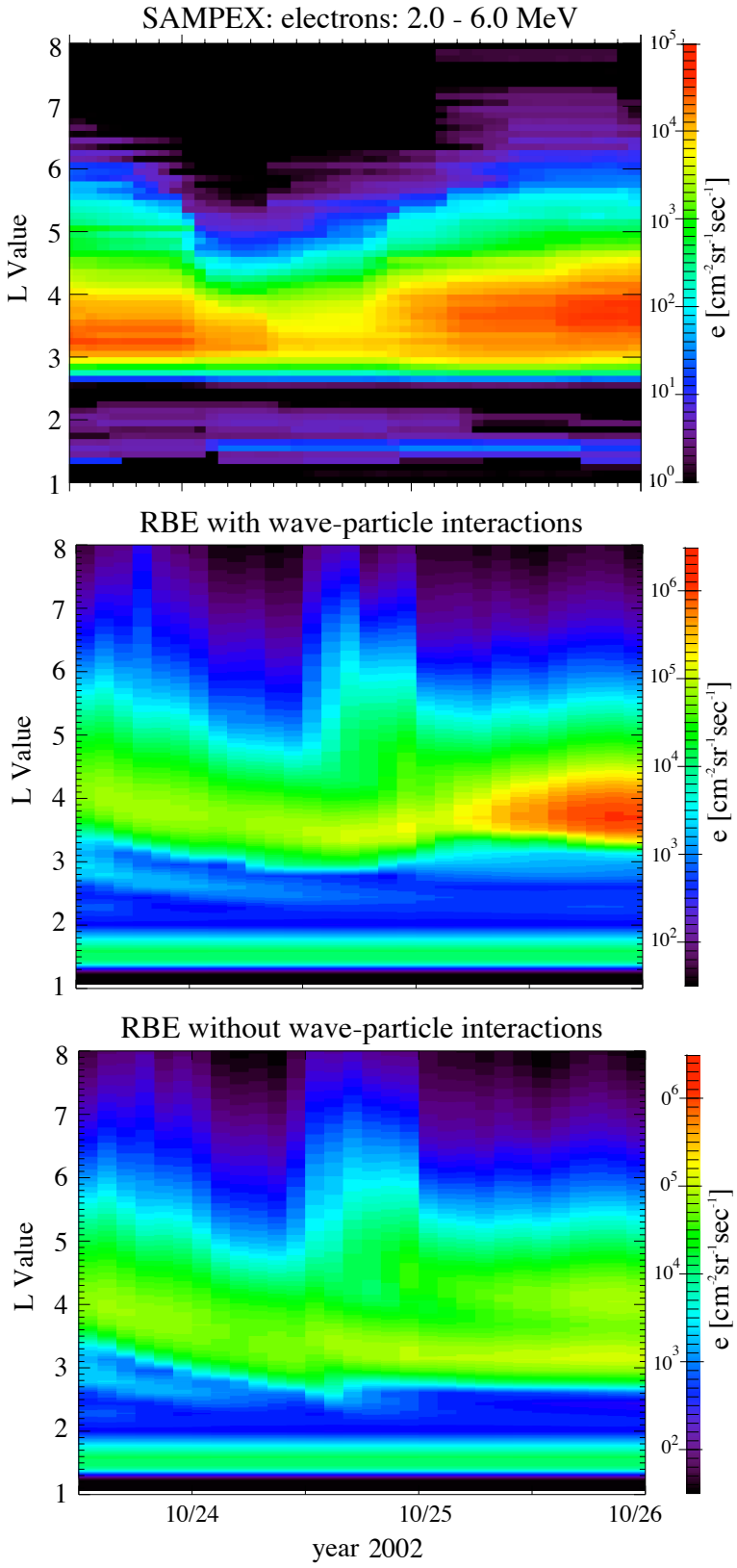

Figure 2.8: Figure taken from Fok et al. (2008). The top panel shows the SAMPEX data, the middle panel shows the RBE model run with a T04 magnetic field and wave-particle interactions, the bottom panel shows the RBE model run with T04 and no wave-particle interactions.

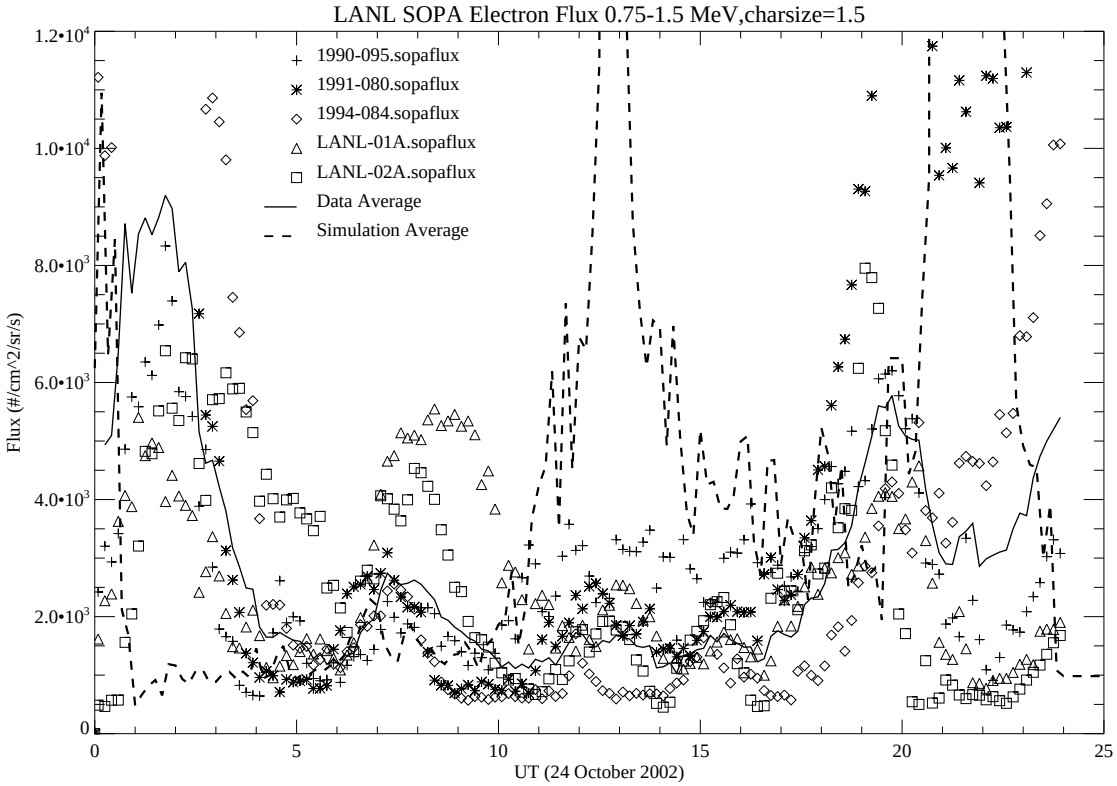

Figure 2.9: A plot showing LANL SOPA electron fluxes together with the average flux at geosynchronous orbit calculated from the simulation. The simulation calculated average uses an energy range from 0.6 to 1.3 MeV.

simulation. The simulation also demonstrates three spikes, two of which are near the spikes seen in the data, and one which is a few hours late. No local acceleration or loss mechanisms are included in the model, but a qualitatively similar time series is reproduced. This result offers a different way to interpret short-lived peaks in the energetic particle flux at geosynchronous orbit. That is, a short-lived spike in either the outer magnetosphere source population, or the radial transport of energetic electron flux, can yield a temporary increase in the measured fluxes at this specific radial distance. This interesting interpretation should certainly be studied more quantitatively in future studies.

Fok et al. (2008) ran the RBE model with the T04 and T96 models for this same time period and found that internal energization sources can be quite significant.

(See the second and third panels of figure 2.8) Wave-particle interactions are not included in the version of the RBE model used in this study. However, based on the study of Fok et al. (2008), we can expect to significantly increase the flux of energetic particles after the dropout on the 24th.

For comparison purposes we can examine our simulation together with the stand-alone simulation results shown in the bottom panel of figure 2.8; The L-Time plots are in the same format. The two major differences between the simulations is the magnetic field model used and how often it is traced. In figure 2.8 the T04 model is used and the field is traced every five minutes, while in figure 2.5 our new approach is used with the field being traced every 10 seconds. Frequent tracing of the magnetic field allows for the inclusion of radial transport effects resulting from rapid changes in the field.

2.5.1 Using a Self Consistent Physics Based Potential Model

Thus far we have focused on coupling the MHD magnetic field calculated by BATS-R-US with the RBE model. We can improve on this scheme by including the RBE's interaction with the IE component of the SWMF represented by a 2D height integrated potential solver given by Ridley et al. (2004). The polar cap potential in the RBE model is now taken from the same ionosphere that is used to set the inner boundary of BATS-R-US and not from an empirical source. In this subsection, we present the results of a simulation of the 23-26 October 2002 storm using the exact same set of parameters, except we now use a new source for polar cap potential.

The results are summarized in figure 2.10. The figure shows the 1.3 to 5.8 MeV electron flux as a function of both time from the start of the simulation and L shell. Moreover, it is in the same format as the model results in figures 2.5 and 2.8. The first half of the simulated time period is comparable to the first half of out previous

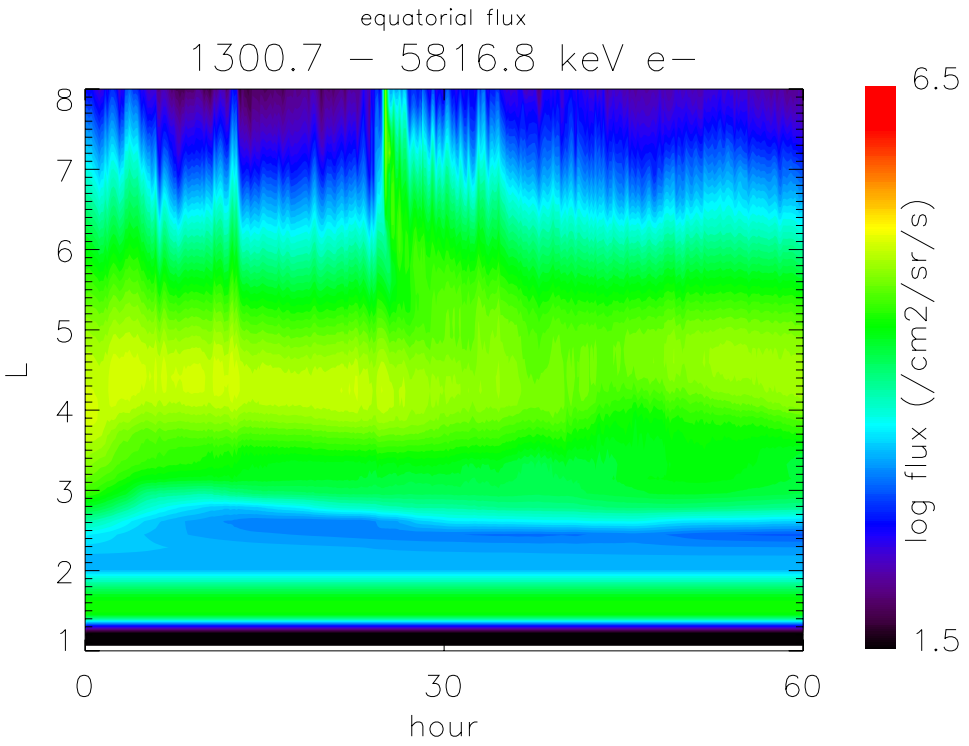

Figure 2.10: A L-shell v. Simulation Time plot of the upper two energy bins of the RBE model with a physics based potential model during the 23-26 October 2002 Storm. The zero time corresponds to noon on the 23rd

simulation. In stark contrast, the second half of the simulated time period exhibits significant difference. The injection of flux featured so prominently in figure 2.5 is hardly seen at all in figure 2.10.

The main difference between the two simulations is the potential model, which makes it the main culprit in explaining the discrepancy. The potentials used in each case are quite similar during the first part of the simulation, but then begin to diverge. Figure 2.11 shows the Weimer empirical potential (Weimer, 1996) used in the first simulation, and the physics based IE potential used in the second simulation at the time of the flux capture (20:40 on 24 October 2002). For comparison purposes, we also show the potential from AMIE (Assimilative Mapping of Ionosphere Electrodynamics). The Weimer pattern and the physics based IE model are very different from each other, and both vary significantly from the AMIE potential. The differing

potentials lead the changes in the strength of convection and the ability of the RBE model to bring flux from the boundary into the model.

Unlike the magnetic field, which has been shown to work well during storm time simulations, we know from Wang et al. (2008) that the IE model's potential pattern becomes increasingly unreliable as the geomagnetic activity increases. Therefore we must significantly improve the IE model in order to take full advantage of this coupling. Unfortunately this is no easy task; Even AMIE potential patterns, which assimilate data into the mapping, were shown by Bekerat et al. (2005) to only adequately represent the DMSP observations about 32% of the time, which is still a remarkable improvement over the performance of empirical models. Nevertheless, comparing this simulation and our first simulation provides an excellent opportunity to examine the impact of different ionospheric potentials on radiation belt dynamics.

We illustrate how the different potential patterns impact the ability of the RBE model to capture flux by examining the drift of an electron near the outer boundary of the model. Using the potential patterns from figure 2.11 we can estimate the electric field on the outer boundary of the RBE model. Figure 2.12 shows a plot of the azimuthal component of the electric field as a function of MLT at 20:40 on 24 October 2002 for both simulations. Negative field strengths correspond to inward $E \times B$ drift, while positive field strengths correspond to outward drift. It is immediately obvious that electrons experience significantly stronger inward drift throughout the majority of the nightside in the simulation driven by the Weimer model compared to the simulation driven by the IE model. This implies that electrons appearing on the outer boundary of the model will penetrate to lower L-shells and have a higher likelihood of being captured into the model in the Weimer driven simulation.

The inclusion of a physics based potential model significantly changes the result.

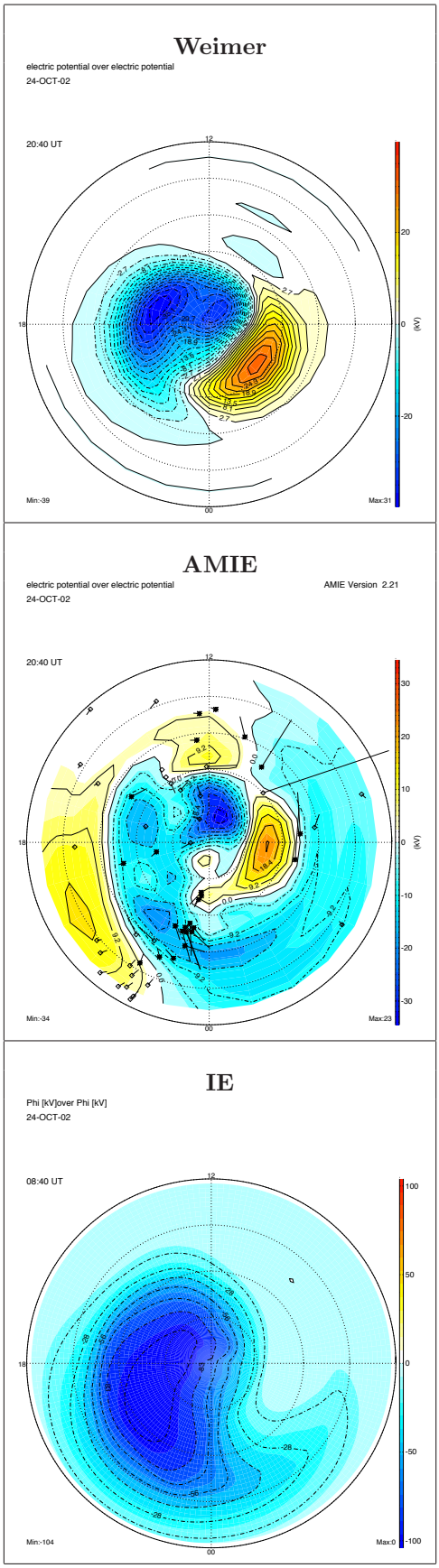

Figure 2.11: Plots of ionospheric potential from Weimer, AMIE and IE at 20:40 on 24 October 2002. The AMIE (Ridley and Kihn, 2004) plot also shows the location of magnetometers used in the inversion. At each of these locations, the input horizontal magnetometer perturbation is drawn, rotated by 90 degrees, to indicate (roughly) the $E \times B$ flow direction.

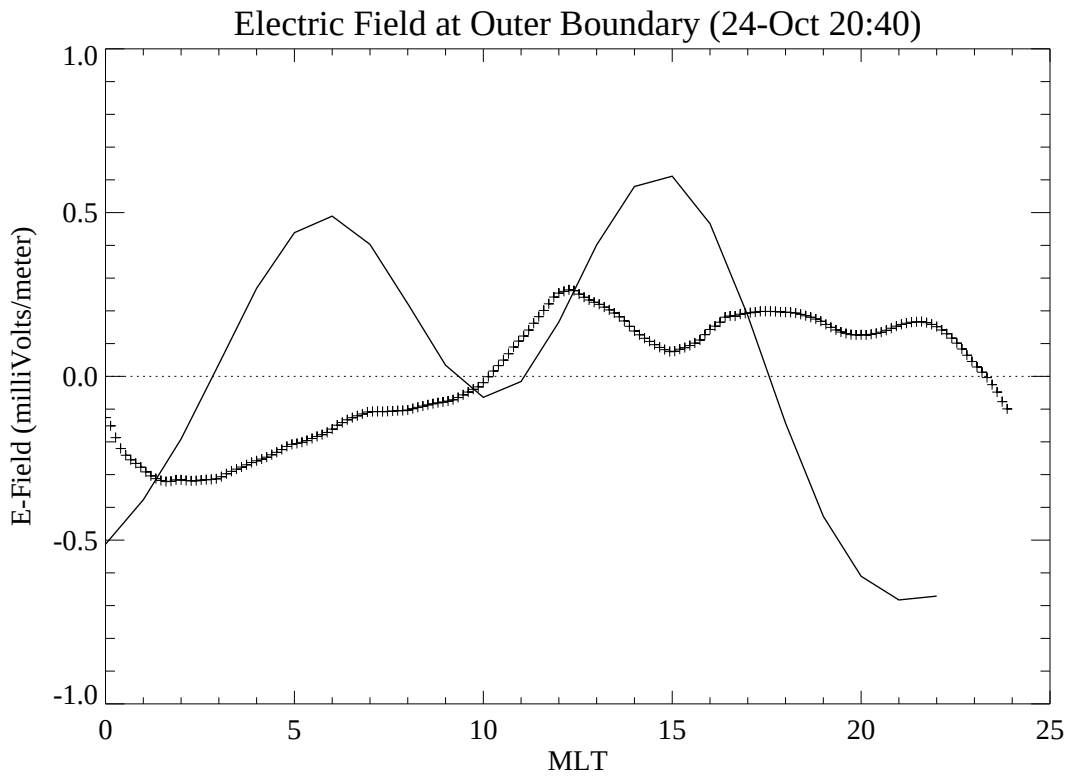

Figure 2.12: A plot of the azimuthal component of the convection electric field on the boundary of the RBE model inferred from the potential plots in figure 2.11. The solid line corresponds to the model driven by empirical Weimer model, and the "+" symbols correspond to the model driven by the physics based IE model.

The source of the change is the different potential patterns, which give rise to altered drifts in the magnetosphere, and effectively modify the solution. Because of the importance of the potential on the solution, it is imperative to accurately model the Magnetosphere-Ionosphere (M-I) coupling.

2.6 Summary and Future Work

We have integrated the RBE model into the SWMF, and described the coupling mechanism. Our newly coupled model allows us to study the radiation belts in a global context. The first application of the model was the 23-26 October 2002 geomagnetic storm.

The most interesting result of the first coupled simulation is the rapid injection of energetic particles. As the solar wind speed increases, the energy of the kappa function that describes the distribution on the boundary increases. The strong inductive electric, resulting from the varying magnetic field, together with the drift calculated from the potential pattern, leads to increased radial transport and convection that is largely responsible for bringing the energized boundary particles into the model. By using a time-dependent magnetic field model that is frequently traced, the radial transport is adequately described.

We have demonstrated reasonable agreement with the SAMPEX data. However, there does exist significant room for improvement. For instance, it is clear that the increase in the energetic particle population is not sufficiently accounted for by only the injection of particles from external sources. Fok et al. (2008) explore the effect of chorus waves as an internal source of energetic particles. They found a significant impact on the simulation results. Future studies utilizing our coupled model should include these effects as well.

We also carried out a second simulation which utilized a self consistently calculated potential from the Ionosphere Electrodynamics (IE) component of the SWMF. The results in this case are significantly altered from the first simulation owing to the strong contrast in the potential patterns. In particular, the capture of energetic electron flux does not happen in this case. The impact of ionospheric potential and M-I coupling on radiation belt dynamics during active times certainly merits further study.

Our newly coupled model opens the door to numerous possibilities. For example, we can self consistently study how large scale changes in the magnetosphere impact the radiation belt solution. From a more applied point of view, the ability of the model to run faster than real-time on a reasonable number of processors introduces the possibility of space weather applications. Because we are using the SWMF, we can also drive our model with the Inner Heliosphere (IH) component instead of satellite data, thereby adding a predictive capability.

Acknowledgements

We would like to thank Dot DeLapp of Los Alamos National Laboratory for providing LANL geosynchronous observations.

CHAPTER III

Modeling Ionospheric Outflow

3.1 Chapter Abstract

Ionospheric outflow can be a significant contributor to the plasma population of the magnetosphere during active geomagnetic conditions. Most Magnetosphere-Ionosphere Coupling (MIC) models do not include this outflow in a physical manner; instead they rely on pressure gradient terms to draw plasma off the inner boundary of the magnetosphere. We present the results of new efforts to model the source and effects of out flowing plasma in the Space Weather Modeling Framework (SWMF). In particular, we use the Polar Wind Outflow Model (PWOM), a field-aligned multi-fluid polar wind code, coupled to the Ionosphere Electrodynamics (IE), and Global Magnetosphere (GM) components of the SWMF. We present our methodology for the MIC, as well as the effect of outflow on the magnetosphere during a geomagnetic storm. Moreover, we explore the use of multi-species MHD to track the resulting plasma composition in the magnetosphere.

3.2 Introduction

Most global magnetosphere models have an inner boundary between 2 and 3 Earth radii. Most ionospheric models only extend up to 1000 km at most. Between these two regions, there exists a modeling gap that is often ignored. The gap includes plas-

maspheric, auroral, and polar cap field-lines, and it is through this region that plasma is accelerated into the magnetosphere providing a source of ionospheric plasma.

There is a preponderance of data studies that demonstrate the relative contribution of ionospheric plasma, entering the magnetosphere through the gap, to make up a significant fraction of the magnetospheric plasma population. Nosé et al. (2003) use data from the Energetic Particle and Ion Composition (EPIC) instrument on board the Geotail spacecraft to examine the O^+/H^+ energy density ratio in the plasma sheet during geomagnetic storms. They found that the ratio can reach 0.3-1.0 at the peak of the storm. Moreover, Nosé et al. (2005) found that during the extreme case of the 29-31 October 2003 super-storm, the O^+/H^+ energy density ratio reached 10-20 at the storm maximum. Daglis et al. (1999) summarizes ring current composition measurements based on AMPTE and CRRES during varying condition and show increased oxygen ions present during active periods (see table 1.1). Pulkkinen et al. (2001) use data from the Polar spacecraft and demonstrate that the O^+ energy density increases with solar variability whereas H^+ and He^+ energy densities do not. These data studies, and other not included here, illustrate the importance of including the ionospheric impacts on the space environment system.

Global models deal with the addition of mass through the gap in different ways. Pressure gradient terms pull plasma off the boundary, centrifugal terms can throw plasma off the boundary, and empirical relationships can be used to specify the mass flow. Section 1.1.1 briefly introduced this topic which we revisit now in greater detail.

The inclusion of ionospheric plasma through pressure gradient, and centrifugal terms is the most common approach to mass coupling between the ionosphere and magnetosphere. As part of a study carried out by Zhang et al. (2007), the inner boundary density of the BATS-R-US magnetosphere model was modified from 5

to 10 amu/cm^{-3}. By increasing the available amount of plasma to be drawn into the magnetosphere, they effectively simulate the impact of ionospheric plasma. The resulting Dst index was found to decrease with the increasing mass source.

Modifying the total inner boundary density serves as a crude approximation to the actual source of ionospheric plasma, but the approach has a number of drawbacks. First, changing the inner boundary in an ad-hoc fashion may yield accurate results, however causality is sacrificed; Is the inner boundary density high because of magnetospheric conditions, or are the conditions in the magnetosphere a result of the ionospheric boundary? Composition information of the ionosphere source is also lost. Oxygen ions make up a large fraction of the composition in the inner magnetosphere and ring current during geomagnetically active times (Lennartsson, 1997; Daglis et al., 1999; Fuselier et al., 2003). To accurately study the impact of composition, the source population must preserve the component information, and the magnetosphere model must track the composition as it propagates.

The use of empirical models to set the ion outflow rate is another approach to mass coupling between the ionosphere and magnetosphere. A study by Gagne (2005) utilized the relationship of Strangeway et al. (2000) which relates the Poynting flux with cusp related oxygen ion outflow. The LFM model calculates the Poynting flux which is in turn used to determine the ion outflow, which is then handed back to the LFM magnetosphere model. A similar approach is also used by Moore et al. (2007). In their study the resulting outflow is tracked using a particle tracing code and the LFM magnetic field rather than using the MHD code directly.

The use of empirical models to set the ion outflow rate possesses several advantages; the ionospheric source rate depends on magnetospheric conditions, the rate will correlate well with data, and it varies in a realistic manner. The drawbacks

of this approach are that the mechanisms for the acceleration are ignored, and the causal chain is difficult to follow.

These methods each have advantages and disadvantages, but one thing that they all have in common is that none is a first principals based approach. The main scientific goal of this chapter is to include the plasma acceleration through the gap region in a self-consistent manner, and to then study the resulting effect on the space environment.

We accomplish our objective using a multistage approach. First, we develop a field-aligned model that can obtain the solution along a single field line in the gap region based on the work of Gombosi et al. (1985). That model is expanded to solve multiple field lines in parallel, effectively filling the region. We call our new model the Polar Wind Outflow Model (PWOM).

3.3 Polar Wind Modeling Overview

We focus on the polar wind outflow in this study; Therefore a brief overview is warrented here. The polar wind refers to the supersonic outflow of particles along open magnetic field lines at high latitude, and can account for an important ionospheric source. First suggested by Axford (1968) and Banks and Holzer (1968), and demonstrated experimentally by Hoffman (1970), many models of the terrestrial polar wind have been developed over the years. Gombosi et al. (1985) introduced a time dependent field aligned model that has been subsequently used to investigate the importance of many physical parameters on the polar wind.

The Polar Wind Outflow Model (PWOM) that we developed and describe latter in this chapter has its roots in the work of Gombosi et al. (1985). This model has been used to investigate many features of the polar wind over the years. First, Gombosi

(1988) added the ability to study field aligned currents. Then, Cannata and Gombosi (1989) used this model to investigate the effect of solar cycle on the polar wind. These results were latter found to be qualitatively consistent with measurements taken by the Akebono satellite in a paper by Abe et al. (2004). Gombosi et al. (1991) included helium ions into the model.

Many other terrestrial field aligned models were developed, utilizing generalized transport, fluid, and kinetic approaches. For instance, Schunk (1981) uses a time independent formulation based on the 13 moment transport equations. By allowing 13 moments for electrons and fewer for ions, they could study electron anisotropies, and simulate a supersonic polar wind. Mitchell and Palmadesso (1983) and Ganguli et al. (1987), introduce time dependent models using 13 and 16 moment solutions respectively. A collisional kinetic model of the polar wind is presented by Pierrard and Lemaire (1998), and used to study the escape of H^+. A good review of polar wind models and measurements can be found in Ganguli (1996).

Terrestrial polar wind models demonstrate that several non-classical effects can impact polar wind results significantly. Centrifugal acceleration resulting from flux tube convection across the polar cap can contribute to outflow of oxygen ions (Cladis (1986), Horwitz et al. (1994)). Gombosi and Killeen (1987) demonstrate that friction heating can also lead to transient outflow of oxygen ions. As demonstrated by Ganguli and Palmadesso (1987) and others, wave particle interaction can also affect plasma outflow. Indeed, Barakat and Barghouthi (1994) use a Monte Carlo model to establish a strong connection between the flux oxygen ions and wave-particle interaction. In some cases the polar wind distribution can become non-Maxwellian. Barakat et al. (1995) show that in the transition region where the flow becomes supersonic, the distribution function becomes double humped.

Three dimensional models of polar wind have also been developed. Schunk and Sojka (1989) solve along various field lines convecting throughout the polar cap potential pattern. By tracking these field lines, they are able to obtain a three dimensional description of the polar wind. Gardner and Schunk (2005) solve a fully three dimensional model instead of tracking individual flux tubes. They also include the neutral polar wind, or the neutral particles flowing with the polar wind as a result of charge exchange, in their model. Both of these models solve the continuity and momentum equations, and use an adiabatic equation of state. Also, a simplification of the perpendicular momentum equation is employed by setting the perpendicular velocity equal to the $\mathbf{E} \times \mathbf{B}$ drift.

3.4 Solving a Single Field-Line

The first step towards obtaining a solution in the gap region is to obtain a solution to a single field-line. The base of the field-line is in the ionosphere at about 250km while the top of the field-line is located at a few earth radii, effectively spanning the gap.

To obtain the solution in the vertical direction we solve the gyrotropic transport solution given by (Gombosi and Nagy, 1989):

$$\frac{\partial}{\partial t}\left(A\rho_i\right) + \frac{\partial}{\partial r}\left(A\rho_i u_i\right) = AS_i \tag{3.1}$$

$$\begin{aligned} &\frac{\partial}{\partial t}\left(A\rho_i u_i\right) + \frac{\partial}{\partial r}\left(A\rho_i u_i^2\right) + A\frac{\partial p_i}{\partial r} = \\ &\quad A\rho_i\left(\frac{e}{m_i}E_\parallel - g\right) + A\frac{\delta M_i}{\delta t} + Au_iS_i \end{aligned} \tag{3.2}$$

$$\begin{aligned}
&\frac{\partial}{\partial t}\left(\frac{1}{2}A\rho_i u_i^2+\frac{1}{\gamma_i-1}Ap_i\right)+\frac{\partial}{\partial r}\left(\frac{1}{2}A\rho_i u_i^3+\frac{\gamma_i}{\gamma_i-1}Au_i p_i\right)\\
&\quad=A\rho_i u_i\left(\frac{e}{m_i}E_\parallel-g\right)+\frac{\partial}{\partial r}\left(A\kappa_i\frac{\partial T_i}{\partial r}\right)+A\frac{\delta E_i}{\delta t}\\
&\quad+Au_i\frac{\delta M_i}{\delta t}+\frac{1}{2}Au_i^2S_i
\end{aligned}\tag{3.3}$$

$$\begin{aligned}
E_\parallel=&-\frac{1}{en_e}\left[\frac{\partial}{\partial r}\left(p_e+\rho_e u_e^2\right)+\frac{A'}{A}\rho_e u_e^2\right]+\\
&\frac{1}{en_e}\frac{\partial}{\partial r}\left(\sum_i\frac{m_e}{m_i}\left[\left(u_e-u_i\right)S_i-\frac{\delta M_i}{\delta t}\right]+\frac{\delta M_e}{\partial t}\right)
\end{aligned}\tag{3.4}$$

The subscript 'i' and the subscript 'e' refer to the ion and electron species respectively. With regard to the other symbols, m is molecular mass, ρ is mass density, u is velocity, T is temperature, p is pressure, e is particle charge, r is the distance along the field line, A is the cross-sectional area, κ is the heat conductivity, γ is the specific heat ratio, k is Boltzmann's constant, $E_\parallel$ is the ambipolar electric field, g is the gravitational acceleration, S is the mass production rate, $\frac{\delta M}{\delta t}$ is the momentum exchange rate, given by Schunk and Nagy (2000) as

$$\frac{\delta M_i}{\delta t}=-\sum_j\rho_i\nu_{ij}\left(u_i-u_j\right)\tag{3.5}$$

and $\frac{\delta E}{\delta t}$ is the energy exchange rate, given by Schunk and Nagy (2000) as

$$\frac{\delta E_i}{\delta t}=\sum_j\frac{\rho_i\nu_{ij}}{m_i+m_j}\left[3k\left(T_j-T_i\right)+m_j\left(u_i-u_j\right)^2\right]\tag{3.6}$$

Here we assume that the neutrals are at rest. The gyrotropic transport equations (3.1 through 3.4) depend on the cross-sectional area A. A is inversely proportional to the magnetic field strength, and using a dipole assumption we have

$$A=\alpha r^3\tag{3.7}$$

where α is a constant.

Equations 3.1 through 3.3 refer to the continuity, momentum, and energy equations respectively. Equation 3.4 determines the ambipolar electric field. Note, that the first term in 3.4, dependent on the electron pressure gradient, is the dominant term and frequently used by other models for the electric field.

Unlike the ions, the electrons are not solved for using the transport equations. Rather, they are solved using charge neutrality, a steady-state electron velocity assumption, and an energy equation:

$$n_e = \sum_i n_i \tag{3.8}$$

$$u_e = \frac{1}{n_e}\left(\sum_i n_i u_i - \frac{j}{e}\right) \tag{3.9}$$

$$j = j_0 \frac{A_0}{A} \tag{3.10}$$

$$\rho_e \frac{\partial T_e}{\partial t} = (\gamma_e - 1)\frac{m_e}{kA}\frac{\partial}{\partial r}\left(A\kappa_e \frac{\partial T_e}{\partial r}\right) - \rho_e u_e \frac{\partial T_e}{\partial r} - T_e\left[S_e + \frac{\gamma_e - 1}{A}\rho_e \frac{\partial}{\partial r}(A u_e)\right] + (\gamma_e - 1)\frac{m_e}{k}\frac{\delta E_e}{\delta t} \tag{3.11}$$

where j is the current density, and the subscript 0 represents the value taken at a reference altitude. Expression 3.10 enforces conservation of field aligned currents. Equation 3.8 represents the quasi-neutrality of the plasma, and substitutes for the continuity equation. Similarly, Equation 3.9 obtains the electron velocity from the ion flux and current, and takes the place of the electron momentum equation. Finally, Equation 3.11 obtains the electron temperature from conduction, advection, adiabatic heating, and energy transfer due to chemical reactions (see table 3.1).

Solving this system of coupled differential equations yields the density, velocity and temperature for ionospheric O^+, H^+, He^+ and e^- along a field-line.

Reaction			Reaction Rate
$O + h\nu$	$\rightarrow$	$O^+ + e^-$	$I(\chi)$
$He + h\nu$	$\rightarrow$	$He^+ + e^-$	3.9×10^{-8}
$O + N_2$	$\rightarrow$	$NO^+ + N$	1.2×10^{-12}
$O^+ + O_2$	$\rightarrow$	$O_2^+ + O$	2.1×10^{-11}
$He^+ + O_2$	$\rightarrow$	$O^+ + O + He$	9.7×10^{-10}
$He^+ + N_2$	$\rightarrow$	$N_2^+ + He$	5.2×10^{-10}
$H^+ + O$	$\leftrightarrow$	$H + O^+$	$P(H^+) = 2.5 \times 10^{-11} T^{1/2}$, $L(H^+) = 2.2 \times 10^{-11} T^{1/2}$

Table 3.1: Chemistry in the Earth polar wind model. The reaction rates are taken from Schunk and Nagy (2000)

3.5 Solving Multiple Field-Lines in Parallel

Obtaining a vertical solution along a single field-line gives only a very localized solution in the gap region. To reconstruct the full three dimensional solution, we solve several field-lines in parallel.

Each field-line that it tracked in the PWOM must be advected around the polar cap. The motion is determined through a combination of the co-rotation and the drift velocity given by:

$$u_{E\times B} = -\frac{\mathbf{E}\times\mathbf{B}}{B^2}$$

The electric field needed for the convection velocity is determined from the polar cap potential pattern which can either come from a file, the Weimer empirical model, or the IE component of the SWMF as detailed in the next section. Using the convection velocity is the same as using a simplified momentum equation for the horizontal solution.

To ensure efficient use of computational resources, we utilize the Message Passing Interface (MPI). Since there is no communication between field-lines, the model exhibits ideal scaling. In other words, if the number of processors increases then the computational time decreases proportionally. The only limit on the scaling is that the number of processors cannot exceed the number of field-lines.

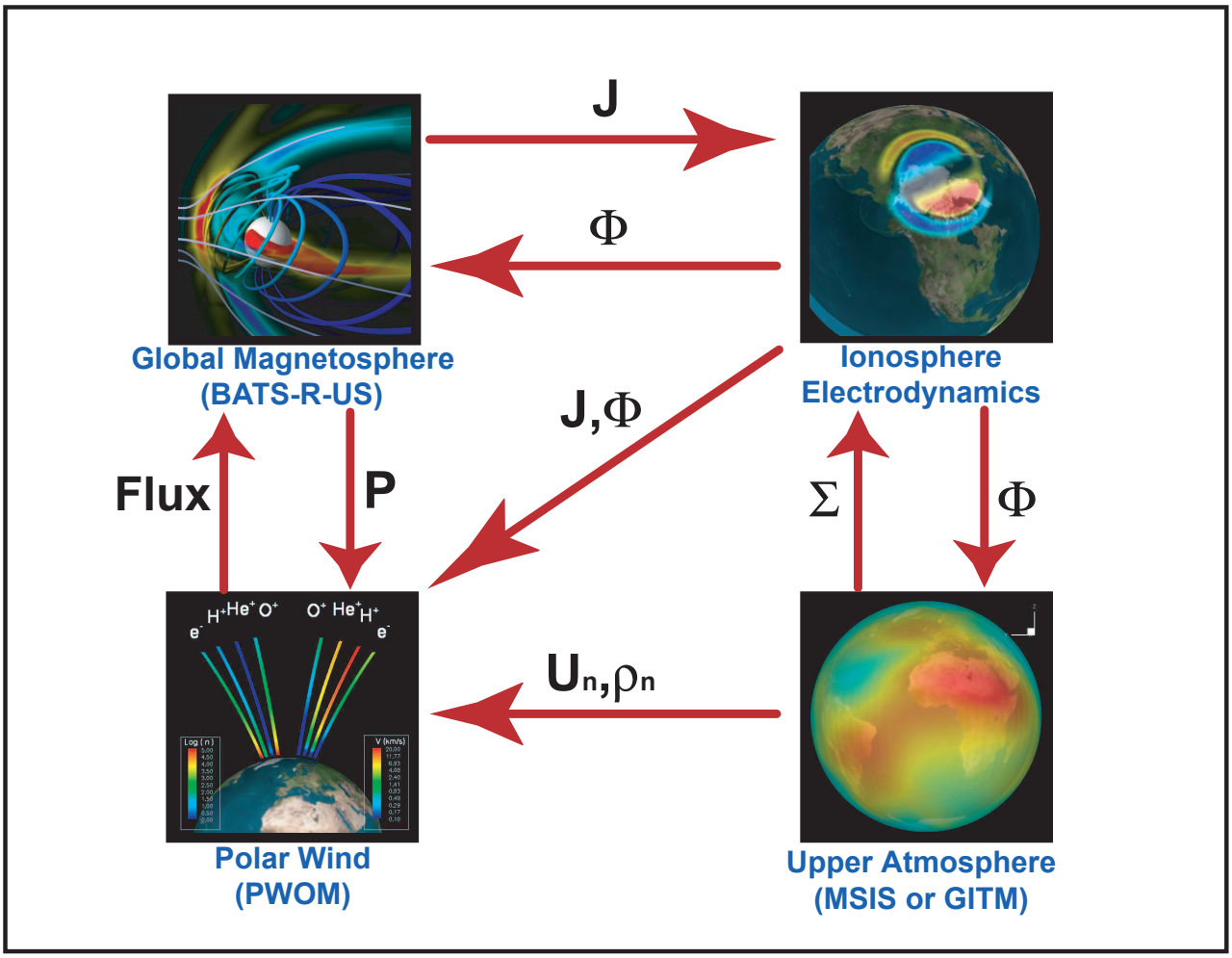

Figure 3.1: A schematic of the information exchange between components

3.6 Incorporating the PWOM into the SWMF

One of the features of the PWOM is its ability to include input from other models. To facilitate the exchange of information, we incorporate the PWOM into the SWMF. Figure 3.1 demonstrates the information flow between models, and is a schematic of the relevant couplings.

We focus on the lower left portion figure 3.1 which represents the PWOM. Input from the Ionosphere Electrodynamics component is delivered in the form of polar cap potential and field aligned currents at low altitude. The gradient of the potential

pattern is taken to determine the electric field, which in turn is used to help calculate the ionospheric convection. The foot points of the individual field-lines in the PWOM are moved accordingly. Field aligned currents from the IE component are used in equation 3.9 to calculate the vertical solution along each field-line.

The PWOM also takes input from the Upper Atmosphere (UA) component. The neutral densities are used to calculate the chemical sources and losses according to the reactions in table 3.1. The neutral winds are used to calculate the Joule heating term in the energy equation. Currently, we use the MSIS empirical model to obtain the neutral densities and and assume that the neutrals are stationary. In the future we will improve on this technique by replacing the empirical model with the physics based Global Ionosphere Thermosphere Model (GITM) (Ridley et al., 2006).

The resulting fluxes at the top of the PWOM are then used to set the inner boundary of the Global Magnetosphere (GM) component. There are several challenges involved with incorporating the fluxes into GM. One such challenge is the differing grid. The BATS-R-US model, which represents the GM component, uses a structured Cartesian grid while the PWOM has a totally unstructured grid in the horizontal direction. In order to interpolate between the two we need to triangulate a grid onto the distribution of field-lines every time the components are coupled. Figure 3.2 shows an example of the triangulation at the beginning and end of a simulation. Another challenge to the GM-PW coupling is putting multi-fluid output of PW into GM. BATS-R-US is usually configured for single-fluid MHD; All the fluxes coming from the PW component then need to be combined into a single-fluid density and velocity. BATS-R-US can also be configured for multi-species or multi-fluid MHD. In these cases the output from the PW component is included by either splitting the densities and using a combined velocity, or using split densities and velocities

respectively.

In principle, the pressure at the inner boundary of the GM component can be fed back to set the upper boundary of the PW component. The resulting pressure change at the upper boundary can either draw additional ionospheric plasma out of the PWOM or act as a cap inhibiting the flow. However this feature still requires testing, and accordingly is not used in any of the studies mentioned in this chapter.

3.7 Results: Steady State

The first step in understanding the capabilities of our newly coupled model is study a few steady state cases. By simulating a few situations with constant input conditions, we can examine the fundamentals of the model's behavior. Two such cases are considered: First, a single stationary field-line is studied under solar maximum and minimum condition. Second, we examine a case with multiple advecting field-lines during quiet solar wind conditions.

A study by Cannata and Gombosi (1989) examined the dependence of polar wind outflow on the solar cycle. As a test that our model is behaving as expected, we reproduce their study here. A single, stationary, field-line at 80 deg latitude and 0 deg longitude is studied under solar maximum conditions and solar minimum conditions. As a proxy for the solar cycle, we vary the F10.7 flux from 60 at solar minimum to 180 at solar maximum. Increasing the F10.7 flux increases the solar EUV input to the atmosphere, increasing both ionization sources and the neutral temperatures. The resulting impact on the polar wind solution is summarized in figure 3.3.

The plots in figure 3.3 demonstrate that increasing the EUV input leads to an order of magnitude increase in the O^+ flux and a slight decrease in the H^+ flux. The reasons behind these changes in the flux are easily explained with a simple physical

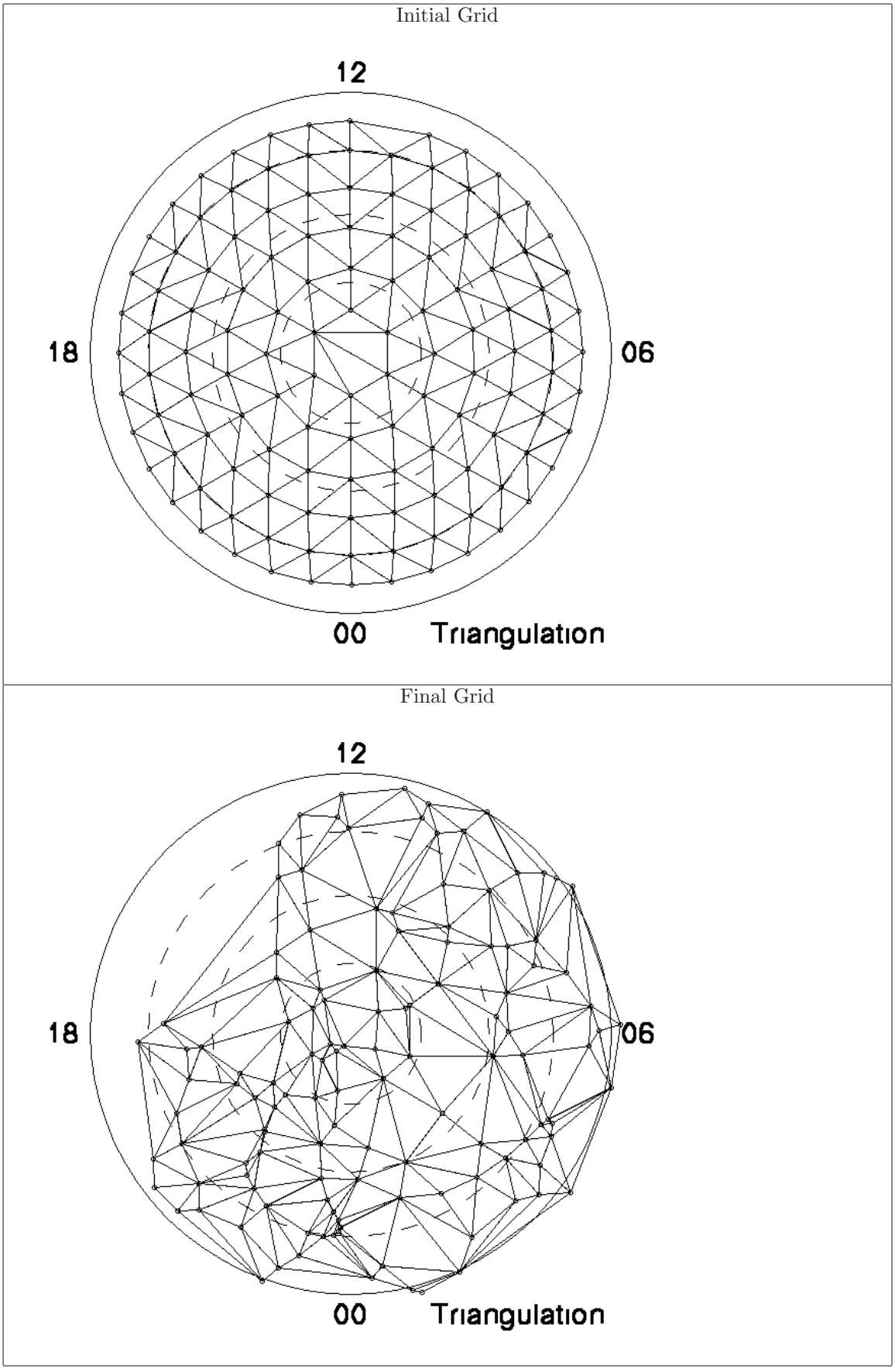

Figure 3.2: The grid triangulated onto the horizontal distribution of field-lines tracked by PWOM. The upper plot shows the initial grid, and the lower plot shows the final distribution after several hours of simulation.

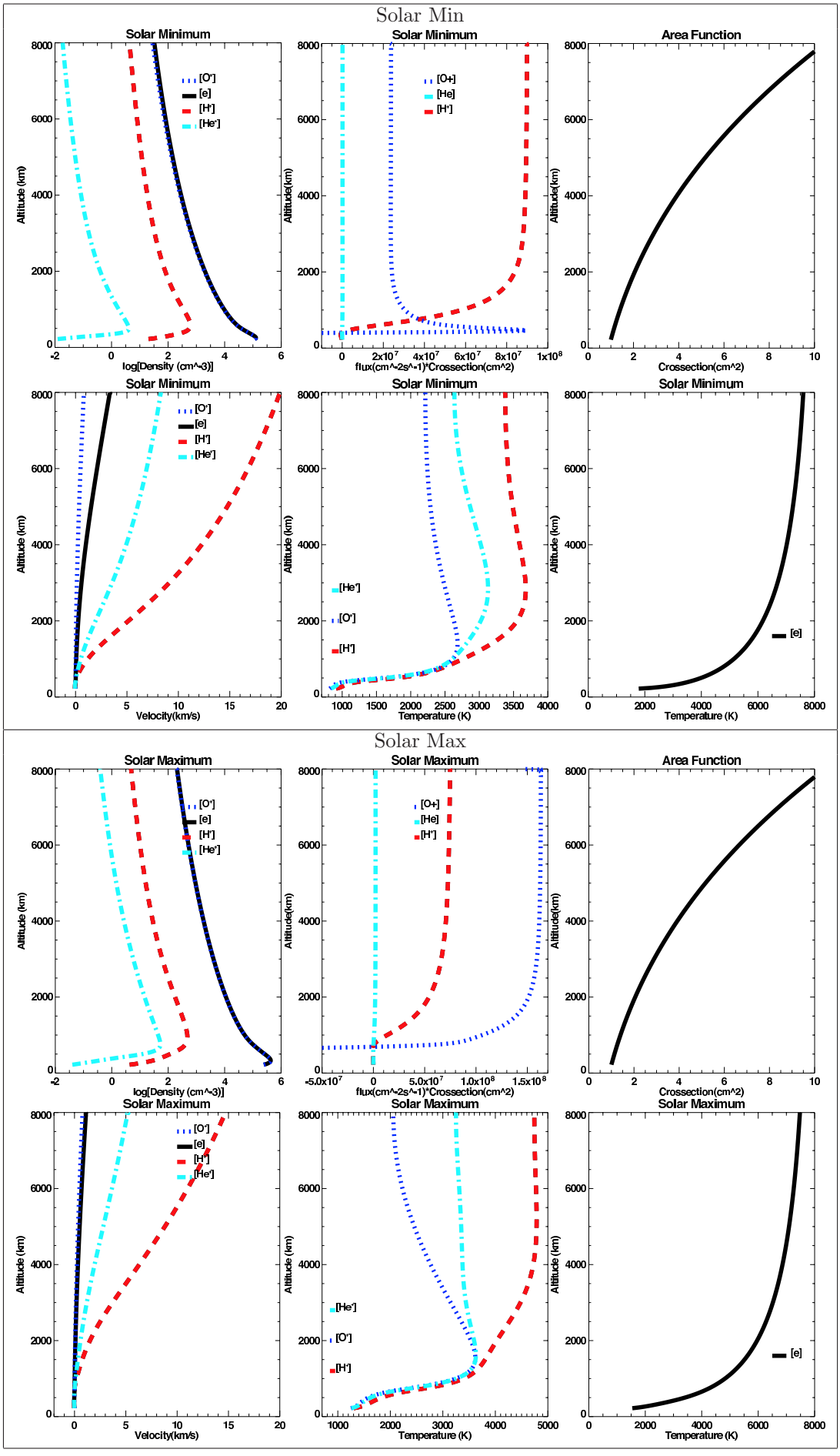

Figure 3.3: A steady-state results for a single field-line at 80 degrees latitude and 0 degrees longitude.

picture. Increasing the EUV input increases the ionization source for O^+ in the polar wind. On the other hand, the thermosphere heats up and expands increasing the collisional regime where the outflow is impeded. The increased ionization source is dominant over the drag resulting in an increased outflow for O^+. The situation for H^+ is slightly different. The friction term due to the collisions still increases, however, the source term does not increase as much. The result is a slight decrease in the net H^+ flux. These results are entirely consistent with those of Cannata and Gombosi (1989) and compares well with Akebono satellite measurements as indicated by Abe et al. (2004).

The next step is to study the model results for a quiet time situation where multiple field-lines are being advected. We consider 125 individual field-lines and run the simulation for 8 hours. The final result is shown in figure 3.4. The H^+ number flux is larger than the O^+, but the since oxygen is 16 times heavier than hydrogen, the mass flux is comparable. The flux of H^+ is higher on the day-side than the night-side while the O^+ flux displays significantly less variability.

It is important to note that this model only simulates the polar wind type outflow solution, and does not account for cusp outflows due to wave-particle interactions. Nonetheless, the impact on the magnetosphere is significant, as the study in the next section will demonstrate.

3.8 Results: 4 May 1998 Storm

Observations have shown that during a geomagnetic storm ionospheric outflow can be the dominant contributor to the magnetosphere plasma composition (Kistler et al., 2005). It is therefore appropriate to test our newly coupled model on an actual geomagnetic storm to see how the ionospheric outflow affects the magnetospheric

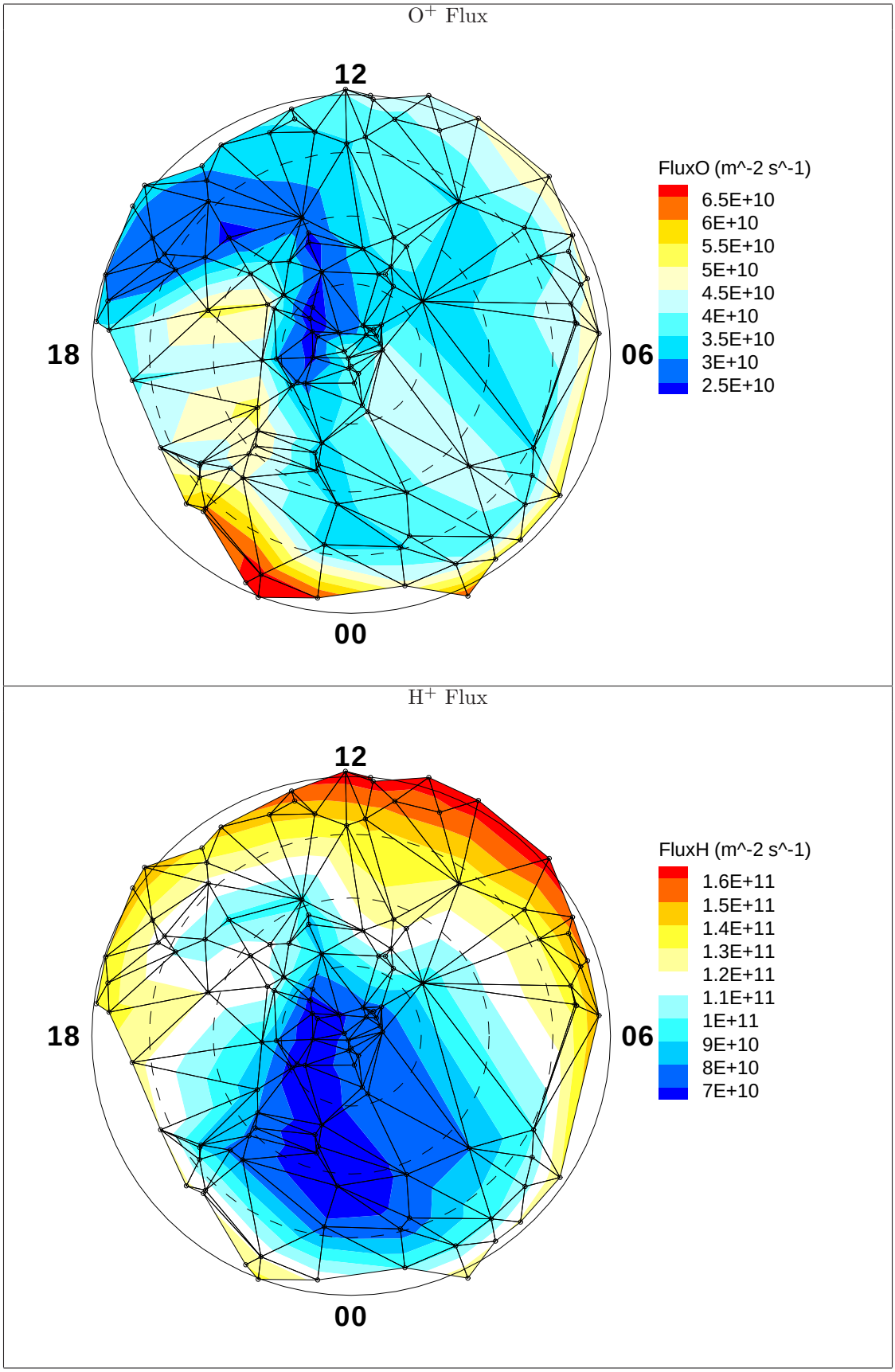

Figure 3.4: A steady-state result for multiple field-lines. Altitude slices of ion fluxes at 8,000 km are shown.

solution. The particular storm chosen for this study is the 4 May 1998 storm.

For this simulation we use the SWMF configured with the PW, GM, IE, and IM components. The GM component is configured to solve the multi-species MHD equations where separate continuity equations are used for O^+ and H^+, but they share a common momentum and energy equation. In this way we can track the individual species without solving the full multi-fluid MHD equations. Additionally, the components are coupled every ten seconds allowing for frequent exchange of information over the course of the simulation. Figure 3.5 shows the solar wind conditions that set the upstream boundary condition for the magnetosphere.

Figure 3.6 shows the log of the mass density along with magnetic field traces at various points during the storm. Unlike traditional MHD simulations, we can take advantage of the multi-species nature of the simulation and track the composition of the density in the magnetosphere, and not just the overall density. Figures 3.7 and 3.8 show the total number density and the corresponding percentage of oxygen ions. The density of Helium ions is miniscule, therefore the remaining number density is H^+. The initial amount of O^+ in the simulation is very small, but when the storm simulation begins the magnetosphere begins to fill with O^+. Eventually O^+ composes the majority of the magnetosphere population.

In order to see the impact of ionospheric outflow on the magnetosphere we compare the impact on specific satellites. In particular, we examine magnetic field data from the GOES satellites compared with simulation output. A simulation with no ion outflow is included as a control case. Direct data model comparisons are shown for GOES 8 (Figure 3.9) and GOES 9 (Figure 3.10). At first sight it is clear that the agreement between the data and model improves significantly when the ionospheric outflow is included. Moreover, when the root mean square (RMS) errors

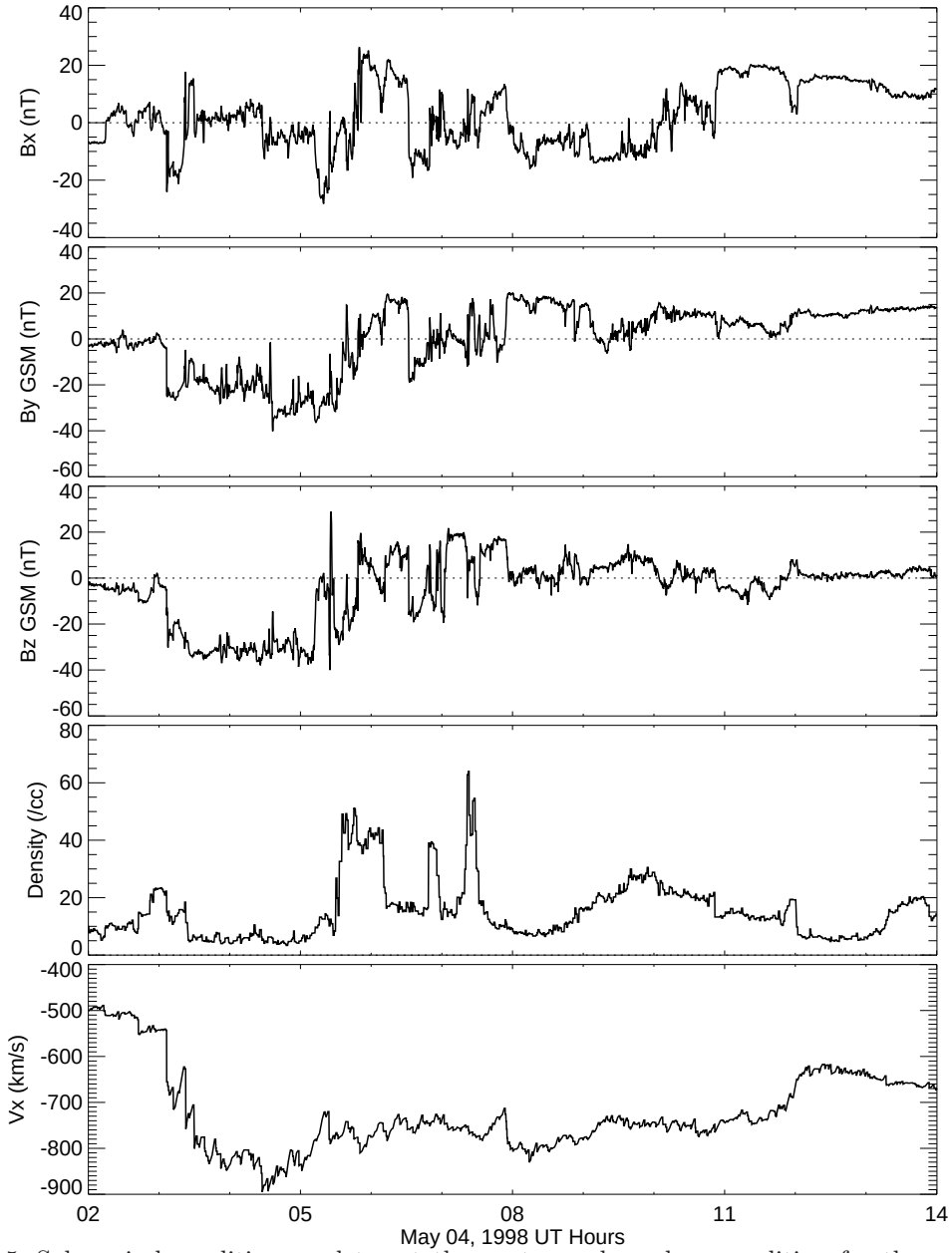

Figure 3.5: Solar wind condition used to set the upstream boundary condition for the magnetosphere for the 4 May 1998 Storm

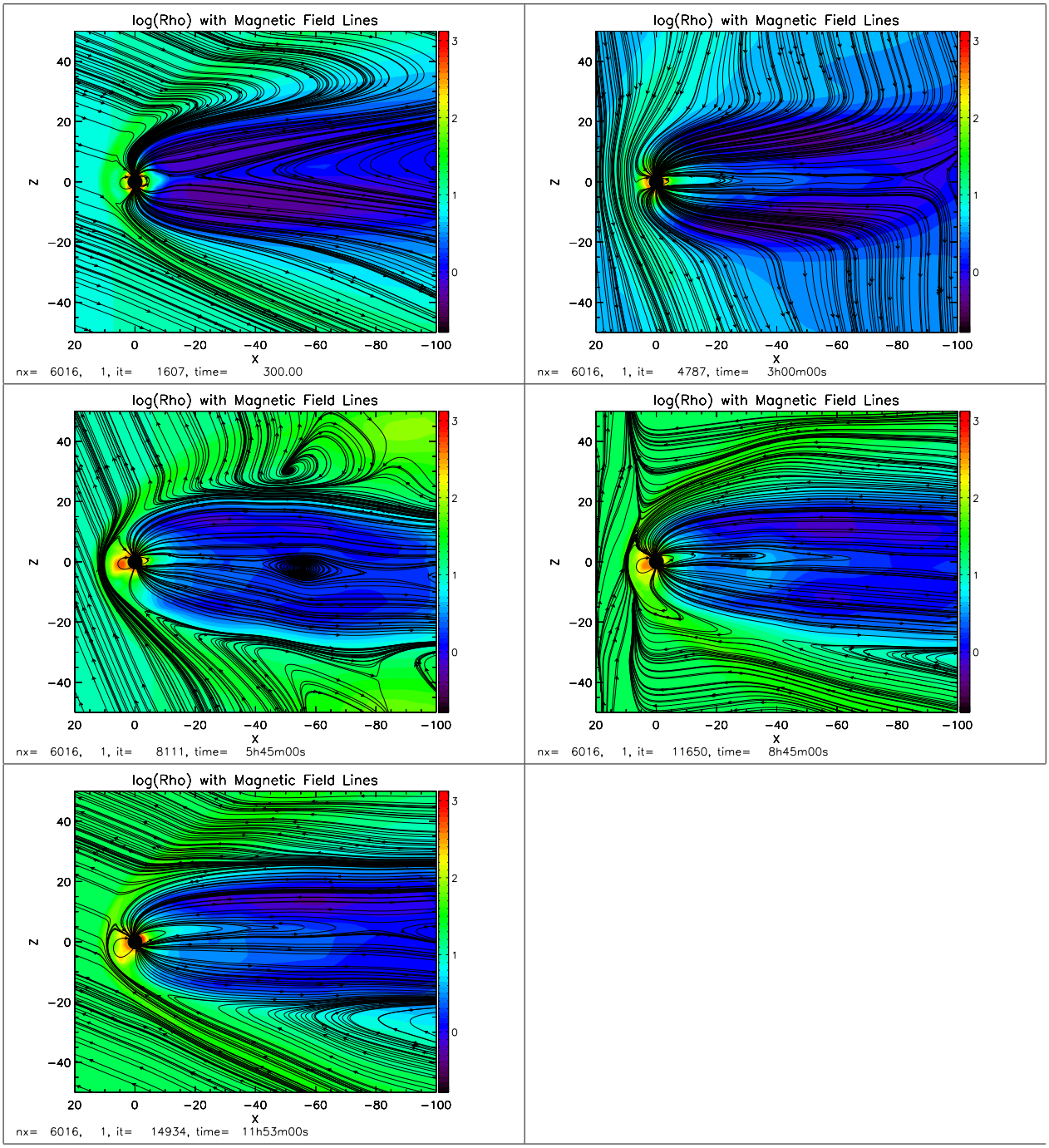

Figure 3.6: Log of mass density and magnetic field-lines in the noon-midnight y=0 plane

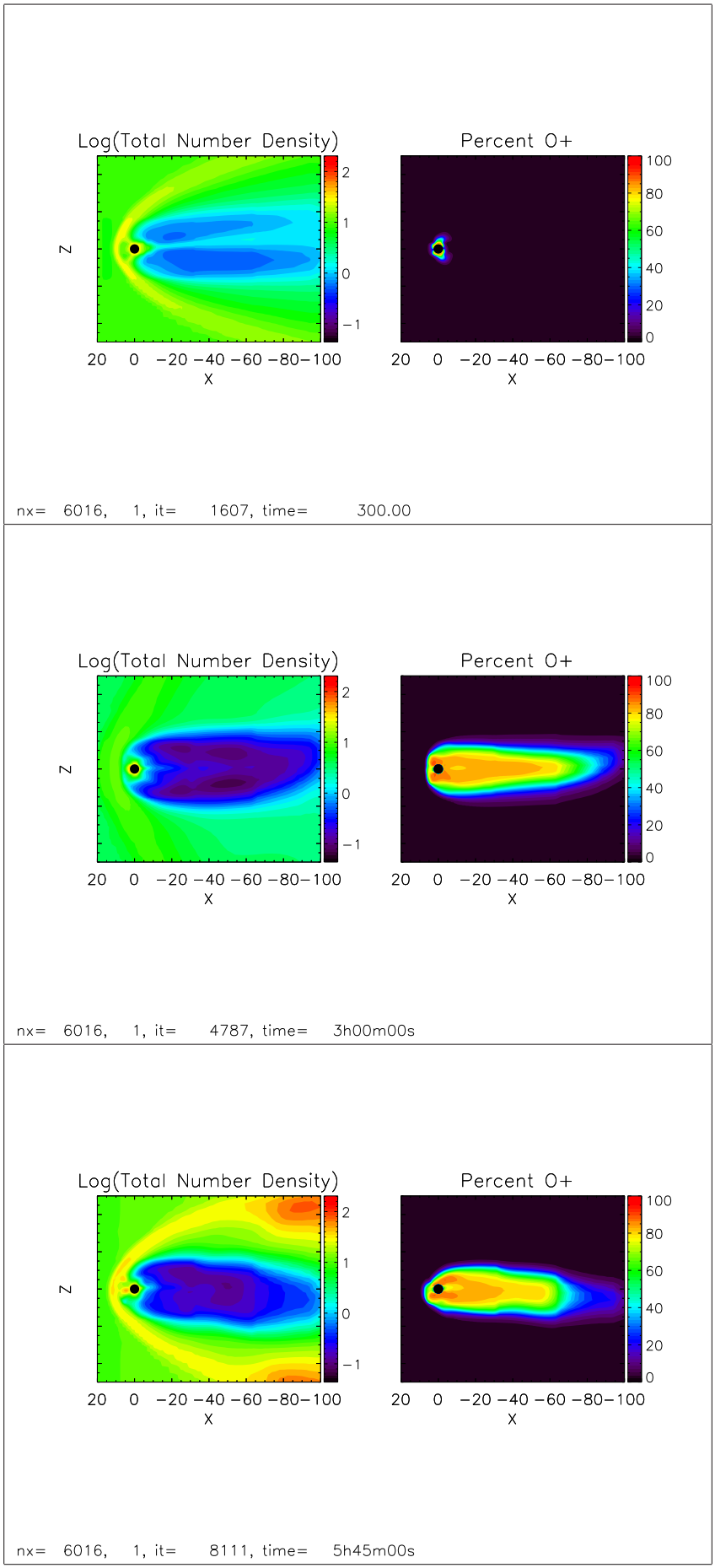

Figure 3.7: Log of number density and the percent of oxygen ions in the magnetosphere. The y=0 plane is shown.

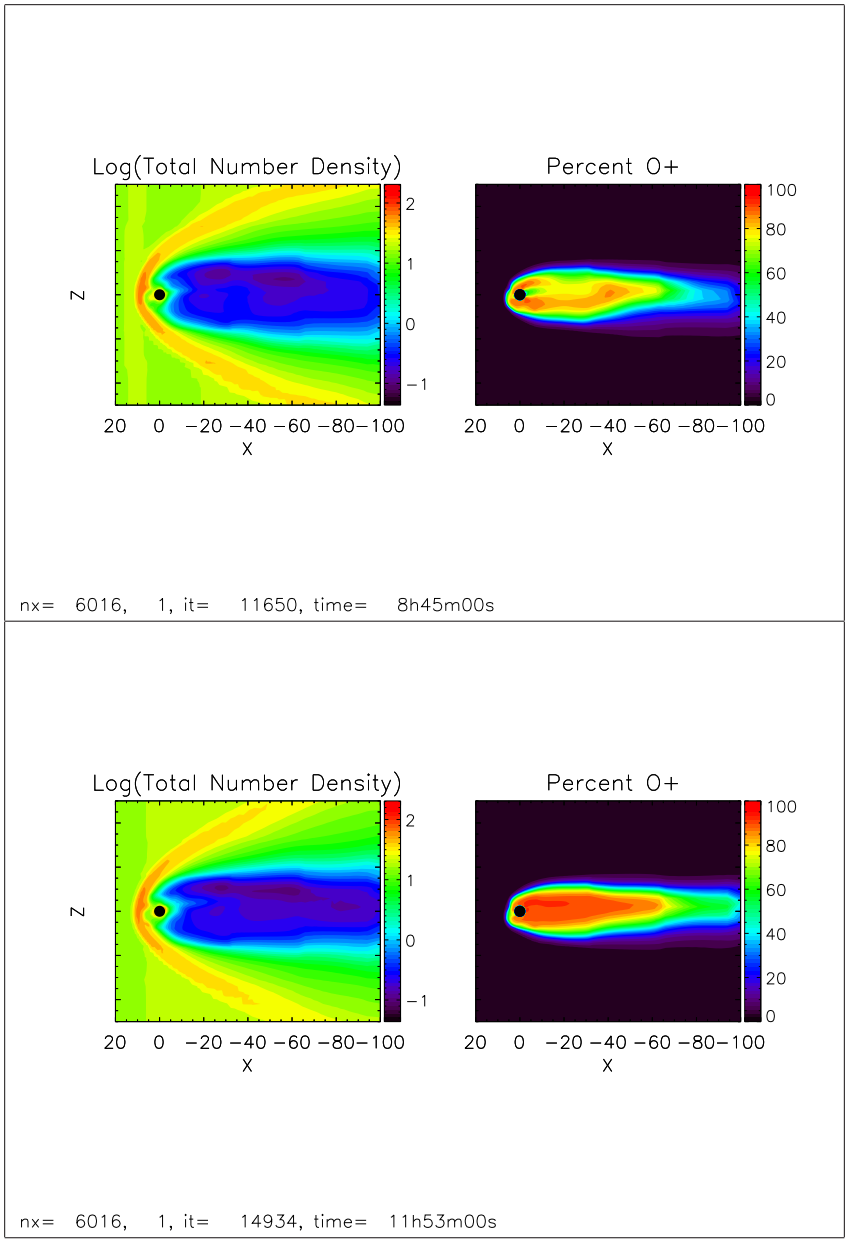

Figure 3.8: Log of number density and the percent of oxygen ions in the magnetosphere. The y=0 plane is shown.

are compared, the error is reduced by as much as a factor of two when outflow is included.

There are several contributing factors, both physical and numerical, to the improved agreement between the GOES data and the simulation when outflow is included. When outflow is included the total density in the magnetosphere is increased. As a result there is an increased source population for the ring current. The ring current model, represented by the RCM, energizes the plasma and increases the pressure and temperature which is then fed back to the global magnetosphere. The result is an increased plasma beta which makes the plasma more responsive to the solar wind driver. The increased density also decreases the Alfven speed which in turn reduces the amount of numerical diffusion. These effects, working in concert, improve the data model comparison.

Clearly, when the magnetosphere is modeled with ion outflow and ring current, the result is better than with only ring current. The next question is: Can we neglect any part of this system and still obtain accurate results? To answer the question, we repeated the simulation with only the GM and PW components and the ring current (IM component) switched off. The resulting comparisons are worse than when all three components are included. Therefore, it appears that to accurately model the magnetosphere the contributions from the ring current and the ion outflow must be included.

3.9 Conclusion and Discussion

This study outlines a new method for studying ionospheric outflow and its effect on the magnetosphere. We developed the PWOM, a new model for ion outflow, and incorporated it into the SWMF. The coupled model allows us to examine outflow as

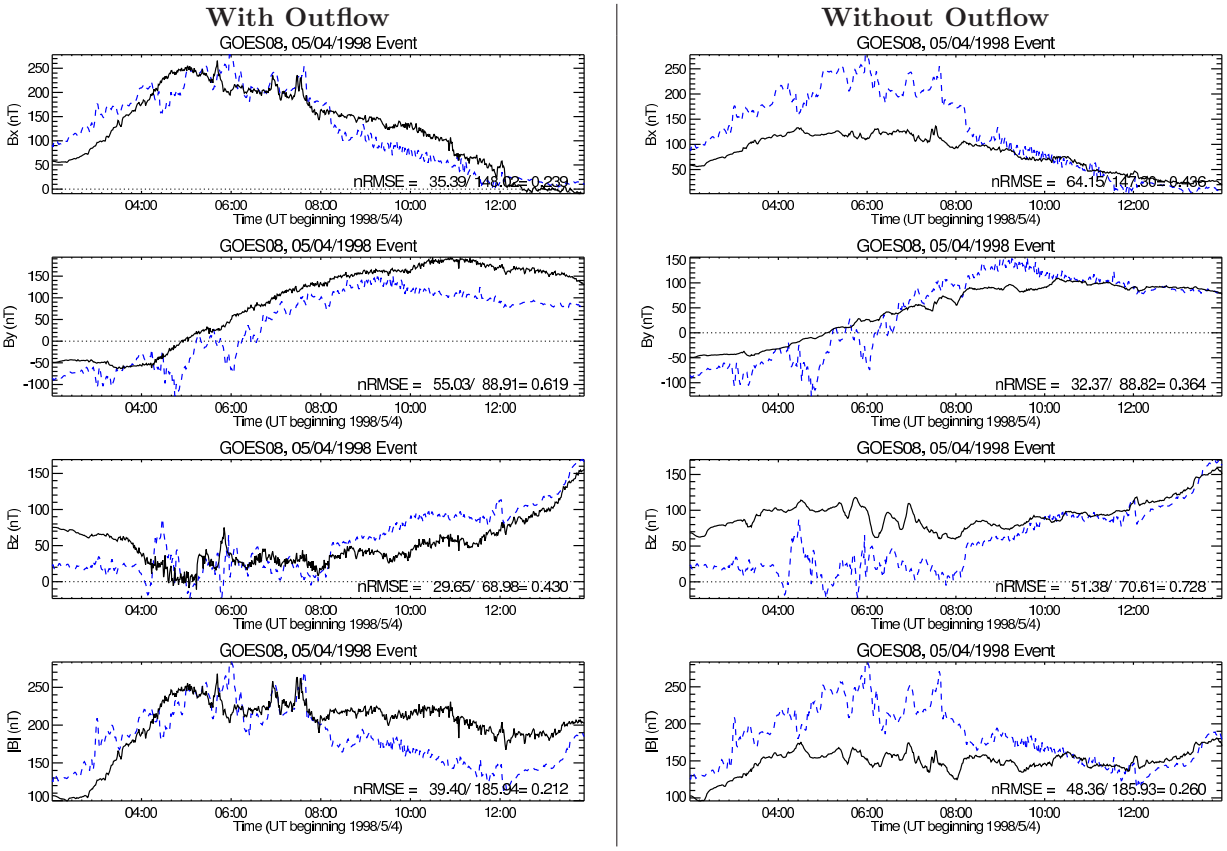

Figure 3.9: Data model comparisons of magnetic field from Goes 08 with the MHD magnetic field calculated by BATS-R-US. The plot on the left shows the comparison when the outflow from the PW component is included, and the plot on the right shows the comparison when outflow is not included.

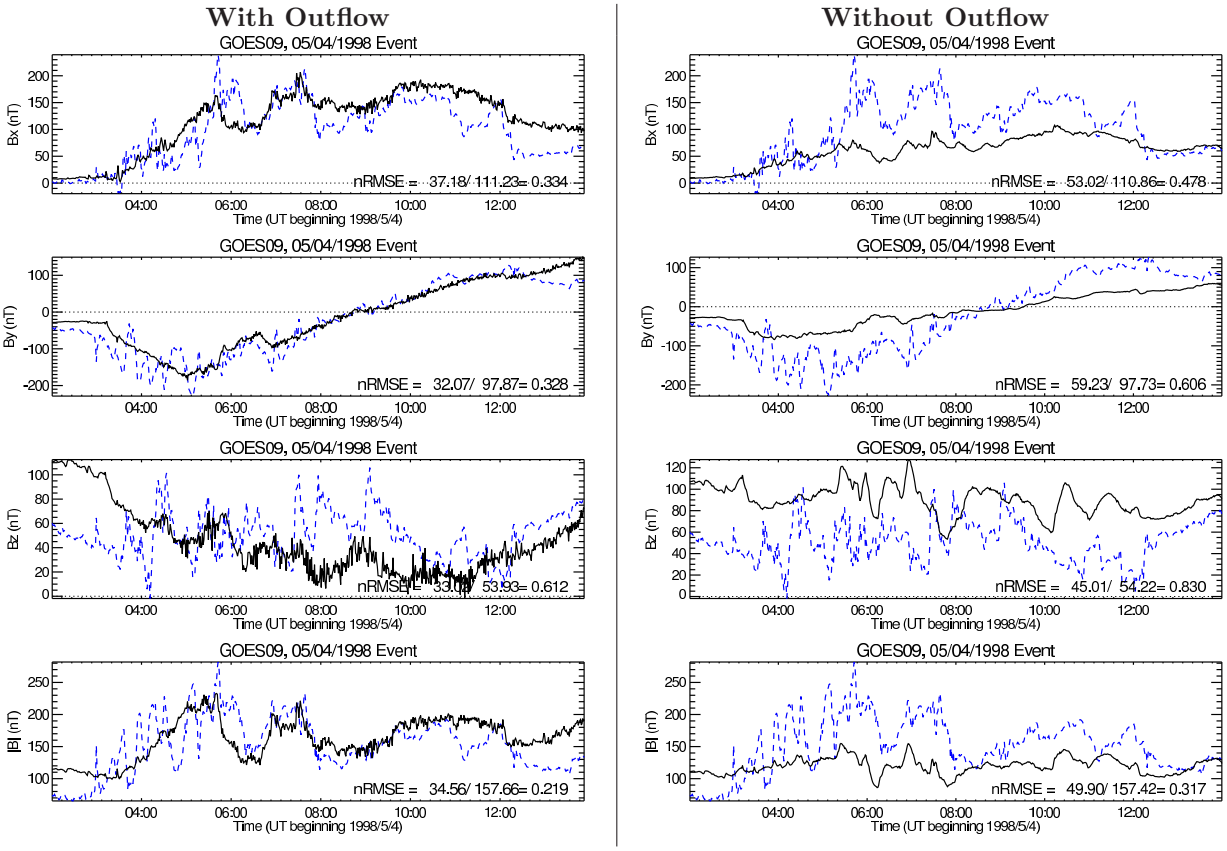

Figure 3.10: Data model comparisons of magnetic field from Goes 09 with the MHD magnetic field calculated by BATS-R-US. The plot on the left shows the comparison when the outflow from the PW component is included, and the plot on the right shows the comparison when outflow is not included.

part of the space environment system. The simulations carried out in this chapter demonstrate the importance of including ion outflow in magnetospheric simulations.

The simulation of the 4 May 1998 storm clearly illustrates the necessity of including the ionospheric contribution to the magnetosphere. When comparing GOES data with simulations with and without ion outflow, the RMS error is significantly reduced when including outflow. The explanation for the improvement, provided in the previous section, relies on the energization of plasma of ionospheric origin through interaction with the ring current and the modification of the Alfven speed in the magnetosphere. As an experiment, the simulation was repeated with the IM component turned off. The comparison with data was much worse than when the ring current is not included, even with the outflow included. It is therefore clear that both outflow and ring current are need to accurately model the magnetosphere during a storm, and if any cog in that system is neglected the final comparison with data is weak.

Another striking feature of the simulation is the relatively high concentration of O^+ in the magnetosphere. Work by Nosé et al. (2005) shows that the energy density ratio between oxygen and hydrogen ions can get quite large during storms. Kistler et al. (2005) find that the contribution of O^+ to the total number density and pressure during substorms increases, creating a O^+:H^+ ratio as high as 10:1. While such large fractions exist, it is not clear that the large percentage of O^+ that persists throughout our simulation is reasonable. Future studies should include direct comparisons to composition data, including satellites such as Polar and Cluster.

The work presented in this chapter is just a first step. More storm simulations are needed to strengthen the conclusion that the inclusion of ion outflow is vital to accurately modeling geomagnetic storms. Additional improvements to the model will

also expand the type of studies that we can conduct. For instance the use of a multi-fluid MHD model for the magnetosphere will allow us to study how ionospheric plasma in the magnetosphere changes the magnetic reconnection and large scale dynamics.

CHAPTER IV

Modeling Ionospheric Outflows at Saturn

4.1 Chapter Abstract

The Saturnian, or Kronian, system's configuration and dynamics are to a large extent controlled by the planet's rapid rotation and the plasma in the magnetosphere. Therefore, characterizing the relative importance of the various plasma sources is crucial to understanding Saturn's magnetosphere. Most research in this area focuses on the addition of mass from the icy satellites, the rings, and Titan, while comparatively little attention has been paid to the ionospheric source. We investigate the ionospheric source at high latitude using multi-fluid numerical simulations of Saturn's polar wind, and find that the magnitude of the particle source rate out of the polar cap is between 2.1×10^{26} and 7.5×10^{27} s^{-1}. Our multi-fluid simulations are carried out using the Polar Wind Outflow Model (PWOM). This new model is capable of calculating the polar wind at Earth and Saturn by solving the gyrotropic transport equations. The polar wind at Saturn is modeled from below the peak ionospheric density to an altitude of one Saturn radius, yielding fluxes for H_3^+, H^+, and electrons. Because the neutral temperature is ill constrained, we calculate source rates for various Saturnian atmospheric profiles corresponding to neutral temperatures of 420, 600, 800, 1000, 1500 K. We compare the results with those calculated from other

models and measurements where appropriate.

4.2 Introduction

The Saturnian system has been explored and understood using a variety of methods including Earth based observation, in-situ measurements, and numerical simulations. Cassini's arrival at Saturn in 2004 has dramatically increased the amount of new data about Saturn's magnetosphere. By using numerical simulations, we can improve our understanding of these new measurements. In particular, here we focus on the ionosphere's relative importance as a sources of magnetospheric plasma.

In order to understand the importance of Saturn's various plasma sources, we draw an analogy to the environment at Earth. In chapter III we demonstrated that the Earth's ionosphere is an important plasma source for the magnetosphere. Additionally, Sharp et al. (1985) examine ISEE 1 and SCATHA mass spectrometer data and determine that the ionosphere is an important or dominant source of plasma for the inner magnetosphere. Furthermore, the significance of an ionospheric source led to speculation on the existence of a geopause (Moore and Delcourt (1995)). A recent paper by Huddleston et al. (2005) examines data from the Dynamics Explorer, and Polar spacecrafts, and argues that the ionosphere is a sufficient source for magnetospheric plasma. However, the ionosphere is not the only controller of magnetospheric plasma. Solar wind parameters are found to be highly correlated to plasma sheet parameters, and the occurrence of the super dense plasma sheet is found to be related to increased density in the solar wind (Borovsky et al. (1997), Borovsky et al. (1998)). Winglee (2000) uses multi-fluid simulations that include both the ionospheric and solar wind source, and finds that the relative importance is highly variable. These studies indicate that the dominant source is highly dependent

on geophysical conditions. However, the ionosphere is clearly an important, source of the magnetospheric plasma at the Earth. Because the ionosphere plays such an important role at Earth, there is reason to believe it may be a factor at Saturn.

Most previous studies of Saturn's magnetosphere have focused on non-ionospheric sources. Richardson and Jurac (2004) use a self-consistent model of plasma and neutrals to estimate the source rate of water products into the magnetosphere. Their model, described fully by Jurac and Richardson (2005), assumes that 95 percent of the neutral source is water and 5 percent is hydrogen. The model solves a diffusion equation for the transport of H^+, H_2^+, O^+, OH^+, H_2O^+, and O^{++}, and the neutral distribution is determined using a Monte Carlo method. They constrain their model with Voyager and Hubble Space Telescope data, and estimate a source of about 10^{28} H_2O/s coming from the area around Enceladus. Gombosi and Hansen (2005) show that this source can be very significant in determining magnetospheric behavior. By applying a plasma source of 10^{28} ions/s, which assumes that all of the neutral particles produced in the inner magnetosphere are ionized, to a global 3D magnetohydrodynamic simulation, they demonstrate that quasi periodic behavior of the magnetosphere can result.

A mass source originating from Enceladus has recently been measured by numerous instruments on the Cassini spacecraft. The Cassini Magnetometer detected the interaction of Saturn's plasma environment with an atmospheric plume emanating from Enceladus' south pole during the first three flybys of the Saturnian moon (Dougherty et al. (2006)). Stunning images of the plume, and the 'tiger stripes' where the plume originates, were captured by the Imaging Science Subsystem (ISS) (Porco et al. (2006)), and the Composite Infrared Spectrometer (CIRS) detected thermal emission from the 'tiger stripes' (Spencer et al. (2006)). Of particular in-

terest is the interpretation of data taken by the Ion and Neutral Mass Spectrometer (INMS) (Waite et al. (2006)). Waite et al. (2006) use a Monte Carlo simulation with a weak gravitational field and two particle sources; one uniform global source, and one centered on the south pole. By tuning these sources they get reasonable agreement with Cassini INMS data, and net source between 1.0×10^{26} to 3.0×10^{27} molecules s^{-1}. INMS data estimates that water accounts for 90.70 to 91.50 percent of the composition. Cassini's UltraViolet Imaging Spectrograph (UVIS) observed stellar occultation of Enceladus, providing valuable information on the nature of the plume (Hansen et al. (2006)). Analyzing this data, Hansen et al. (2006) infer a column density of 1.5×10^{16} cm^{-2}. Assuming that the density corresponds to a vapor equilibrium, and the gas velocity is at least the thermal velocity, they arrive at a source rate of 5×10^{27} molecules s^{-1}. These recent measurements establish Enceladus as a significant mass source to Saturn's magnetosphere.

The moon Titan is another mass source for Saturn's magnetosphere. Shematovich et al. (2003) and Michael et al. (2005) use one and three dimensional Monte Carlo simulations to quantify the source of neutral nitrogen resulting from photon and ion bombardment of the upper atmosphere. Smith et al. (2004) combine the results of these studies to estimate the net source rate of nitrogen atoms and molecules from Titan to be about 3.55×10^{25} s^{-1}, far less than the Enceladus source determined above. They use this as input to 3D Monte Carlo simulations to determine the morphology of the Titan torus. Smith et al. (2004) also mention that the neutral density in the Titan torus is larger than the Voyager-based ion density.

Recent observations of the plasma composition of Saturn's magnetosphere indicate that N^+ may not be as significant as previously thought. Young et al. (2005) present CAPS/IMS data from Cassini's initial orbit and note that N^+ was not detected in

the region of Titan's orbit either on the inbound or outbound pass. They do note, however, that the spacecraft was significantly distant from Titan's orbital plane; so the lack of nitrogen ions may not be unreasonable. Smith et al. (2005) also study CAPS/IMS data, and determine that that N^+ exists in Saturn's inner magnetosphere. The detected nitrogen ions are found to be close to local corotational energies and, and therefore are unlikely to be due to escape from Titan, but are probably created locally. More work needs to be done to understand the source, and significance, of the nitrogen ions in Saturn's magnetosphere. However, current evidence seems to indicate that the Titan source is one to two orders of magnitude less than the icy satellite and Enceladus source.

While the icy satellite and Enceladus sources of plasma are quite significant in the inner and outer magnetosphere, the ionosphere may play a role in the outer magnetosphere through the polar wind. Many models have been developed for the Earth, and have yielded a wealth of information for understanding the polar wind. The chemistry and plasma constituents are different between the Earth and other magnetized planets, but the fundamental physical processes remain the same. Indeed, Nagy et al. (1986) show that the polar wind may be a significant source of plasma to the Jovian magnetosphere. Therefore, the polar wind at Saturn may behave similarly to the terrestrial polar wind.

Only one study of the polar wind at Saturn exists. Frey (1997) studies the polar wind at Saturn between 1,400 and 8,000 km above the 1 bar level. The study demonstrates the dependance of the polar wind on the neutral atmosphere, and water and methane content. Notably, the larger neutral temperature raise the density of CH_4 at the lower boundary and reduce the net plasma density. Furthermore, a flux of polar wind plasma between 10^7 and 10^8 $cm^{-2}s^{-1}$is estimated. Frey (1997) also

considers the time variable nature of the polar wind. Simulating a flux tube that crosses from the day side and convects to the night side, they start from a steady state solution, and turn off photo-ionization for a number of hours. Unfortunately, the altitude range is too small to observe a realistic sonic transition, making the plasma source difficult to characterize.

Our study attempts to quantify the source of ionospheric plasma to the Saturnian magnetosphere. To do this, we introduce the Saturn version of the Polar Wind Outflow Model (PWOM), a multi-fluid, first principles, model of Saturn's polar wind. The PWOM builds on previous work by extending the altitude range, the parameter range, improving the numerical scheme, and extending the physical validity of the model. Moreover, we consider an altitude range from 1,400 to 61,000 km above the 1 bar level, and a variety of possible neutral atmospheres. The neutral atmospheres, described in Section 4.5, correspond to a selection of neutral temperatures ranging from 420 K to 1,500 K. Examining several possible parameters yields a range for the polar wind source at Saturn.

4.3 Model Description

The Polar Wind Outflow Model (PWOM), solves the gyrotropic continuity, momentum and energy equations that describe the supersonic ion outflow along open magnetic field lines in the polar region. The PWOM can simulate the polar winds of Earth and Saturn. At Earth the behavior of three ion species, O^+, H^+, and He^+ are considered, while at Saturn only two species, H^+ and H_3^+, are considered. The model assumes a stationary neutral atmosphere. Ranging in altitude from 250 km to 8,000 km for the Earth version, or 1,400 to 61,000 km for the Saturn version, the PWOM has its lower boundary set in a reservoir at chemical and thermal equilibrium, while

the top boundary is at considerably lower pressure, thus creating a transonic outflow to a low pressure external medium. The considerable altitude range covers two different regimes; the collision and chemistry dominated low altitude, and the expansion dominated high altitude. Furthermore, the ambipolar electric field is calculated at every time step, and is a major contributor to ion outflow. Other physical effects that are included in the PWOM, are topside electron heating, photo-ionization, and the expanding cross-sectional area of the magnetic flux tube. The ability to include field aligned currents is present, but not used in the current study. Energetic particle precipitation is included in the Earth version of the PWOM, but has not yet been added to the Saturn version.

Modeling the polar wind at Saturn requires modifying the chemistry and collision routines as well as the neutral atmosphere. We use the chemistry model described in Table 4.1. Note that H^+ is primarily due to photo-chemistry through dissociative ionization of H_2, while H_3^+ is generated by the reaction between H_2 and H_2^+ and the three body reaction involving H^+ and H_2. Furthermore, the loss of H_2^+ occurs so rapidly that we do not keep track of it in the model. For the current version of the code, the photo-ionization rates are kept constant with altitude. Solar zenith angle and altitude dependent photo-ionization rates will be included in future versions of the model. The chemical kinetic model is solved explicitly at all altitudes.

We also include the loss of H^+ with vibrationally excited H_2, as seen in Table 4.1. McElroy (1973) first suggested that this reaction is exothermic for vibrational levels greater than or equal to 4. Work by Cravens (1987) and Majeed et al. (1991) demonstrate that vibrationally excited H_2 may be a significant loss mechanism for H^+ in the Jovian and Saturnian ionospheres. However, the PWOM does not track the H_2 ($\nu \geq 4$) density. Instead, we follow the example of Moses and Bass (2000)

Reaction			Reaction Rate	Reference
$H_2+h\nu$	$\rightarrow$	$H^+ + H + e^-$	$1.9\times10^{-11}s^{-1}$	Moses and Bass (2000)
	$\rightarrow$	$H_2^+ + e^-$	$9.9\times10^{-10}s^{-1}$	Moses and Bass (2000)
$H+h\nu$	$\rightarrow$	H^+	$1.0\times10^{-9}s^{-1}$	Moses and Bass (2000)
$H_2O+h\nu$	$\rightarrow$	$H^+ + OH + e^-$	$4.2\times10^{-10}s^{-1}$	Moses and Bass (2000)
$H^+ + H_2\,(\nu \geq 4)$	$\rightarrow$	$H_2^+ + H$	See Text	-
$H_2^+ + H_2$	$\rightarrow$	$H_3^+ + H$	$2.0\times10^{-9}cm^3s^{-1}$	Nagy (1987),Anichich (1994)
$H^+ + H_2 + M$	$\rightarrow$	$H_3^+ + M$	$3.2\times10^{-29}cm^6s^{-1}$	Capone et al. (1977)
$H^+ + CH_4$	$\rightarrow$	$CH_3^+ + H_2$	$3.69\times10^{-9}cm^3s^{-1}$	Kim and Fox (1994)
	$\rightarrow$	$CH_4^+ + H$	$0.81\times10^{-9}cm^3s^{-1}$	Kim and Fox (1994)
$H_3^+ + CH_4$	$\rightarrow$	$CH_5^+ + H_2$	$2.4\times10^{-9}cm^3s^{-1}$	Anichich (1994)
$H_3^+ + H_2O$	$\rightarrow$	$H_3O^+ + H_2$	$5.3\times10^{-9}cm^3s^{-1}$	Anichich (1994)
$H^+ + H_2O$	$\rightarrow$	$H_2O^+ + H$	$8.2\times10^{-9}cm^3s^{-1}$	Anichich (1994)
$H^+ + e^-$	$\rightarrow$	$H+h\nu$	$1.91\times10^{-10}T_e^{-0.7}cm^3s^{-1}$	Kim and Fox (1994)
$H_3^+ + e^-$	$\rightarrow$	$H_2 + H$	$7.62\times10^{-7}T_e^{-0.5}cm^3s^{-1}$	Kim and Fox (1994)[1]
	$\rightarrow$	$H + H + H$	$9.7\times10^{-7}T_e^{-0.5}cm^3s^{-1}$	Kim and Fox (1994)[1]

Table 4.1: Chemistry in the Saturn polar wind model. (1) The net dissociative recombination of H_3^+ was also measured by Jensen et al. (2001) to be approximately 1.7×10^{-6} $T^{-0.5}$ cm^3s^{-1}, which is in agreement with the values given by Kim and Fox (1994).

and use a effective reaction rate defined by

$$k_{effective} = 2 \times 10^{-9} \sum_{\nu=4}^{8} \exp \frac{-(E_\nu - E_0)}{kT_\nu} \tag{4.1}$$

Where the effective reaction rate uses the entire molecular hydrogen density, as opposed to the $H_2(\nu \geq 4)$ population, and the vibrational temperatures in equation 4.1 are taken from Majeed et al. (1991).

4.4 Numerical Schemes

This section describes the numerical schemes used in the PWOM to solve the gyrotropic transport equations. The discretization is first order in time and second order in space. We use operator splitting to solve the heat conduction separately from the rest of the equation. The heat conduction is discretized by the standard implicit Crank-Nicolson scheme.

The advection terms are solved with the spatially second-order Total Variation Diminishing (TVD) Lax-Friedrichs scheme with some minor modifications. The primi-

tive variables U (densities, velocities and pressures) are extrapolated to the cell faces from the adjacent cell centers.

We apply limited reconstruction (VanLeer (1979)) to obtain the left and right face values

$$U^L_{j+1/2} = U_j + \frac{1}{2}\bar{\Delta}U_j \tag{4.2}$$

$$U^R_{j+1/2} = U_{j+1} - \frac{1}{2}\bar{\Delta}U_j \tag{4.3}$$

where $j+1/2$ is the cell interface between the cells indexed by j and $j+1$, and $\bar{\Delta}U_j$ is the limited slope of the variable. We use a modified monotized central limiter. If the left and right slopes $\Delta U_{j-1/2} = U_j - U_{j-1}$ and $\Delta U_{j+1/2} = U_{j+1} - U_j$ have opposite signs, the limited slope is zero. Otherwise we take

$$\bar{\Delta}U_j = \mathrm{sgn}\Delta U_{j+1/2} \min\left(\beta|\Delta U_{j-1/2}|, \beta|\Delta U_{j+1/2}|, \frac{|U_{j+1} - U_{j-1}|}{2\Delta x_j}\right) \tag{4.4}$$

where sgn is the sign function, and $1 \leq \beta \leq 2$ is an adjustable parameter. We found that $\beta = 1.5$ produces robust and accurate results.

The fluxes are calculated from the average of the left and right face values and a second order dissipative Lax-Friedrichs flux is added to obtain the numerical flux function

$$F_{j+1/2} = \frac{F(U^L) + F(U^R)}{2} - \alpha\left(U^R_{j+1/2} - U^L_{j+1/2}\right) \tag{4.5}$$

where F is the physical flux function and we use

$$\alpha = 0.45\frac{\Delta x}{\Delta t} \tag{4.6}$$

The coefficient is reduced to 0.45 from the standard 0.5 because the cell area varies with altitude. Using the numerical flux function, the conservative update is

$$U^*_j = U^n_j - \Delta t\frac{A_{j+1/2}F_{j+1/2} - A_{j-1/2}F_{j-1/2}}{V_j} + \Delta t S_j \tag{4.7}$$

where $A_{j+1/2}$ is the cell face area, V_j is the cell volume, S_j contains all the explicitly treated source terms, and the superscript $*$ refers to the fact that some of the source terms are yet to be added.

The ion-neutral momentum transfer term in Equation 3.5 and the corresponding ion-neutral energy transfer term in the Equation 3.6 are evaluated implicitly so that a reasonable time step can be used. Since there are no spatial derivatives involved, the implicit equations can be solved easily. First the momentum of species i is updated as

$$(\rho u)_i^{n+1} = \frac{(\rho u)_i^*}{1 + \Delta t \sum_j \nu_{ij}} \tag{4.8}$$

where $(\rho u)^*$ already contains the contributions from advection and other source terms, and ν_{ij} is the collisional frequency between ion species i and neutral species j. Here we exploit the fact that the neutral velocity is zero, but the formula can be easily generalized for non-zero v_j. Using the fully updated velocity and the partially updated energy, the partially updated pressure is

$$p_i^* = (\gamma_i - 1)\left[e_i^* - \frac{1}{2}\rho_i^{n+1}\left(u_i^{n+1}\right)^2\right] \tag{4.9}$$

where e is the energy density obtaind from the conservative update. Then the pressure is updated implicitly as

$$p_i^{n+1} = \frac{p_i^* + (k/m_i)\rho_i^n \Delta t \sum_j \mu_{ij}\nu_{ij} T_j^n}{1 + \Delta t \sum_j \mu_{ij}\nu_{ij}} \tag{4.10}$$

where $\mu_{ij} = 2(m_i)/(m_i + m_j)$ is the effective mass ratio, and the sum is over neutral species indexed by j.

The numerical scheme described above is implemented on a grid with an expanding cross-sectional area described by Equation 3.7. The bottom of the grid is located at 1,400 km above the 1 bar level, and the top of the grid is located at about 1 Saturn

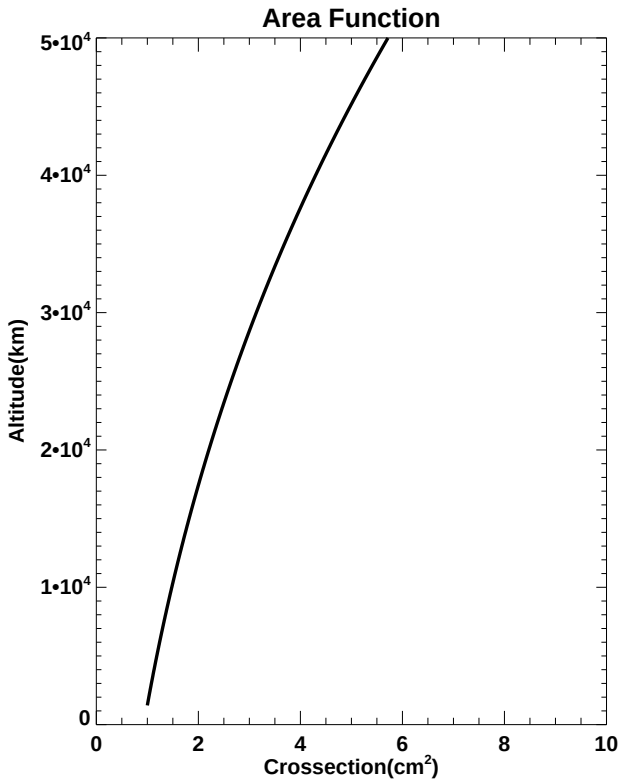

Figure 4.1: The cross-sectional area of a magnetic flux tube that has been normalized to have an area of 1 cm^2 at the bottom of the simulation.

Radius above the 1 bar level. Eight hundred cells are used with a grid spacing of 75 km. This resolution is shown by a grid convergence study to be sufficient. Grids with 200, 400, 800, and 1,500 cells are considered, and little difference is found between a grid using 1,500 cells and one using 800 cells. Therefore, by using the 800 cell grid we can complete the simulations in less time with confidence that the solution is accurate. For the 800 cell grid we can use a time step of 0.1 seconds.

4.5 The Neutral Background for Saturn

The PWOM requires the background neutral atmosphere as an input. For the Earth, the model uses the neutral background from MSIS 90. Unfortunately, a similar empirical model does not yet exist for Saturn. We therefore rely on analysis of the stellar occultation measurements of the Voyager 2 Saturn flyby, presented by

Smith et al. (1983), and other estimates to create our neutral background.

Most of the neutral constituents, as used in the PWOM, have their values defined at an altitude of 1,400 km, and are then extended to higher altitudes using a hydrostatic distribution. Close examination of Smith et al. (1983) demonstrates that the species independent hydrostatic assumption is reasonable above 1,400 km. The lower boundary densities of H_2 and H are set, according to analysis of the afore mentioned stellar occultation of Smith et al. (1983), to 6.3×10^9 cm^{-3} and 5.0×10^7 cm^{-3} respectively. The density of H_2O is set to 6.3×10^2 cm^{-3}, which represents a flux of 10^6 molecules cm^{-2} s^{-1} according to Majeed and McConnell (1991). This influx of water is comparable to Infrared Space Observatory (ISO) measurements presented by Feuchtgruber et al. (1997). Like H_2 and H, the density of CH_4 is also taken from Smith et al. (1983); but it is set to 1.6×10^8 cm^{-3} at 1,000 km because that is the highest altitude for which measurements of CH_4 are available.

There are challenges in approximating the neutral atmosphere as described. The Voyager 2 stellar occultation was taken at low latitude, but the polar wind is a process that takes place in the open field line region at high latitude. Joule heating in particular, can cause a strong increase in temperature in the polar region. Furthermore, the value of the exospheric neutral temperature, which affects the neutral scale height, is not well constrained. According to Smith et al. (1983), the neutral temperature is 420 K; Festou and Atreya (1982) estimate the neutral temperature to be 800 K. Preliminary work by Shemansky et al. (2005), using Cassini data, estimates the neutral temperature at 345 K. The neutral temperature can also be estimated from the plasma temperature. At low altitudes, the neutral temperature and the plasma temperature should coincide. Nagy et al. (2005) use radio occultation measurements from Cassini to estimate a plasma temperature consistent with

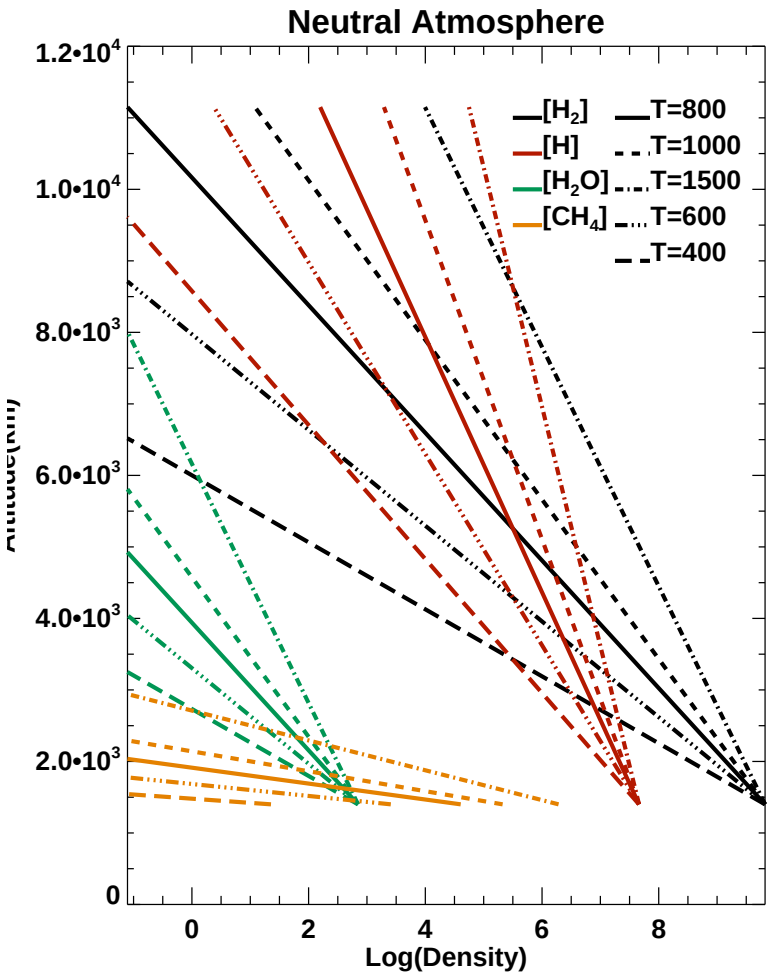

Figure 4.2: Plots of the various background neutral atmospheres considered.

1,000 K. Finally, Moore and Mendillo (2005) cite numerous studies to infer the range of topside plasma temperatures between approximately 260 and 1,700 K.

We consider a wide array of cases in an attempt to span the parameter space of possible neutral temperatures. Figure 4.5 illustrates the various cases considered in this study. The neutral temperatures range from 420 to 1,500 K, effectively covering the range of possible neutral temperatures. In the future, a more sophisticated neutral atmosphere may be considered, but for the purposes of this study, a simple isothermal and hydrostatic model is sufficient.

4.6 Results

Using the neutral atmosphere described in Section 4.5, we run the PWOM until a steady state is achieved for a number of scenarios. In order to disregard the effect of the upper boundary, the results are only presented below 50,000 km. Below 50,000 km, the result is reasonably insensitive to the position of the boundary. We verify this assertion by extending the simulation domain up to about 71,000 km, and comparing the results with the original simulation. We find that below an altitude of about 50,000 km the differences in the result are small. Density, electric field, and flux are presented for various neutral atmospheres corresponding to neutral temperatures 420, 600, 800, 1,000, and 1,500 K.

Figure 4.3 shows the ion densities for the various neutral temperatures. Changing the neutral temperature affects the neutral background, which in turn affects the ion density. Note that for lower neutral temperatures H^+ is the dominant ion, while for higher neutral temperatures H_3^+ is the dominant ion. Which ion species dominates is very important for the polar wind process. To a first approximation, the ambipolar electric field applies an upward force equal to about half the weight of the major ion. This is seen by keeping only the electron pressure gradient term in equation 3.4, and using a simple hydrostatic assumption. Therefore, increasing the neutral temperature leads not only to an increase in the mass of the major plasma constituent, but also leads to an increase in the ambipolar electric field. Figure 4.4 clearly demonstrates the calculated electric field's dependance on neutral temperature. While the peak electric field is larger for lower neutral temperatures, the electric field throughout most of the simulated range is smaller.

The electron density calculated by the model is of interest for several reasons. Be-

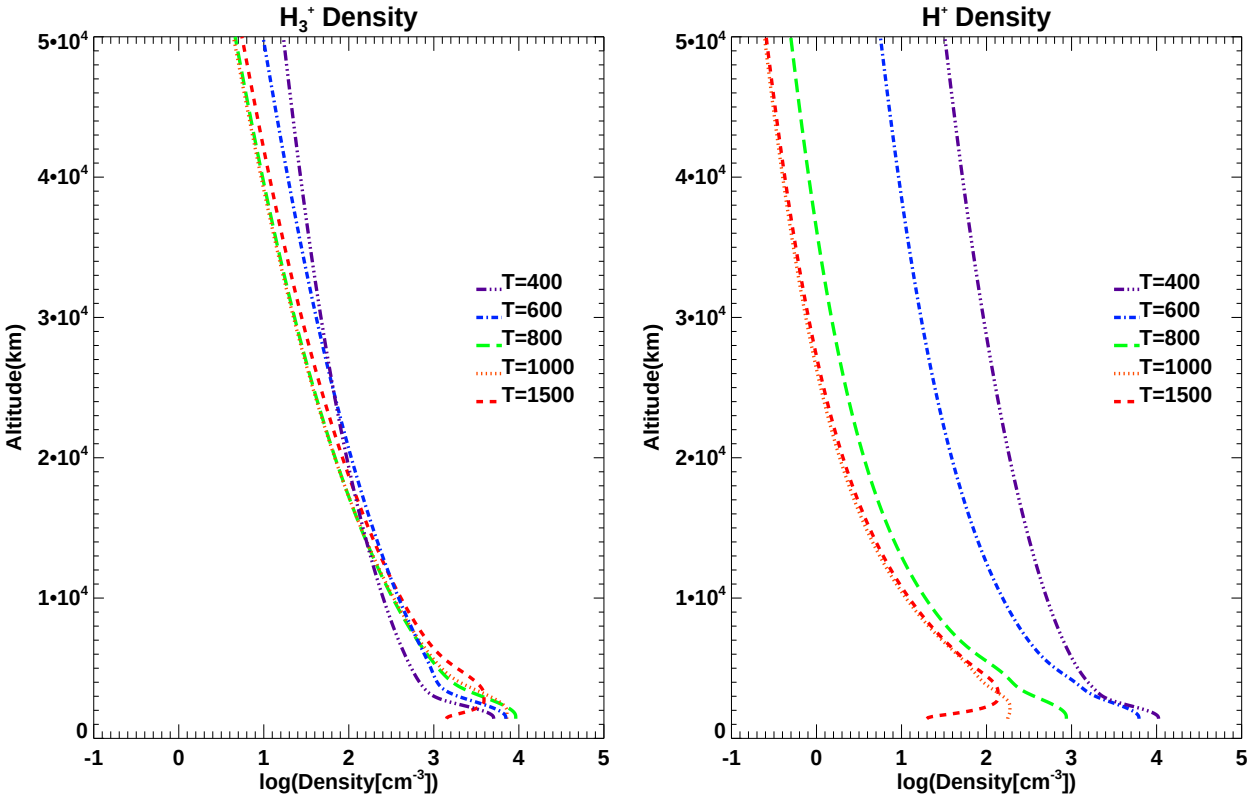

Figure 4.3: Plots of ion densities with H_3^+ on the left and H^+ on the right. Note that the neutral temperature affects the relative ion density.

cause of the quasi-neutrality condition imposed on the electrons, the electron density is representative of the total plasma density. It is also one of the few quantities for which high latitude data is available. Indeed, the Voyager 1 ingress radio occultation profile, presented by Atreya et al. (1984), provides data at 71 deg S latitude. Unfortunately, several challenges exist to doing a direct data-model comparison. First, without exact knowledge of the neutral atmosphere, it is difficult to precisely reproduce the data. Furthermore, it is not clear that 71 deg S is at sufficiently high latitude to place the measurement in the polar cap. Despite these difficulties, we compare our modeled cases to the available data. Figure 4.5 directly compares the measured and calculated electron densities below 10,000 km. The comparison shows

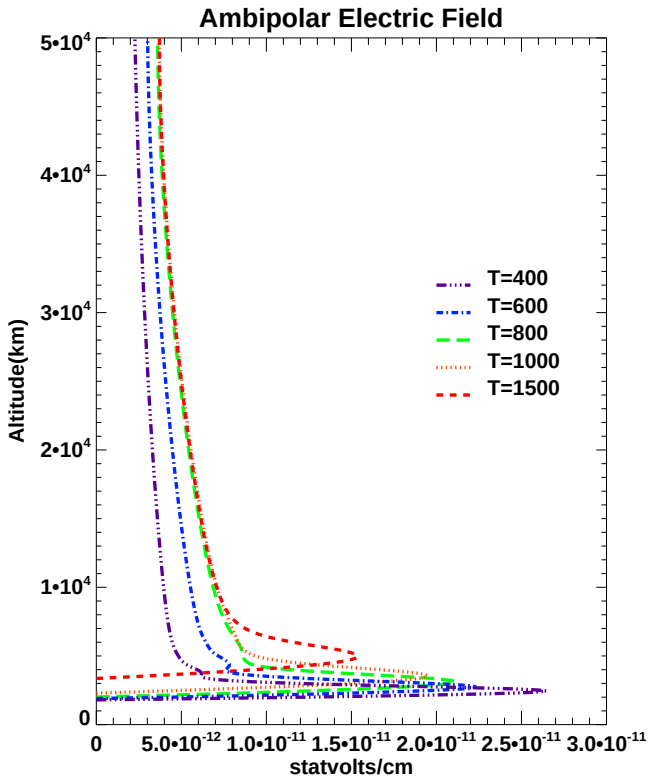

Figure 4.4: The plot demonstrates the ambipolar electric fields dependance on the neutral temperature. The cases with lower neutral temperatures have smaller electric field strength in the expansion region.

agreement in overall features. Notably, the clear density peak followed by a sharp decrease is evident in both the data and the modeled cases. The change in slope of the density decrease is also evident in both the data and modeled cases; it is representative of the importance of the vertical transport of plasma. Many key differences are also seen in the comparison. For instance, some cases match the magnitude of the density peak, while others match the location, but none of the afore mentioned cases do both.

The location of the density peak represents the altitude at which vertical transport and chemistry balance. Increasing the chemical source lowers altitude of the peak, while increasing vertical advection raises the altitude. These parameters are not independent; the low temperature cases have increased vertical transport and in-

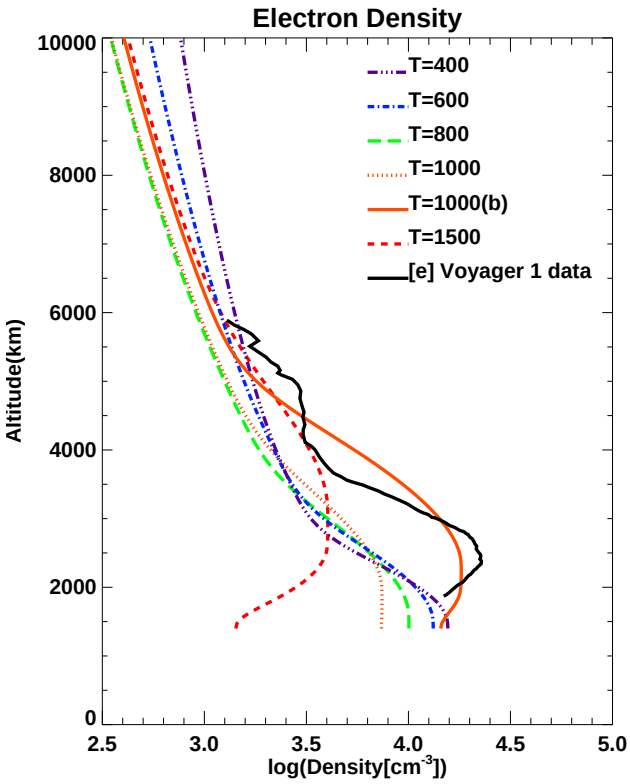

Figure 4.5: The plot demonstrates the electron densities dependence on the neutral temperature, and compares the result with Voyager 1 data taken at 71 deg S.

creased source terms (due to decreased loss from CH_4), while the higher temperature cases have decreased vertical transport and decreased source terms (due to increased loss from CH_4). It is expected that the peak density will always occur above the lower boundary of the model. In the high temperature cases this occurs, but for temperatures below 800 K we find that the density peaks at the boundary. There are several reasons that this could occur. One reason, is that the neutral densities at these latitudes are not well constrained, and changes will have a significant effect on the chemical source. Another reason has to do with a limitation of the model; the photo-ionization rate is not altitude dependent. As a result, the source at the lower boundary might be exaggerated, thereby lowering the peak. Future versions of the PWOM will include an altitude dependent photo-ionization rate, but for obtaining

a first estimate of the ionospheric source, the current model is adequate.

Because none of the previous cases showed strong agreement with the only available data set, we have tuned the neutral atmosphere to obtain improved agreement. Labeled case 1000 (b) in Figure 5, we consider an increase of a factor of 10 in H_2 and 1,000 in H_2O density with a neutral temperature of 1,000 K, and find a better match with the observed electron density. Additionally, we let H_2O decrease with a shorter scale height, reflecting that the neutral constituents are not well mixed at the altitudes considered. Increasing the H_2 density could be reflective of the importance of the energy input from Joule heating, which Cowley et al. (2004b) estimate to be more than 10 times the average solar input. Also, the density of water is not based on in-situ measurement, but rather on remote measurements. The uncertainty of the estimate is, therefore, greater. Moreover, Connerney and Waite (1984) note that the influx of H_2O is not spatially uniform. In particular, they note that at latitudes (-38 deg, $+44$ deg), which are magnetically connected to the inner B ring, the water influx may be approximately 50 times greater than the global average. The Voyager 1 data shown in Figure 4.5 was taken at 71 deg S which corresponds to L$\approx$ 8.5, or just past the edge of the E ring. Increasing the water density to this level has been studied by Majeed and McConnell (1991) and Moses and Bass (2000), and corresponds to an influx of about 10^8 molecules cm^{-3} s^{-1}. The flux is the largest considered in these studies, but not outside the realm of possibilities. This demonstrates the importance of accurate knowledge of the neutral densities. Future high latitude measurements by the Cassini spacecraft will assist in this endeavor.

The ion temperatures, given in Figure 4.6, illustrate the interaction between the two different physical regimes of the polar wind: One dominated by collisions with the background neutral atmosphere, and one that is expansion dominated. The rela-

tive size of the two regions is determined mainly by the neutral temperature. Larger neutral temperatures represent an increased neutral scale height, which gives rise to an expanded atmosphere. The result is to increase the region over which collisions are important. Hence, the region over which the ion temperature corresponds to the neutral temperature also increases. This is seen in Figure 4.6; where ion temperatures match the neutral temperatures is the collisional region, and where the ion and neutral temperatures begin to depart is the expansion dominated region. Furthermore, the collisions at low altitude lead to frictional heating that increases the ion temperature. Adiabatic cooling at high altitude, due to expansion, counteracts the low altitude frictional heating. A consequence of the low altitude heating and high altitude cooling is the formation of a temperature peak in Figure 4.6.

Another interesting feature of the ion temperature is the nonlinear dependence on the neutral temperature. The lowest neutral temperature case in Figure 4.6 corresponds to the lowest peak ion temperature, but the highest neutral temperature case does not correspond to the highest peak ion temperature. The heating depends on the two terms shown in Equation 3.6. The first term is a frictional heating term, and the second term tries to keep the ion temperature coincident with the neutral temperature. However, only the first term raises the peak, and it depends on the collision frequency and velocity difference. The coldest neutral temperature corresponds to the case with the lowest collision frequency, but the largest velocity difference. The hottest neutral temperature corresponds to the case with the largest collision frequency, but the smallest velocity difference. By contrast, the middle temperature cases have reasonably large collision frequencies and velocity differences. The result is that the largest temperature peaks occur for temperatures in the middle of the range considered.

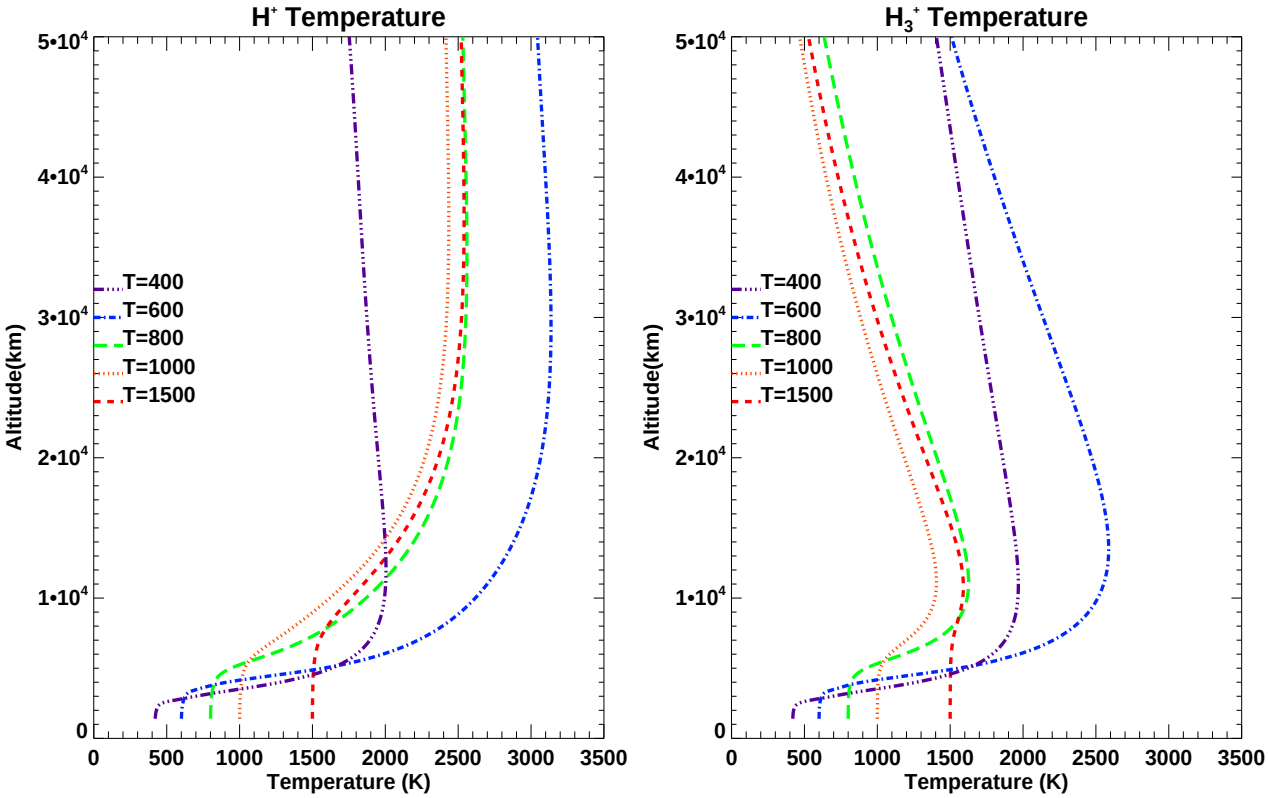

Figure 4.6: The plot on the left shows the ion temperature of H^+. The plot on the right shows the plasma temperature of H_3^+.

Particle flux is the key quantity to consider when gauging the polar wind's importance as a mass source. In particular, Equation 3.9 demonstrates that electron flux is equivalent to the net particle flux since field aligned currents are not considered in this case. Figure 4.7 presents the electron flux multiplied by the cross-sectional area of a flux tube. Since we are using a gyrotropic assumption, particles may only be lost through chemical reactions. Therefore, the number flux in a magnetic flux tube remains constant in the expansion dominated regime, but is not constant at low altitudes. Figure 4.7 illustrates that above about 5,000 km the number of particles flowing through the flux tube remains constant.

As demonstrated above, the neutral temperature greatly influences the polar wind.

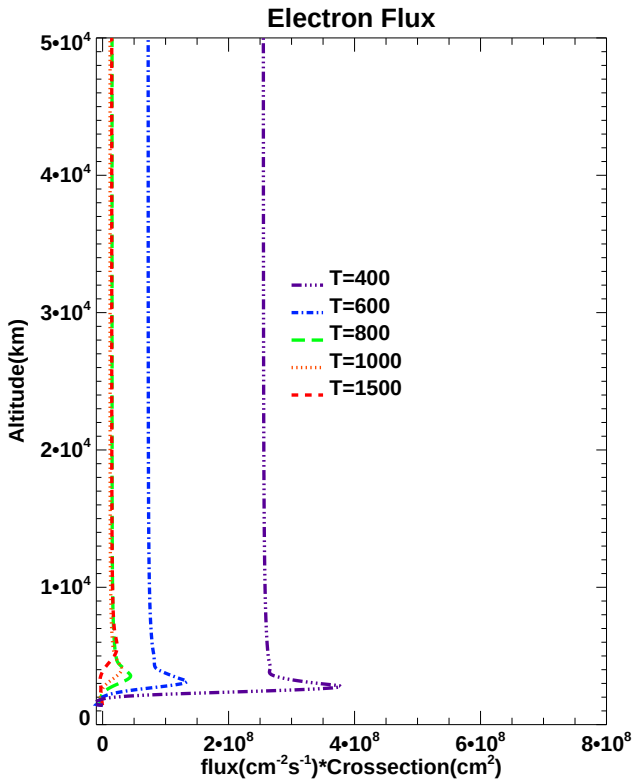

Figure 4.7: A plot of electron flux times the altitude dependent cross-sectional area normalized to 1 cm^2 at 1,400 km.

Figure 4.7 illustrates the importance of the neutral temperature to the outflow of plasma. Notably, lower neutral temperatures translate to greater outflow than higher neutral temperatures. There are two main reasons for this behavior. First, because the low temperature atmosphere is more compressed than a warmer atmosphere, the collisional region is smaller, reducing collisions that impede the flow at low altitudes. Second, a cooler neutral background allows less CH_4 at the bottom of the model; as a consequence, the chemical loss of ions is reduced, leading to increased plasma densities. Therefore, improved knowledge of the CH_4 density is needed to fully understand the plasma densities and outflows.

To translate flux into a net source rate for the magnetosphere, we must know the size of the polar cap. We obtain the polar cap area by using a Space Weather

Modeling Framework (Tóth et al. (2005)) simulation of Saturn's magnetosphere. In particular, we use simulations conducted by Hansen et al. (2005), and extract the total polar cap area for each of the seven bow shock crossing during the inbound leg of Cassini's Saturn orbit insertion, at times corresponding to 27/06/04: 09:45, 10:30, 18:00, 20:00, and 28/06/04: 00:15, 03:00, 05:45. This process yields a range of values from 2.9×10^{19}cm^2 to 4.4×10^{19}cm^2 at 10,000 km above the one bar level. Multiplying the polar cap area from the MHD simulation by flux of polar wind plasma yields the particle source rate. From the PWOM, we estimate that the polar wind number flux is between 7.3×10^6 and 1.7×10^8cm^{-2}s^{-1}, yielding a particle source rate between 2.1×10^{26} and 7.5×10^{27} s^{-1}.

4.7 Discussion of Results and Future Work

The results presented in Section 4.6 show that the magnitude of the polar wind source is between that of the icy satellites, calculated by Jurac and Richardson (2005), and of the Titan Torus, calculated by Smith et al. (2004). However, the polar wind source must be considered in context. Figure 4.8 shows a schematic of the spatial distribution of various mass sources. Note that the polar wind is mostly important in the open field line region, whereas the source from the icy satellites is more important for the inner magnetosphere.

Although the polar wind flows along open field lines, the plasma from the polar wind can make its way into lower latitudes. Consider, for example, an open field line about to reconnect in the tail. Such a field line has polar wind plasma flowing along it. After reconnection that same field line still has polar wind plasma flowing along it. Following the Dungey cycle (Dungey (1961)), that field line is now closed and begins to convect toward the dayside. Thus, polar wind plasma can enter the closed field

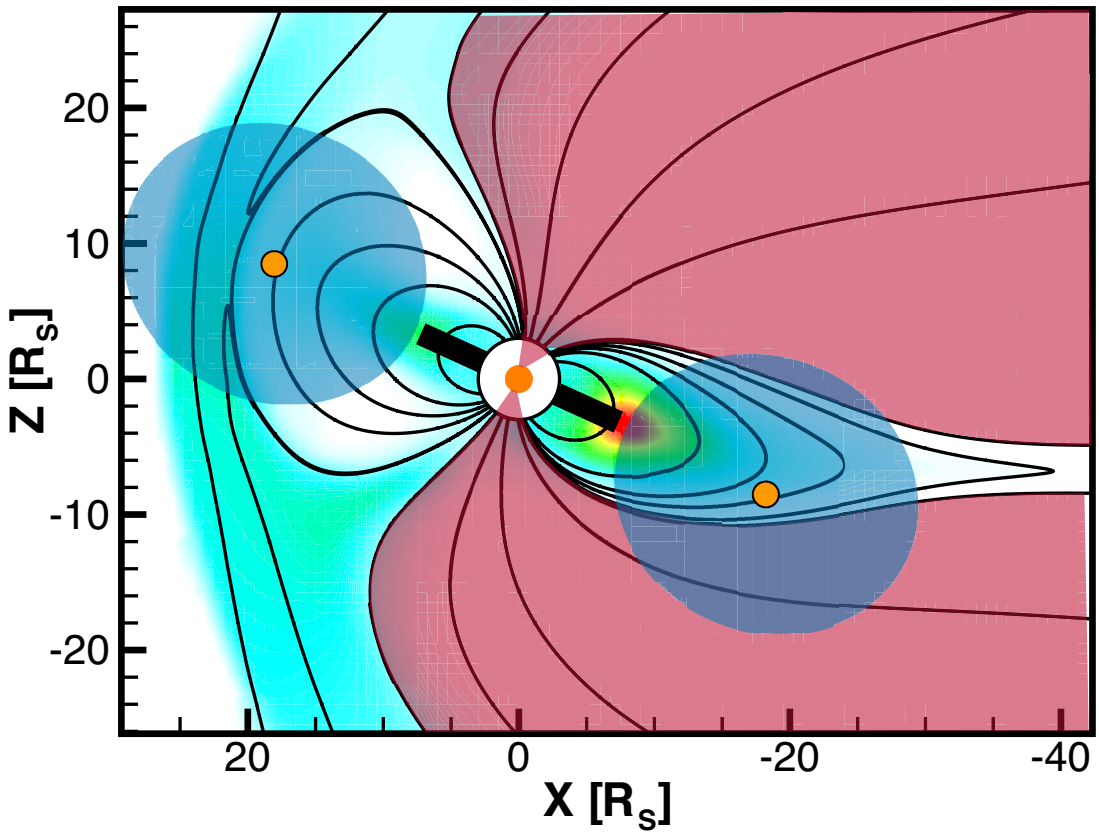

Figure 4.8: The schematic shows the location of three important mass sources to Saturn's magnetosphere. The E-ring and Enceladus are shown in black, and the Titan torus is shown as a blue oval around an orange dot at Titan's orbit. The region where the polar wind is important is shown in purple, and represents the open field line regions.

line region. We can estimate the efficiency of this process using a simple back-of-the-envelope calculation (Cowley (2006)). Jackman et al. (2004) find that the transpolar transit time can range from 1 to 8 days depending on solar wind conditions. Using an average polar wind velocity of 10 km s^{-1}, we find that the polar wind plasma can flow 14 to 115 Saturn Radii along the field line before reconnection can occur. The length of Saturn's tail is not well determined, but global MHD simulations of Saturn's magnetosphere (Hansen et al. (2005) figure 3) place the tail length at more than 65 Saturn Radii. Polar wind plasma that flows less than this distance before reconnection occurs is trapped in the magnetosphere. Therefore, at least 57 percent of all escaping polar wind plasma remains in the magnetosphere.

It is clear from the simulations that the neutral background density and temperature strongly influence the polar wind outflow. Increased temperature can cause the atmosphere to heat up and heave up; the breadth of the collisional region increases, thereby constricting the outflow of plasma. Furthermore, changes in the neutral density at the bottom of the model affects the relative ion densities. Changing the relative ion densities changes the ambipolar electric field, which in turn modifies the outflow through the momentum equation. However, since the low temperature cases have a reduced electric field but also an increased net ion outflow, the ambipolar electric field in the expansion region is not the main controller of the outflow rate. Furthermore, the decreased density of CH_4 in the low temperature cases are extremely important; reduced CH_4 is a major contributor to increased ion densities, and as a result, increased flux.

The fluxes calculated by the PWOM compare well with those calculated by Frey (1997), despite some significant differences. As mentioned earlier, Frey (1997) calculate a flux between 10^7 and 10^8 $cm^{-2}s^{-1}$ which is comparable to what the PWOM predicts. The differences between the models arise from an improved chemical scheme, neutral atmopshere, and altitude range. The PWOM uses a photo-ionization rate of 1.9×10^{-9} for the reaction $H_2 + h\nu \rightarrow H^+ + H + e$, which is 5 times less than the value used by Frey (1997). Since this reaction is a major source of H^+, the reduced rate will lead to smaller densities. Moreover, the Frey (1997) model does not include loss of H^+ with vibrationally excited molecular hydrogen. This is a major loss process, and also serves to reduce the density of H^+. Counteracting these effects is the significant reduction in the amount of water in the background neutral atmosphere. Our model uses a water flux that is comparable to Infrared Space Observatory (ISO) measurements as reported by Feuchtgruber et al. (1997). In contrast, Frey (1997) use a much

larger number inferred by Majeed and McConnell (1991). Since water is a major loss of H^+, reducing the amount of water bolsters the density of H^+. Because some of our differences reduce the H^+ density, and some raise the density, our results are in reasonable agreement with those of Frey (1997).

Direct comparison of our results with other Saturnian ionospheric models is difficult for several reasons. First, most models are low latitude models, and therefore do not include polar wind processes. Additionally, the altitude range considered by other models is very different, and diffusion is their main plasma transport process. Finally, low latitude models do not consider the range of neutral temperatures that may be available at high latitudes. Despite these differences, we can still make a qualitative comparison using the lowest temperature case considered by the PWOM at low altitude (near 1,400 km). Relative ion densities at low altitudes in the lowest temperature case are in good agreement with the studies of Moses and Bass (2000) and Moore et al. (2004). This region is well within the chemical equilibrium regime, and due to similar chemical models, good agreement is expected.

A lack of measurements of the background neutral atmosphere at high latitude restricts the ability of the PWOM to go beyond understanding fundamental processes and making zeroth order source estimates. The high latitude atmosphere may vary significantly from that at low latitude. Increased solar zenith angle, and Joule heating are two physical effects that may cause such differences. As shown above, the polar wind at Saturn is heavily reliant on the neutral background; the uncertainties in the neutral background resulting from the lack of measurements can strongly influence the results. Future measurements by the Cassini spacecraft should help address the issues resulting from the sparsity of data.

As alluded to in the introduction, several non-classical effects may impact Saturn's

polar wind. Centrifugal acceleration, frictional heating, and wave-particle interactions may enhance the flow and create transient features in the polar wind. These effects are outside the range of the PWOM, but we discuss their potential significance. We carry out a simple calculation to estimate the importance of centrifugal acceleration and frictional heating. Cowley et al. (2004a) estimate that the transpolar flow speed in the polar cap is approximately 200 m s^{-1}. Therefore, at the lower boundary of our model the centrifugal force is found to be 10^5 times less than the gravitational force, and is thus a small correction. By using Equation 3.6, assuming that the neutrals are stationary and have the same temperature as the ions, and that the number density is on the order of 10^3 cm^{-3}, we estimate that the energy input due to frictional heating is, at most, on the order of 10^{-13} Joules m^{-3}. This could be a very significant effect leading to transient outflows. The region were frictional heating is important is spatially and temporally constrained and will require tracking the flux tube motion. Future versions of the PWOM should include this potentially important effect. The importance of wave-particle interactions to Saturn's polar wind is much harder estimate, and therefore more study is needed before any meaningful statement can be made.

Further improvements to the model will allow us to expand upon the present study. In particular, including a solar zenith angle dependance on photo-ionization in the Saturn version of the PWOM will allow us to study the polar wind at various locations in the polar cap, and will allow improved density profiles. The inclusion of impact ionization will also be an improvement, and will raise the source estimates calculated here. A more sophisticated chemical model should also be used. These improvements will increase the accuracy and scope of the model.

CHAPTER V

Conclusion

The space environment makes up a complicated interconnected system comprised of regions with different spatial locations, characteristic energies and length scales. It is important to consider the interactions between these disparate regions in order to understand each regime, and to study the whole system. In this thesis we examined the role of radiation belts and polar wind outflow on the space environment system through the use of newly coupled models.

When simulating an active time period, the importance of the magnetospheric magnetic field and the polar cap potential on the radiation belt solution becomes apparent. Differences in the polar cap potential change the convection in the inner magnetosphere. Together with rapid changes in the magnetic field, it is possible to see rapid capture of radiation belt electrons. Changing the convection pattern or the magnetic field model significantly changes the condition for capture.

By combining similar simulations with radiation belt data we can study additional questions. In particular, why some geomagnetic storms lead to radiation belt enhancements while others do not, and what the mechanisms are for enhancement. These are questions that remain largely unresolved. Future work will use this newly coupled model to study these open questions.

Just as the radiation belt solution can be affected by the magnetosphere and ionosphere solutions, the result in the magnetosphere is affected by ionospheric outflow. The outflow during storm times, as modeled by the PWOM, can increase the density in the inner magnetosphere and potentially raise the plasma beta. At the same time the increased density can reduce the Alfven speed thereby reducing the numerical diffusion. The combination of increased plasma beta and reduced diffusion yield improved agreement between the model and the data.

The ionosphere can also be a significant contributor to the plasma population of the magnetosphere in planetary applications. Although smaller than the measured contribution from the moon Enceladus, the calculated ionospheric outflow at Saturn is significant. Just how much the ionospheric outflow affects the solution in Saturn's magnetosphere, however, is a subject for future studies.

In all these cases, be it how the ionosphere and magnetosphere impact the radiation belts, or how the flow of mass from the ionosphere to the magnetosphere changes the behavior in the magnetosphere, the importance of treating the space environment as a coupled system is evident. Moreover, leaving out the coupling between the various regions neglects important physics that must be included. To understand and explain what is happening in the ionosphere, magnetosphere, radiation belts, etc. the regions must be considered together.

Of course none of these questions could have been addressed without a significant amount of model development. To accomplish the first study an existing radiation belt model (the RBE model) was incorporated in the SWMF. This process involved coupling together two model over a three dimensional domain, and with vastly different grids. The second study also required model coupling, but of a much more complicated nature. Additionally, a new, parallel, model of ionospheric outflow (the

PWOM) needed to be developed. This new model solves the field-aligned gyrotropic transport equations for multiple moving field-lines, and determines the resulting fluxes of O^+, H^+, and He^+ into the magnetosphere. Finally, adding the PWOM to the SWMF necessitated the creation of a new component, and expansion of the SWMF.

These technical challenges were formidable, but new technology allows for more interesting scientific studies. As a result of the software development undertaken as part of this thesis, there are many possibilities for future study. For instance, an examination of magnetospheric plasma sources and the ramifications for dynamics can now be undertaken; Or a study of how ion outflow affects the radiation belt dynamics; Or the effect of ionospheric O^+ on reconnection in the tail. There are many possibilities for future study, and they are possible because of the new models and model couplings developed for this thesis.

5.1 Additional Lessons Learned

Several scientific results were obtained and new technologies were developed while working on this thesis (see above). In particular, the necessity of utilizing a systems approach to studying the space environment becomes apparent, and new technologies for doing so were developed. However, I learned a great deal beyond the scientific conclusions detailed above. How to tackle a problem scientifically, and how to develop the necessary effective and accurate software are both valuable lessons derived from my experience.

When attacking a scientific problem, the scientific method provides a clear approach to answering questions. You can test a given hypothesis with well devised experiments and adequate controls, but learning to create the well devised experi-

ment is extremely difficult to learn. In this thesis, the experiments take the form of numerical simulation, but, just like a traditional experiment, the simulations must be carefully constructed and carried out in a way that allows us to draw clear conclusions.

One of the main challenges I had to deal with in learning to setup a numerical experiment is verification that the model is actually solving the equations correctly. Solving this difficult problem is crucial when using a numerical model to address scientific questions. Unfortunately, we use simulations when analytic solutions either do not exist, or are impractical to obtain. Therefore a direct comparison with an exact solution is impossible. Hope is not lost, however, and we can make due with three substitutes: Limiting cases, grid convergence, and data model comparisons. I focus only on the PWOM since the other models discussed in this thesis were developed by others who have already carried out the verification processes described.

The first step to verifying that our model is to look at limiting cases of specific quantities. In the polar wind, it is well known that in the simplest approximation the ambipolar electric field is given by:

$$E_{\parallel} = -\frac{1}{en_e}\frac{\partial p_e}{\partial z} = \frac{m_i g}{2e}$$

where p_e is the electron pressure, z is the altitude coordinate, n_e is the electron number density, e is the electron charge, m_i is the mass of the major ion species, and g is the gravitational acceleration. At Earth, where the major ion is Oxygen, we can expect an electric field of about 8.6×10^{-6}V/m; at Saturn, where the major ion is H_3, the electric field is about 1.5×10^{-7}V/m. The average values in the model are found to be close to these approximate values, indicating that the model is working correctly. Other quantities can be compared likewise. At low altitudes, the model should return densities that are close to chemical equilibrium; the calculation is too

complex to be included in its entirety, but the results agree quite well with with the model.

Grid convergence is another step required to demonstrate that the model is accurately modeling the equations. When the equations are discretized, it is inevitable to have terms that depend on the grid spacing. As the grid is refined, however, the dependence on the spacing should diminish; otherwise the result would depend on resolution which is unphysical. Chapter IV carries out exactly this trial, and the PWOM exhibits excellent grid convergence.

Data model comparisons are more correctly used for validation of the codes usefulness rather than verification that the code is solving the equations correctly, however good data model comparisons are usually a good indication. In the preceding chapters, comparisons with specific satellites demonstrated the satisfactory performance of the model. Moreover, general agreement between this model and Akebono satellite data was demonstrated by Abe et al. (2004).

Having a working model that accurately solves the equations given to it is essential to being able to answer scientific questions using numerical techniques. Otherwise the model would be no better than using a faulty experimental setup in a laboratory experiment. Since our models agree well in limiting cases, exhibit grid convergence and agreement with data, they are clearly appropriate to use in answer the questions posed in the thesis. Learning how to develop such a model and how to conduct verification was a very valuable lesson.

In conducting model development for this thesis I learned another useful lesson: good coding practice and frequent, automated, testing. This may sound like a minor concern, but code written in a haphazard way without standards is more likely to contain insidious bugs that are hard to track down. Using good programming

practices that follow a naming standard for variables and a consistent design philosophy is essential for writing readable code that has a minimum of bugs. Likewise, frequent functionality testing uncovers bugs as soon as they are introduced, allowing for (relatively) painless correction as compared to trying to find an introduced bug months or years later. I followed these techniques when developing the PWOM and the other couplings described in this thesis, and found them to be invaluable.

Learning to answer scientific questions, develop and verify physical models, and how to use good coding practices are all important lessons that I learned during the course of this research. Careful verification and good coding practices may appear to be insignificant parts of using a model to deal with physical problems, but with out them the level of confidence in the model's accuracy and ability plummets. Therefore, these seemingly minor concerns are actually invaluable lessons for conducting good scientific studies.

BIBLIOGRAPHY

BIBLIOGRAPHY

Abe, T., Yau, A. W., Watanabe, S., Yamada, M., Sagawa, E., Sep. 2004. Long-term variation of the polar wind velocity and its implication for the ion acceleration process: Akebono/suprathermal ion mass spectrometer observations. J. Geophys. Res. 109, 9305.

Anichich, V. G., 1994. Evaluated bimolecular ion-molecule gas phase kinetics of positive ions for use in modeling the chemistry of planetary atmospheres, cometary comae, and interstellar clouds. J. Phys. Chem. Ref. Data 22, 1469.

Atreya, S. K., Donahue, T. M., Nagy, A. F., Waite, J. H., McConnell, J. C., 1984. Theory, measurements, and models of the upper atmosphere and ionosphere of Saturn. Saturn, pp. 239–277.

Axford, W. I., 1968. The polar wind and the terrestrial helium budget. J. Geophys. Res. 73, 68,55.

Baker, D., 2000. The occurrence of operational anomalies in spacecraft and their relationship to space weather. Plasma Science, IEEE Transactions on 28 (6), 2007–2016.

Baker, D. N., Mason, G. M., Figueroa, O., Colon, G., Watzin, J. G., Aleman, R. M., May 1993. An overview of the Solar, Anomalous, and Magnetospheric Particle Explorer (SAMPEX) mission. IEEE Transactions on Geoscience and Remote Sensing 31, 531–541.

Banks, P. M., Holzer, T. E., 1968. The polar wind. J. Geophys. Res. 73, 6846.

Barakat, A. R., Barghouthi, I. A., Oct. 1994. The effect of wave-particle interactions on the polar winds O(+). Geophys. Res. Lett. 21, 2279–2282.

Barakat, A. R., Barghouthi, I. A., Schunk, R. W., 1995. Double-hump H^+ velocity distribution in the polar wind. Geophys. Res. Lett. 22, 1857–1860.

Bekerat, H. A., Schunk, R. W., Scherliess, L., Jul. 2007. Estimation of the high-latitude topside electron heat flux using DMSP plasma density measurements. Journal of Atmospheric and Solar-Terrestrial Physics 69, 1029–1048.

Bekerat, H. A., Schunk, R. W., Scherliess, L., Ridley, A., Nov 2005. Comparison of satellite ion drift velocities with amie deduced convection patterns. Journal of Atmospheric and Solar-Terrestrial Physics 67, 1463.

Beutier, T., Boscher, D., Aug. 1995. A three-dimensional analysis of the electron radiation belt by the Salammbô code. J. Geophys. Res. 100, 14853–14862.

Beutier, T., Boscher, D., France, M., Sep. 1995. SALAMMBO: A three-dimensional simulation of the proton radiation belt. J. Geophys. Res. 100, 17181–17188.

Boltzmann, L., 1872. Weitere studien über das wärmegleichgewicht unter gasmolekülen. Sitz. Math.-Naturwiss. Cl. Akad. Wiss. Wien 66, 275–370.

Borovsky, J. E., Thomsen, M., Elphic, R. C., 1998. The driving of the plasma sheet by the solar wind. J. Geophys. Res. 103, 17,617–17,639.

Borovsky, J. E., Thomsen, M. F., McComas, D. J., 1997. The superdense plasma sheet: Plasmaspheric origin, solar wind origin, or ionospheric origin? J. Geophys. Res. 102, 22,089–22,097.

Bourdarie, S., Boscher, D., Beutier, T., Sauvaud, J.-A., Blanc, M., Aug. 1997. Electron and proton radiation belt dynamic simulations during storm periods: A new asymmetric convection-diffusion model. J. Geophys. Res. 102, 17541–17552.

Cannata, R. W., Gombosi, T. I., Oct. 1989. Modeling the solar cycle dependence of quiet-time ion upwelling at high geomagnetic latitudes. Geophys. Res. Lett. 16 (10), 1141–1144.

Capone, L. A., Whitten, R. C., Prasad, S. S., Dubach, J., 1977. The ionospheres of saturn, uranus, and neptune. Ap. J. 215, 977.

Chen, Y., Friedel, R. H. W., Reeves, G. D., Nov. 2006. Phase space density distributions of energetic electrons in the outer radiation belt during two Geospace Environment Modeling Inner Magnetosphere/Storms selected storms. Journal of Geophysical Research (Space Physics) 111, 11.

Cladis, J. B., Sep. 1986. Parallel acceleration and transport of ions from polar ionosphere to plasma sheet. Geophys. Res. Lett. 13, 893–896.

Connerney, J. E. P., Waite, J. H., 1984. New model of saturn's ionosphere with an influx of water from the rings. Nature 312, 136.

Cowley, S., 2006. Private communication.

Cowley, S., Bunce, E., Prangé, R., Apr. 2004a. Saturn's polar ionospheric flows and their relation to the main auroral oval. Annales Geophysicae 22, 1379–1394.

Cowley, S. W. H., Bunce, E. J., O'Rourke, J. M., May 2004b. A simple quantitative model of plasma flows and currents in Saturn's polar ionosphere. J. Geophys. Res. 109, 5212.

Cravens, T. E., Oct. 1987. Vibrationally excited molecular hydrogen in the upper atmosphere of Jupiter. J. Geophys. Res. 92, 11083–11100.

Daglis, I. A., Thorne, R. M., Baumjohann, W., Orsini, S., Jan 1999. The terrestrial ring current: Origin, formation, and decay. Reviews of Geophysics 37, 407, (c) 1999: American Geophysical Union.

De Zeeuw, D. L., Gombosi, T. I., Groth, C. P. T., Powell, K. G., Stout, Q. F., 2000. An adaptive MHD method for global space weather simulations. IEEE Trans. Plasma Sci. 00, 00–00.

De Zeeuw, D. L., Sazykin, S., Wolf, R., Gombosi, T. I., 2004. Coupling of a global MHD code and an inner magnetosphere model: Initial results. J. Geophys. Res. 109.

Dougherty, M. K., Khurana, K. K., Neubauer, F. M., Russell, C. T., Saur, J., Leisner, J. S., Burton, M. E., 2006. Identification of a Dynamic Atmosphere at Enceladus with the Cassini Magnetometer. Science 311 (5766), 1406–1409.
URL `http://www.sciencemag.org/cgi/content/abstract/311/5766/1406`

Dungey, J. W., 1961. Interplanetary magnetic field and the auroral zones. Phys. Rev. Lett. 6, 47.

Elkington, S. R., Wiltberger, M., Chan, A. A., Baker, D. N., Oct. 2004. Physical models of the geospace radiation environment. Journal of Atmospheric and Terrestrial Physics 66, 1371–1387.

Festou, M. C., Atreya, S. K., 1982. Voyager ultraviolet stellar occultation measurements of the composition and thermal profiles of the saturnian upper atmosphere. Geophys. Res. Lett. 9, 1147.

Feuchtgruber, H., Lellouch, E., de Graauw, T., Bezard, B., Encrenaz, T., Griffin, M., 1997. External supply of oxygen to the atmospheres of giant planets. Nature 389, 159–162.

Fok, M.-C., Moore, T. E., Spjeldvik, W. N., Mar. 2001. Rapid enhancement of radiation belt electron fluxes due to substorm dipolarization of the geomagnetic field. J. Geophys. Res. 106, 3873–3882.

Fok, M. H., Horne, R. E., Meredith, N. P., Glauert, S. A., Jan. 2008. Radiation Belt Environment model: Application to space weather nowcasting. J. Geophys. Res. 113, A03S08.

Frey, M. A., 1997. The polar wind of saturn. Ph.D. thesis, The University of Michigan.

Fung, S. F., 1996. Recent Development in the NASA Trapped Radiation Models. In: Lemaire, J. F., Heynderickx, D., Baker, D. N. (Eds.), Radiation Belts: Models and Standards. p. 79.

Fuselier, S. A., Mende, S. B., Moore, T. E., Frey, H. U., Petrinec, S. M., Claflin, E. S., Collier, M. R., Oct. 2003. Cusp dynamics and ionospheric outflow. Space Science Reviews 109, 285–312.

Gagne, J., May 2005. Implementation of ionospheric outflow in the lfm global mhd magnetospheric simulation. Ph.D. thesis, Dartmouth College.

Ganguli, S. B., 1996. The polar wind. Rev. Geophys. 34, 311–348.

Ganguli, S. B., Mitchell, H. G., Palmadesso, P. J., Jun. 1987. Behavior of ionized plasma in the high latitude topside ionosphere: The polar wind. Planet. Space Sci. 35, 703–714.

Ganguli, S. B., Palmadesso, P. J., Aug. 1987. Plasma transport in the auroral return current region. J. Geophys. Res. 92, 8673–8690.

Gardner, L. C., Schunk, R. W., Oct. 2005. Global neutral polar wind model. J. Geophys. Res. 110, 10302.

Garrett, H., Whittlesey, A., 2000. Spacecraft charging, an update. Plasma Science, IEEE Transactions on 28 (6), 2017–2028.

Glocer, A., Toth, G., Fok, M., Gombosi, T., 2008. Integration of the radiation belt environment model into the space weather modeling framework. J. Atmos. Solar-Terr. Phys., Submitted.

Gombosi, T. I., 1988. Preshock region acceleration of implanted cometary H^+ and O^+. J. Geophys. Res. 93, 35.

Gombosi, T. I., 1998. Physics of the Space Environment. Cambridge University Press, Cambridge, UK.

Gombosi, T. I., Cravens, T. E., Nagy, A. F., Apr. 1985. A time-dependent theoretical model of the polar wind Preliminary results. Geophys. Res. Lett. 12, 167–170.

Gombosi, T. I., Hansen, K. C., Feb. 2005. Saturn's Variable Magnetosphere. Science 307, 1224–1226.

Gombosi, T. I., Kerr, L. K., Nagy, A. F., Cannata, R. W., 1991. Helium in the polar wind. Adv. Space Res. 12 (6), 183–186.

Gombosi, T. I., Killeen, T. L., 1987. Effects of thermospheric motions on the polar wind: A time-dependent numerical study. J. Geophys. Res. 92 (A5), 4725–4729.

Gombosi, T. I., Nagy, A., 1989. Time-dependent modeling of field aligned current-generated ion transients in the polar wind. J. Geophys. Res. 94, 359–369.

Gombosi, T. I., Powell, K. G., De Zeeuw, D. L., Clauer, C. R., Hansen, K. C., Manchester, W. B., Ridley, A. J., Roussev, I. I., Sokolov, I. V., Stout, Q. F., Toth, G., Mar/Apr 2004. Solution-adaptive magnetohydrodynamics for space plasmas: Sun-to-earth simulations. Computing in Science and Engineering 06 (2), 14–35.

Gombosi, T. I., Tóth, G., De Zeeuw, D. L., Hansen, K. C., Kabin, K., Powell, K. G., 2001. Semi-relativistic magnetohydrodynamics and physics-based convergence acceleration. J. Comput. Phys. 177, 176–205.

Gombosi, T. I., Tóth, G., de Zeeuw, D. L., Powell, K. G., Stout, Q. F., 2001. Adaptive mesh refinement MHD for global simulations. In: Büchner, J., Dum, C. T., Scholer, M. (Eds.), Space plasma simulation: proceedings of the Sixth International School/Symposium, ISSS-6, Garching, Germany, 3-7 September, 2001. Edited by J. Büchner, C.T. Dum, and M. Scholer. Berlin: Schaltungsdienst Lange o.H.G., 2001., p.88. p. 88.

Hansen, C. J., Esposito, L., Stewart, A. I. F., Colwell, J., Hendrix, A., Pryor, W., Shemansky, D., West, R., 2006. Enceladus' Water Vapor Plume. Science 311 (5766), 1422–1425.
URL http://www.sciencemag.org/cgi/content/abstract/311/5766/1422

Hansen, K. C., Ridley, A. J., Hospodarsky, G. B., Achilleos, N., Dougherty, M. K., Gombosi, T. I., Tóth, G., Jul. 2005. Global MHD simulations of Saturn's magnetosphere at the time of Cassini approach. Geophys. Res. Lett. 32, 20.

Heppner, J. P., Ness, N. F., Skillman, T. L., Scearce, C. S., 1962. Magnetic Field Measurements with the Explorer X Satellite. Journal of the Physical Society of Japan Supplement 17, B546+.

Hill, C., Luca, C. D., Suarez, M., Silva, A. D., 2004. The architecture of the earth system modeling framework. ieeexplore.ieee.org.

Hoffman, J. H., 1970. Studies of the composition of the ionosphere with a magnetic deflection mass spectrometer. Int. J. Mass Spectrom. Ion Phys. 4 (315).

Horwitz, J. L., Ho, C. W., Scarbro, H. D., Wilson, G. R., Moore, T. E., Aug. 1994. Centrifugal acceleration of the polar wind. J. Geophys. Res. 99, 15051–15064.

Huddleston, M. M., Chappell, C. R., Delcourt, D. C., Moore, T. E., Giles, B. L., Chandler, M. O., Dec. 2005. An examination of the process and magnitude of ionospheric plasma supply to the magnetosphere. J. Geophys. Res. 110, 12202.

Jackman, C. M., Achilleos, N., Bunce, E. J., Cowley, S. W. H., Dougherty, M. K., Jones, G. H., Milan, S. E., Smith, E. J., Nov. 2004. Interplanetary magnetic field at ˜9 AU during the declining phase of the solar cycle and its implications for Saturn's magnetospheric dynamics. Journal of Geophysical Research (Space Physics) 109, 11203.

Jensen, M. J., Pedersen, H. B., Safvan, C. P., Seiersen, K., Urbain, X., Andersen, L. H., 2001. Dissociative recombination and excitation of h[sub 3][sup +]. Physical Review A (Atomic, Molecular, and Optical Physics) 63 (5), 052701.
URL http://link.aps.org/abstract/PRA/v63/e052701

Jordanova, V. K., Miyoshi, Y., Jul. 2005. Relativistic model of ring current and radiation belt ions and electrons: Initial results. Geophys. Res. Lett. 32, 14104.

Jurac, S., Richardson, J. D., Sep. 2005. A self-consistent model of plasma and neutrals at Saturn: Neutral cloud morphology. J. Geophys. Res. 110, 9220.

Kanekal, S. G., Friedel, R. H. W., Reeves, G. D., Baker, D. N., Blake, J. B., Dec. 2005. Relativistic electron events in 2002: Studies of pitch angle isotropization. Journal of Geophysical Research (Space Physics) 110, 12224.

Kim, Y. H., Fox, J. L., Dec. 1994. The chemistry of hydrocarbon ions in the Jovian ionosphere. Icarus 112, 310–325.

Kistler, L. M., Mouikis, C., Möbius, E., Klecker, B., Sauvaud, J. A., Réme, H., Korth, A., Marcucci, M. F., Lundin, R., Parks, G. K., Balogh, A., Jun. 2005. Contribution of nonadiabatic ions to the cross-tail current in an O^+ dominated thin current sheet. Journal of Geophysical Research (Space Physics) 110, 6213–+.

Kivelson, M. G., Russell, C. T., Apr. 1995. Introduction to Space Physics. Introduction to Space Physics, Edited by Margaret G. Kivelson and Christopher T. Russell, pp. 586. ISBN 0521451043. Cambridge, UK: Cambridge University Press, April 1995.

Lennartsson, O. W., Apr. 1997. ISEE Ion Composition Data with Implications for Solar Wind Entry into Earth's Magnetotail. Space Science Reviews 80, 305–323.

Li, X., Temerin, M., Baker, D. N., Reeves, G. D., Larson, D., May 2001. Quantitative prediction of radiation belt electrons at geostationary orbit based on solar wind measurements. Geophys. Res. Lett. 28, 1887–1890.

Luhmann, J., Solomon, S., Linker, J., Lyon, J., Jan 2004. Coupled model simulation of a sun-to-earth space weather event. Journal of Atmospheric and Solar-Terrestrial Physics.

Lyon, J. G., Fedder, J. A., Mobarry, C. M., Oct. 2004. The Lyon-Fedder-Mobarry (LFM) global MHD magnetospheric simulation code. Journal of Atmospheric and Solar-Terrestrial Physics 66, 1333–1350.

Majeed, T., McConnell, J. C., 1991. The upper ionospheres of jupiter and saturn. Planet. Space Sci. 39, 1715.

Majeed, T., Yelle, R. V., McConnell, J. C., Nov. 1991. Vibrationally excited h2 in the outer planets thermosphere - fluorescence in the lyman and werner bands. Planet. Space Sci. 39, 1591–1606.

McElroy, M. B., 1973. The Ionospheres of the Major Planets (Article published in the Space Science Reviews special issue on 'Outer Solar System Exploration - An Overview', ed. by J. E. Long and D. G. Rea.). Space Science Reviews 14, 460.

Mead, G. D., Cahill, Jr., L. J., Jun. 1967. Explorer 12 Measurements of the Distortion of the Geomagnetic Field by the Solar Wind. J. Geophys. Res. 72, 2737–+.

Michael, M., Johnson, R. E., Leblanc, F., Liu, M., Luhmann, J. G., Shematovich, V. I., May 2005. Ejection of nitrogen from Titan's atmosphere by magnetospheric ions and pick-up ions. Icarus 175, 263–267.

Mitchell, H. G., Palmadesso, P. J., Mar. 1983. A dynamic model for the auroral field line plasma in the presence of field-aligned current. J. Geophys. Res. 88, 2131–2139.

Moore, L., Mendillo, M., May 2005. Ionospheric contribution to Saturn's inner plasmasphere. J. Geophys. Res. 110, 5310.

Moore, L. E., Mendillo, M., Müller-Wodarg, I. C. F., Murr, D. L., Dec. 2004. Modeling of global variations and ring shadowing in Saturn's ionosphere. Icarus 172, 503–520.

Moore, T. E., Delcourt, D. C., 1995. The geopause. Rev. Geophys. 33, 175–210.

Moore, T. E., Fok, M.-C., Delcourt, D. C., Slinker, S. P., Fedder, J. A., Mar. 2007. Global aspects of solar wind ionosphere interactions. Journal of Atmospheric and Solar-Terrestrial Physics 69, 265–278.

Moses, J. I., Bass, S. F., Mar. 2000. The effects of external material on the chemistry and structure of Saturn's ionosphere. J. Geophys. Res. 105, 7013–7052.

Nagy, A. F., 1987. Photochemistry of planetary ionospheres. Adv. Space Res. 7, (12)89.

Nagy, A. F., Barakat, A. R., Schunk, R. W., Jan. 1986. Is Jupiter's ionosphere a significant plasma source for its magnetosphere? J. Geophys. Res. 91, 351–354.

Nagy, A. F., Kliore, A. J., Marouf, E. A., French, R. G., Flasar, F. M., Rappaport, N. J., Anabtawi, A., Asmar, S. W., Johnston, D., Barbinis, E., Fleischman, D., Aug. 2005. Recent Results of Ionospheric Occultations of the Cassini Spacecraft by Saturn. AAS/Division for Planetary Sciences Meeting Abstracts 37.

National Research Council, 2003. The Sun to the Earth–And Beyond: A Decadal Research Strategy in Solar and Space Physics. National Academies Press, Washington, D.C.

Nosé, M., McEntire, R. W., Christon, S. P., May 2003. Change of the plasma sheet ion composition during magnetic storm development observed by the Geotail spacecraft. Journal of Geophysical Research (Space Physics) 108, 1201.

Nosé, M., Taguchi, S., Hosokawa, K., Christon, S. P., McEntire, R. W., Moore, T. E., Collier, M. R., Aug. 2005. Overwhelming O^+ contribution to the plasma sheet energy density during the October 2003 superstorm: Geotail/EPIC and IMAGE/LENA observations. Journal of Geophysical Research (Space Physics) 110, 9.

Pierrard, V., Lemaire, J., Jun. 1998. A collisional kinetic model of the polar wind. J. Geophys. Res. 103, 11701–11710.

Porco, C. C., Helfenstein, P., Thomas, P. C., Ingersoll, A. P., Wisdom, J., West, R., Neukum, G., Denk, T., Wagner, R., Roatsch, T., Kieffer, S., Turtle, E., McEwen, A., Johnson, T. V., Rathbun, J., Veverka, J., Wilson, D., Perry, J., Spitale, J., Brahic, A., Burns, J. A., DelGenio, A. D., Dones, L., Murray, C. D., Squyres, S., 2006. Cassini Observes the Active South Pole of Enceladus. Science 311 (5766), 1393–1401.
URL `http://www.sciencemag.org/cgi/content/abstract/311/5766/1393`

Powell, K. G., Roe, P. L., Linde, T. J., Gombosi, T. I., DeZeeuw, D. L., Sep. 1999. A solution-adaptive upwind scheme for ideal magnetohydrodynamics. J. Comput. Phys. 154 (2), 284–309.

Pulkkinen, T. I., Ganushkina, N. Y., Baker, D. N., Turner, N. E., Fennell, J. F., Roeder, J., Fritz, T. A., Grande, M., Kellett, B., Kettmann, G., Sep. 2001. Ring current ion composition during solar minimum and rising solar activity: Polar/CAMMICE/MICS results. J. Geophys. Res. 106, 19131–19148.

Reeves, G. D., McAdams, K. L., Friedel, R. H. W., O'Brien, T. P., May 2003. Acceleration and loss of relativistic electrons during geomagnetic storms. Geophys. Res. Lett. 30, 36–1.

Richardson, J. D., Jurac, S., Dec. 2004. A self-consistent model of plasma and neutrals at Saturn: The ion tori. Geophys. Res. Lett. 31, 24803.

Ridley, A., Gombosi, T., Dezeeuw, D., Feb. 2004. Ionospheric control of the magnetosphere: conductance. Annales Geophysicae 22, 567–584.

Ridley, A. J., De Zeeuw, D. L., Gombosi, T. I., Powell, K. G., Dec. 2001. Using steady state MHD results to predict the global state of the magnetosphere-ionosphere system. J. Geophys. Res. 106, 30067–30076.

Ridley, A. J., Deng, Y., Tóth, G., May 2006. The global ionosphere thermosphere model. Journal of Atmospheric and Solar-Terrestrial Physics 68, 839–864.

Ridley, A. J., Hansen, K. C., Tóth, G., De Zeeuw, D. L., Gombosi, T. I., Powell, K. G., Oct. 2002. University of Michigan MHD results of the Geospace Global Circulation Model metrics challenge. Journal of Geophysical Research (Space Physics) 107, 1290.

Ridley, A. J., Kihn, E. A., Apr 2004. Polar cap index comparisons with amie cross polar cap potential, electric field, and polar cap area. Geophysical Research Letters 31, 07801.

Schunk, R. W., Jan. 1981. Electron temperature anisotropy in the polar wind. J. Geophys. Res. 86, 91–102.

Schunk, R. W., Nagy, A. F., 2000. Ionospheres: Physics, Plasma Physics, and Chemistry. Cambridge University Press, Cambridge, UK.

Schunk, R. W., Sojka, J. J., Jul. 1989. A three-dimensional time-dependent model of the polar wind. J. Geophys. Res. 94, 8973–8991.

Schunk, R. W., Sojka, J. J., Jun 1997. Global ionosphere-polar wind system during changing magnetic activity. Journal of Geophysical Research 102, 11625.

Sharp, R. D., Lennartsson, W., Strangeway, R. J., Jun. 1985. The ionospheric contribution to the plasma environment in near-earth space. Radio Science 20, 456–462.

Shemansky, D. E., Hallett, J. T., Liu, X., Dec. 2005. The First Cassini UVIS Stellar Occultation of the Saturn Atmosphere. AGU Fall Meeting Abstracts, D4+.

Shematovich, V. I., Johnson, R. E., Michael, M., Luhmann, J. G., Aug. 2003. Nitrogen loss from Titan. J. Geophys. Res. 108, 6–1.

Smith, G. R., Shemansky, D. E., Holberg, J. B., Broadfoot, A. L., Sandel, B. R., McConnell, J. C., Nov. 1983. Saturn's upper atmosphere from the Voyager 2 EUV solar and stellar occultations. J. Geophys. Res. 88, 8667–8678.

Smith, H. T., Johnson, R. E., Shematovich, V. I., Aug. 2004. Titan's atomic and molecular nitrogen tori. Geophys. Res. Lett. 31, 16804.

Smith, H. T., Shappirio, M., Sittler, E. C., Reisenfeld, D., Johnson, R. E., Baragiola, R. A., Crary, F. J., McComas, D. J., Young, D. T., Jun. 2005. Discovery of nitrogen in Saturn's inner magnetosphere. Geophys. Res. Lett. 32, 14.

Spencer, J. R., Pearl, J. C., Segura, M., Flasar, F. M., Mamoutkine, A., Romani, P., Buratti, B. J., Hendrix, A. R., Spilker, L. J., Lopes, R. M. C., 2006. Cassini Encounters Enceladus: Background and the Discovery of a South Polar Hot Spot. Science 311 (5766), 1401–1405. URL http://www.sciencemag.org/cgi/content/abstract/311/5766/1401

Stout, Q., De Zeeuw, D., Gombosi, T., Groth, C., Marshall, H., Powell, K., 1997. Adaptive blocks: A high-performacie data structure. In: Supercomputing 1997 Conference, IEEE Comput. Soc., San Jose, Calif.

Strangeway, R. J., Russell, C. T., Carlson, C. W., McFadden, J. P., Ergun, R. E., Temerin, M., Klumpar, D. M., Peterson, W. K., Moore, T. E., Jan 2000. Cusp field-aligned currents and ion outflows. Journal of Geophysical Research 105, 21129.

Tóth, G., Sokolov, I. V., Gombosi, T. I., Chesney, D. R., Clauer, C. R., De Zeeuw, D. L., Hansen, K. C., Kane, K. J., Manchester, W. B., Oehmke, R. C., Powell, K. G., Ridley, A. J., Roussev, I. I., Stout, Q. F., Volberg, O., Wolf, R. A., Sazykin, S., Chan, A., Yu, B., Kóta, J., Dec. 2005. Space Weather Modeling Framework: A new tool for the space science community. J. Geophys. Res. 110 (A12), 12226–12246.

Tsyganenko, N. A., Aug. 2002a. A model of the near magnetosphere with a dawn-dusk asymmetry 1. Mathematical structure. Journal of Geophysical Research (Space Physics) 107, 1179.

Tsyganenko, N. A., Aug. 2002b. A model of the near magnetosphere with a dawn-dusk asymmetry 2. Parameterization and fitting to observations. Journal of Geophysical Research (Space Physics) 107, 1176.

Tsyganenko, N. A., Sitnov, M. I., Mar. 2005. Modeling the dynamics of the inner magnetosphere during strong geomagnetic storms. Journal of Geophysical Research (Space Physics) 110, 3208.

Ukhorskiy, A. Y., Anderson, B. J., Brandt, P. C., Tsyganenko, N. A., Nov. 2006. Storm time evolution of the outer radiation belt: Transport and losses. Journal of Geophysical Research (Space Physics) 111, 11.

van Allen, J. A., Nov. 1959. The Geomagnetically Trapped Corpuscular Radiation. J. Geophys. Res. 64, 1683.

VanLeer, B., 1979. Towards the ultimate conservative difference scheme. V. A Second order sequel to Godunov's method. J. Comput. Phys. 32, 101.

Vette, J. I., Nov. 1991. The AE-8 trapped electron model environment. NASA STI/Recon Technical Report N 92, 24228.

Waite, J. Hunter, J., Combi, M. R., Ip, W.-H., Cravens, T. E., McNutt, Ralph L., J., Kasprzak, W., Yelle, R., Luhmann, J., Niemann, H., Gell, D., Magee, B., Fletcher, G., Lunine, J., Tseng, W.-L., 2006. Cassini Ion and Neutral Mass Spectrometer: Enceladus Plume Composition and Structure. Science 311 (5766), 1419–1422.
URL `http://www.sciencemag.org/cgi/content/abstract/311/5766/1419`

Wang, H., Ridley, A. J., Luhr, H., 2008. Validation of the space weather modeling framework using observations from champ and dmsp. Space Weather, 16In Press.

Weimer, D., Jan 1996. A flexible, imf dependent model of high-latitude electric potentials having "space weather" applications. Geophys Res Lett 23, 2549–2552.

Wiltberger, M., Wang, W., Burns, A., Solomon, S., Lyon, J., Goodrich, C., Jan 2004. Initial results from the coupled magnetosphere ionosphere thermosphere model: magnetospheric and ionospheric responses. Journal of Atmospheric and Solar-Terrestrial Physics 66, 1411–1423.

Winglee, R. M., Apr. 2000. Mapping of ionospheric outflows into the magnetosphere for varying IMF conditions. Journal of Atmospheric and Terrestrial Physics 62, 527–540.

Wrenn, G., Rodgers, D., Ryden, K., Jan 2002. A solar cycle of spacecraft anomalies due to internal charging. Ann. Geophys.

Young, D. T., Berthelier, J.-J., Blanc, M., Burch, J. L., Bolton, S., Coates, A. J., Crary, F. J., Goldstein, R., Grande, M., Hill, T. W., Johnson, R. E., Baragiola, R. A., Kelha, V., McComas, D. J., Mursula, K., Sittler, E. C., Svenes, K. R., Szegö, K., Tanskanen, P., Thomsen, M. F., Bakshi, S., Barraclough, B. L., Bebesi, Z., Delapp, D., Dunlop, M. W., Gosling, J. T., Furman, J. D., Gilbert, L. K., Glenn, D., Holmlund, C., Illiano, J.-M., Lewis, G. R., Linder, D. R., Maurice, S., McAndrews, H. J., Narheim, B. T., Pallier, E., Reisenfeld, D., Rymer, A. M., Smith, H. T., Tokar, R. L., Vilppola, J., Zinsmeyer, C., Feb. 2005. Composition and Dynamics of Plasma in Saturn's Magnetosphere. Science 307, 1262–1266.

Zhang, J., Liemohn, M. W., De Zeeuw, D. L., Borovsky, J. E., Ridley, A. J., Toth, G., Sazykin, S., Thomsen, M. F., Kozyra, J. U., Gombosi, T. I., Wolf, R. A., Apr. 2007. Understanding storm-time ring current development through data-model comparisons of a moderate storm. Journal of Geophysical Research (Space Physics) 112, 4208.

Zheng, Y., Fok, M.-C., Khazanov, G. V., Dec. 2003. A radiation belt-ring current forecasting model. Space Weather 1, 1.